THERMAL DESIGN STUDIES IN NIOBIUM AND HELIUM FOR SUPERCONDUCTING RADIO FREQUENCY CAVITIES

By

Ahmad Aizaz

A DISSERTATION

Submitted to
Michigan State University
In partial fulfillment of the requirements
for the degree of

DOCTOR OF PHILOSOPHY

Department of Mechanical Engineering

2006

ABSTRACT

THERMAL DESIGN STUDIES IN NIOBIUM AND HELIUM FOR SUPERCONDUCTING RADIO FREQUENCY CAVITIES

By

Ahmad Aizaz

Liquid helium is now a common refrigerant for superconducting radio frequency (SRF) technology. It helps in cooling the niobium (Nb) made SRF cavities below their superconducting transition temperature (T_c). Testing of these cavities is routinely done in saturated liquid helium-I (He-I) for low field measurements and in saturated liquid helium-II (He-II) for high field measurements. The thermal design studies of these cavities involve two thermal parameters, namely the temperature dependant thermal conductivity of Nb at low temperatures and the Nb-He interface heat transfer coefficient. During the fabrication process of the SRF cavities, Nb sheet material is plastically deformed through a deep drawing process to obtain the desired shape. The effect of plastic deformation on low temperature thermal conductivity as well as heat transfer coefficients in the two states (He-I and He-II) has been studied. Strain induced due to the plastic deformations reduces the thermal conductivity in its phonon transmission regime, which may explain the performance limitations of the SRF cavities during their high field operations. The effect of annealing the Nb samples at two different temperatures to restore the phonon peak in the thermal conductivity curve has also been studied. Measurements of heat transfer coefficient for nucleate pool boiling liquid helium are in agreement with the theoretical predictions as well as with the existing experimental data. These measurements reveal higher heat transfer for rough surfaces as compared with smoother ones. Kapitza conductance measurements for Nb - He-II interface for rough

surfaces with surface index (SI) more than 3 as compared with the flat and smooth surfaces have also been carried out before and after the annealing. Here, SI is defined as the ratio of exposed surface area to that of projected area. These measurements provide helpful insight in understanding the problem of Kapitza conductance for different surface topologies where the rough and annealed surface revealed increased Kapitza conductance.

ACKNOWLEDGEMENTS

The contributions of many people, both at scientific level and personal level have been fundamental to the completion of this dissertation.

First and the foremost, I would like to extend a huge thank you to my technical advisor, Terry L. Grimm, for essentially teaching me to think like a scientist. Though being from outside of my parent department of mechanical engineering, he completely understood my shortcomings and limitations. In this, he walked me through the difficult process of objective learning with patience. His pushing and urging for more effort when I needed to be pushed, and his general availability despite his hectic commitments elsewhere in his office, have made him the ideal advisor. His guidance in the art of presenting the research work like a salesman has simply been elegant.

Thanks also go to Neil T. Wright for acting as the Chair of my guidance committee. His full involvement in almost all the developmental stages of my research with valuable suggestions and guidance on my write-up drafts remained crucial in completing my thesis.

Special thanks to Robert McMasters for acting as Co-Chair on my guidance committee despite his transfer to another university in Virginia. His polite and friendly personality has been very instrumental, much beyond his professional obligations, in my initial settling down in the new environment of MSU as an international student. I must also acknowledge his support in getting me involved in this research project at the cyclotron laboratory.

In the same vein, I would like to thank all my student colleagues, both graduate and undergraduate, in the SRF group who have worked on my experimental setup or shared with me their emotions and feelings through thick and thin, especially Susan Musser, Dave and Mandy Meidlinger, Hairong Jiang and Tim Kole.

The collaborative work with Pierre Bauer, Claire Antoine and Chris Boffo, from Fermi National Accelerator Laboratory, who helped me with providing flat plate Nb samples, was pivotal to my research validation. This dissertation would be incomplete without their contributions. Titanification processing on the Nb samples done at Cornell was only possible through the generous help extended by Rongli Geng. This help is well appreciated.

Finally, I'd like to thank my best friend and wife Asma Aizaz, for all the late night dinners brought to the lab when I had to run experiments, and the help in encouraging me to finish the thesis well in time. Without your tremendous patience, support and love, this work would not have been completed.

Last of all, I would like to thank both my parents, Malik Sher Afgan and Mrs. Munawar Malik, for moral and spiritual support through their well-needed prayers. This work would not have been completed without their prayers.

TABLE OF CONTENTS

LIST OF FIGURES

LIST OF TABLES

1 Introduction

Advances in particle physics are closely linked to advances in particle accelerators. Among many factors affecting the performance of the accelerator, the availability of higher energy particle beams is one of the most important.

A key component of the modern particle accelerator is the device that imparts energy to the charged particles. This is the superconducting electromagnetic cavity resonating at a microwave radio frequency (SRF). The resonating frequency is typically between 50 MHz and 3000 MHz. Among many practical limitations of achieving high performance in SRF cavities, this study deals with their thermal limitations. The work described in this thesis is an attempt to improve the performance of SRF cavities by studying its thermal design parameter.

1.1 SRF Cavities

An SRF cavity is the device through which power is coupled into the particle beam of an accelerator. As mentioned earlier, SRF accelerating cavities are microwave resonators, which generally derive from a "pillbox" shape (right circular cylindrical), with connecting tubes to allow particle beam to pass through for acceleration. Figure 1.1 shows a typical cylindrically symmetric cavity. The electric field is roughly parallel to the beam axis, and decays to zero radially upon approaching to the cavity walls. Boundary conditions dictate that the electric field must be normal to the metal surface with peak electric field occurring near the iris; a region where the beam tube joins the cavity. The magnetic field is in the azimuthal direction, with the peak magnetic field located near the cavity equator but decays to zero on the cavity axis.
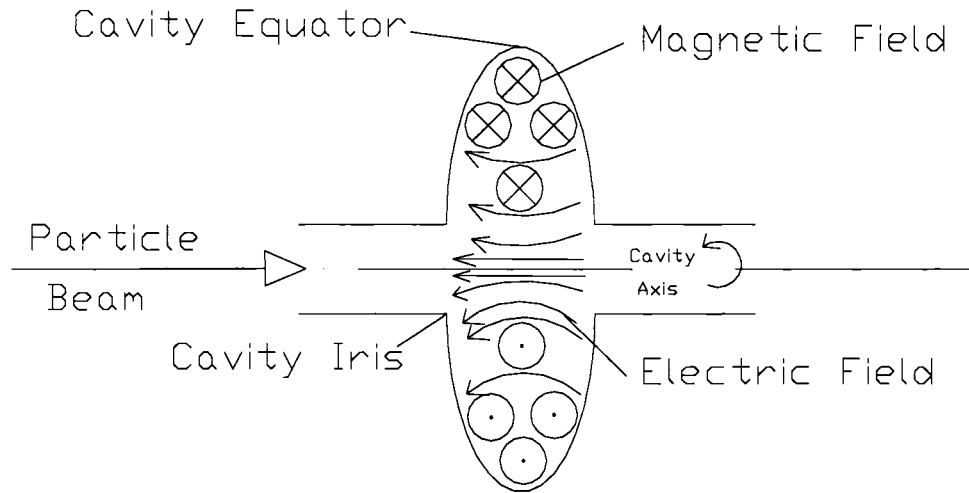
Figure 1.1: A typical SRF elliptical cavity, showing particle beam and fundamental or lowest RF frequency mode (TM 010) of the SRF cavity.

An important figure of merit in evaluating various SRF cavity structures is its quality factor (Q_o), which is defined as the product of RF angular frequency (ω) and the ratio of the stored energy in the electromagnetic fields (U) to the dissipated power (P_{diss}), and can be written as

$$Q_o = \omega \, U \, / \, P_{diss} \qquad (1\text{-}1)$$

It is known that surface resistance causes power dissipation by the surface currents, which arise in order to support the magnetic fields at the RF surface. The dissipated power can be written as the ratio of the square of accelerating voltage (V_{acc}) and the shunt impedance (R_a), that is,.

$$P_{diss} = (V_{acc})^2 \, / \, R_a \qquad (1\text{-}1a)$$

and Q_o is also frequently written as

$$Q_o = G \, / \, R_s \qquad (1\text{-}1b)$$

2

where, G is the geometric constant depending upon the shape of the cavity and R_s is the RF surface resistance.

Therefore, the dissipated power in the cavity can be related with R_s, as:

$$P_{diss} = \frac{V_{acc}^2}{\left(R_a/Q_o\right)Q_o} = \frac{V_{acc}^2}{\left(R_a/Q_o\right)G}R_s \qquad (1\text{-}1c)$$

Here (R_a / Q_o) is another figure of merit often quoted for determining the level of mode excitation by charges passing through the cavity. Note that it is independent of RF surface resistance as well as of cavity size. Often one quotes the average accelerating electric field (E_{acc}) that the electron sees during transit. This is given by

$$E_{acc} = V_{acc}/d \qquad (1\text{-}1d)$$

where, d is the active length of an accelerating structure and is usually an iris to iris distance of a typical elliptical cavity such as shown in figure 1.1.

Wall losses usually occur in the form of heat dissipation through the wall material of the cavity into the liquid helium surrounding the cavity. As the power increases, a stage comes when the losses become too great to allow the liquid helium to remove the heat from the cavity. At this point, the temperature of the material starts rising higher than the material's superconducting critical temperature (T_c) above which the material becomes a normal conductor, bringing about a sudden degradation of the performance of the SRF cavity. This mechanism of performance degradation of SRF cavities is usually known as thermal breakdown or "quench" and is described more in the subsequent paragraphs.

1.2 Advantages of SRF Cavities

It is well known that many materials, known as superconductors, lose all DC electrical resistance when the temperature drops below the T_c. However, unlike DC

3

resistance, RF resistance is zero only at T=0 K (absolute zero). At temperatures above absolute zero, but below the critical temperature, the surface resistance is greatly reduced, yet non-zero. This phenomenon is usually explained through the "London two-fluid model". According to this model, for temperatures less than $T_c/2$, the superconducting surface resistance can be well represented as:

$$R_s = A\frac{f^2}{T_s}\exp(-\frac{\Delta(o)}{K_B T_s}) + R_o \qquad (1\text{-}2)$$

The first term on the right hand side of equation 1-2 is the BCS surface resistance; named after the three scientists who first presented the BCS theory i.e. Bardeen, Cooper, and Schrieffer. For surface temperatures (T_s) less than $T_c/2$, the binding energy, $\Delta(0)$, is nearly unchanged from its value at absolute zero. The coefficient A is a function of material parameters such as the superconducting coherence length, the penetration depth, the electron mean free path, and the Fermi velocity. Here, k_B is the Stefan-Boltzmann constant and the value of A (1.333×10^{-4} for RRR ~230) can be evaluated computationally via programs by Turneasure [1] or Halbritter [2]. Material purity is usually described via the Residual Resistivity Ratio (RRR), which is the ratio of electrical resistivity at room temperature to the normal conducting resistivity at 4.2 K. The BCS surface resistance in a typical f = 3 GHz cavity varies from 3 μOhms at T=4.2 K to less than 1 nOhm at T=1.4 K. It is important to note that cavities operating at 4.2 K in He-I, i.e. when the temperature is not significantly less than $T_c/2$, the use of relation 1-2 may not produce accurate results predicted by BCS theory.

The second term on the right hand side of equation 1-2 is the residual resistance R_o, which is temperature independent. Mechanisms for R_o are not well understood, though

several possibilities have been proposed and investigated [3], [4]. Residual resistance values are generally found to be between 5 and 100 nOhm, although values as low as 1 nOhm have been measured [5].

The chief advantage in the use of SRF cavities is the reduced wall loss power dissipation. The wall loss power dissipation is proportional to the surface resistance, which is reduced by a factor of 10^6 in superconducting cavities as compared to copper cavities. The total power usage does not reflect all of this gain, however, due to the need to refrigerate the cavities to liquid helium temperatures. Even including refrigerator power, using typical refrigerator efficiencies, the net power usage drops by a factor of several hundreds to a thousand in superconducting cavities. In continuous operation (CW) this means greatly reduced power and higher accelerating gradients. In pulsed operation, SRF cavities offer long pulse lengths and high duty cycles compared to normal conducting cavities.

Niobium is currently the material of choice for superconducting cavities. The main reason for this choice is that niobium has the highest critical temperature of all pure metals ($T_c = 9.25$ K), and in addition, is relatively simple to fabricate.

Experimentation with specially designed SRF non-accelerating cavities [6],[7] has clearly shown that there are no fundamental limits to the peak electric fields on a niobium surface up to $E_{peak} = 200$ MV/m. The theoretical limit on accelerating cavity performance is therefore dependant on the cavity's magnetic fields. The DC critical magnetic field is thus related with the metal temperature as

$$H_c(T) = H_c(0)\left[1 - \left(\frac{T_s}{T_c}\right)^2\right]$$ (1-3)

where $H_c(0)$ is the critical magnetic field at T=0 K.

In RF conditions, the requirements are relaxed somewhat, as the penetration of the magnetic field into the RF surface requires nucleation of a flux line, which requires a finite amount of time. The nucleation time has been determined to be such that the complete shielding of magnetic fields can persist to fields higher than the critical field, up to a limit termed the superheating critical field, H_{sh}. In niobium, the superheating critical field is estimated to be approximately $H_{sh} = 2300$ [8] oersted (or simply Oe).

In typical SRF accelerating cavities, $H_{peak} = 2300$ Oe corresponds to accelerating gradients of 50 to 60 MV/m. Given that, accelerators with niobium cavities generally operate at $E_{acc} = 10$-20 MV/m, the need for further improvement is clear.

1.3 Limitations of SRF Cavities Through Thermal Breakdown

Thermal breakdown is a phenomenon in which the temperature of part or the entire RF surface exceeds the critical temperature, thereby becoming normal conducting and rapidly dissipating all of the stored energy in the cavity fields. The field at which breakdown occurs depends upon multiple factors; including thermal conductivity of the bulk niobium and heat transfer from the niobium to liquid helium bath. There are many processes, which, by acting either independently or simultaneously, can cause thermal breakdown of the cavity. Some of these are listed below.

1.3.1 Thermal Breakdown Due to Defects

Material defects are the most commonly understood cause of thermal break down in SRF cavities. In this, the break down is considered localized, where a small defect in the RF surface dissipates power more readily than surrounding superconducting walls. Breakdown occurs when the power dissipation overwhelms the ability of the Nb to

conduct away the heat to surrounding liquid helium acting as the coolant. Thus the temperature of the defect rises above the critical temperature of the bulk Nb, making it normal conducting and eventually leading to thermal breakdown. It has been shown in previous studies [9] that the local magnetic field just before thermal break down around a hemispherical defect, to a first order approximation, can be given as:

$$H_{tb} = \sqrt{\frac{4k(T_c - T_b)}{r_d R_d}} \qquad (1\text{-}4)$$

Here, H_{tb} is the thermal breakdown magnetic field, k is the thermal conductivity of the Nb, T_c is critical temperature of Nb, T_b is the bulk temperature of the liquid helium, 'r_d' is the defect radius and R_d is the electrical surface resistance of the defect. From this relation, it appears that the defect in the Nb skin is thermally isolated from the cooling effects of the surrounding liquid helium and the breakdown magnetic field is totally dependant only upon the thermal conductivity of the bulk Nb.

1.3.2 Global Thermal Instability (GTI)

Another type of thermal breakdown usually attributed to high surface magnetic field regions is global thermal instability (GTI) [10]. In GTI, the heating is nearly uniform over all of the high surface magnetic field regions. GTI occurs because, even without localized defects, the RF surface retains some uniform residual RF resistance. GTI is initiated when the power dissipation due to residual resistance raises the temperature enough such that the exponentially growing BCS surface resistance becomes dominant, causing a thermal runaway process, which leads to a thermal breakdown. In this kind of thermal breakdown, both the Nb thermal conductivity as well as Nb-He interface heat transfer coefficient determines the maximum achievable fields before quenching.

7

1.3.3 Thermal Breakdown Due to Field Emission

Field emission (FE) is the process of electrons coming out of the Nb surface in the presence of high surface electric fields. These emitted electrons impact elsewhere on the cavity surface, heating the surface, and thereby increasing the surface resistance. This increases power dissipation of the cavity, as well as adding to the load on the refrigeration plant. In the extreme, FE heating of the cavity walls can lead to thermal breakdown, as mentioned in the last section. Acceleration of emitted electrons draws power out of the electromagnetic fields, which would otherwise be available for acceleration of the particle beam. Eventually, as fields are raised, the power dissipation into FE related processes limits the attainable fields in the cavity.

1.4 Thermal Magnetic Interactions in SRF Cavities

As discussed in the last section, the heat removal from the inner surface (RF surface) of the SRF cavity is via conduction through the niobium and convection to the liquid helium surrounding the cavity. The operation of low frequency ($f < \sim$300 MHz) cavities as well as low field-testing of high frequency SRF cavity is usually performed in liquid He I at around 4.2 K. However, the operation of high frequency cavities as well as high field-testing of low frequency cavities is done in He-II at around 2.0 K, where the helium is in its super-fluid state. Through a simple thermal circuit, as shown in figure 1.2, the influence of different thermal variables on the critical magnetic field can be understood.
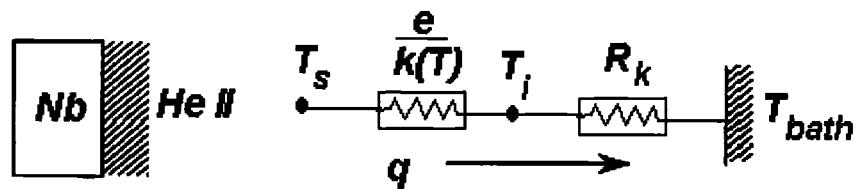
Figure 1.2: Heat Transfer from RF surface of SRF cavity to the surrounding liquid helium as depicted through electrical analogy.

8

Here, T_s the RF surface temperature due to various phenomena discussed in the last section, is created through joule heating, $k(T)$ is the temperature dependant thermal conductivity of the niobium, e is the thickness of the niobium, T_i is the temperature of the interface surface of the Nb exposed to the surrounding liquid helium, R_k is the bulk thermal resistance of the liquid helium when it is in normal state, however, it is commonly called the "Kapitza resistance" when liquid helium is in its super-fluid state, i.e. below 2.17 K and, T_{bath} is the temperature of the bulk liquid helium.

Figure 1.2 shows an element of the cavity wall in contact with He and the electrical analog of the heat flow path from the RF surface to the He bath. Through this electrical analogy, it is clear that heat current, q, has two distinct heat resistances in its path. One is characterized by the bulk material property of niobium i.e. thermal conductivity k, and the other is characterized by the heat transfer coefficient h or h_k of the liquid helium depending upon its state.

For the case of a defect free cavity, the influence of R_k (or `$1/h_k$) and k on the accelerating field, E_{acc}, can be investigated as done by others [11], through some simple thermal-magnetic simulations as shown in figure 1.3. Here, E_{acc} is directly proportional to peak surface magnetic fields (B_{pk}). Consider that the heat flux q in W/m^2 is solely produced by Joule heating at the inner surface wall and is uniquely due to the RF surface resistance R_s, then it can be expressed [11] as :

$$q = 1 / (2\mu_o^2) R_s B^2 \qquad (1\text{-}4)$$

9

where, μ_o is the magnetic permeability, B, expressed in Tesla, is the magnetic flux density on the RF surface of the cavity and, R_s is the surface resistance in ohms, which, itself is a function of RF surface temperature T_s as given by equation (1-2). The use of this equation on the high surface magnetic field regions, where the most intense heating is taking place, implies that the magnetic fields are B_{pk}.

Using equation 1-4 along with 1-D thermal model of figure 1.2 for a defect free SRF cavity, the maximum achievable magnetic fields (B_{pk}) are plotted as a function of the RF surface temperature for the two sets of values of thermal conductivity and Kapitza conductance. These constant property simulations clearly show the effect of increased k and h_k on the higher allowable magnetic field, which is then limited by the critical magnetic fields only. Another important observation can be made from these simulations is that for a defect free cavity, the maximum RF surface temperature rise due to applied magnetic fields is on the order of a few hundred milli-Kelvin only. This observation helps in understanding the operating range of temperature dependant thermal conductivity of Nb, as explained in the next section.
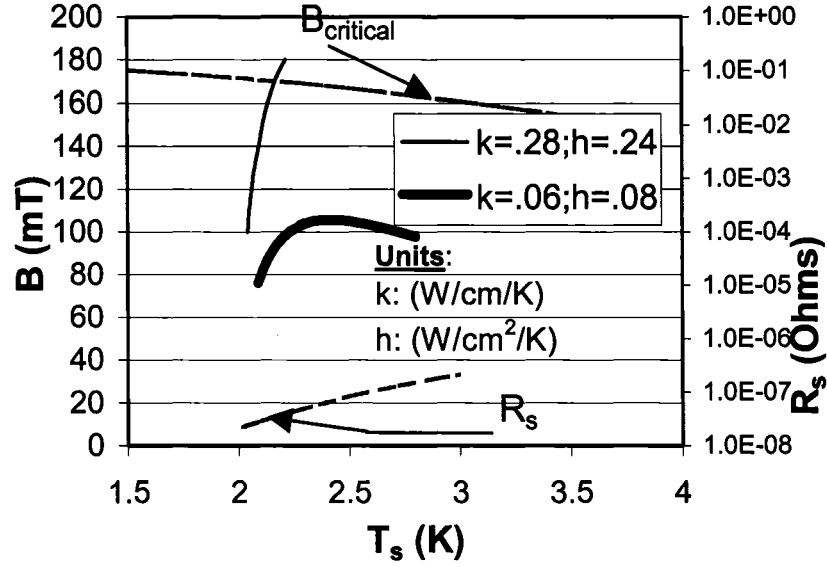
Figure 1.3: Thermal-magnetic simulations with constant thermal properties, k and h, for the two cases are shown. About five times increase in k and three times increase in h resulted in almost 50% improvement in applied magnetic fields. Parameters used for these simulations are R_{res} = 5 nohms, e = 3 mm, T_b = 2 K, f = 1.3 GHz, RRR = 230. Rise in surface resistance (right axis) due to RF surface temperature increase is also plotted.

1.4.1 Effect of Thermal Conductivity on SRF Cavities

At the operating temperatures of the cavities, when Nb is in its superconducting state, its thermal conductivity varies dramatically with temperature and is governed by the interplay of both of the heat carriers, i.e. electrons and phonons. Figure 1.4 shows a typical curve for Nb thermal conductivity at low temperatures where a local maxima is clearly visible below ~ 3 K. The thermal conductivity of Nb above 4 K is well known and correlates with its RRR value (k = RRR/4 @ 4.2 K) [9], however, below ~ 3 K, in the phonon conduction region, this correlation is not well understood. In this phonon conduction regime, the microstructure of the bulk Nb, characterized by strains and lattice imperfections or grain size and grain boundaries, plays a vital role in determining the

11

final shape of its thermal conductivity curve. A more thorough treatment of the thermal conductivity at low temperatures is given in chapter 2.
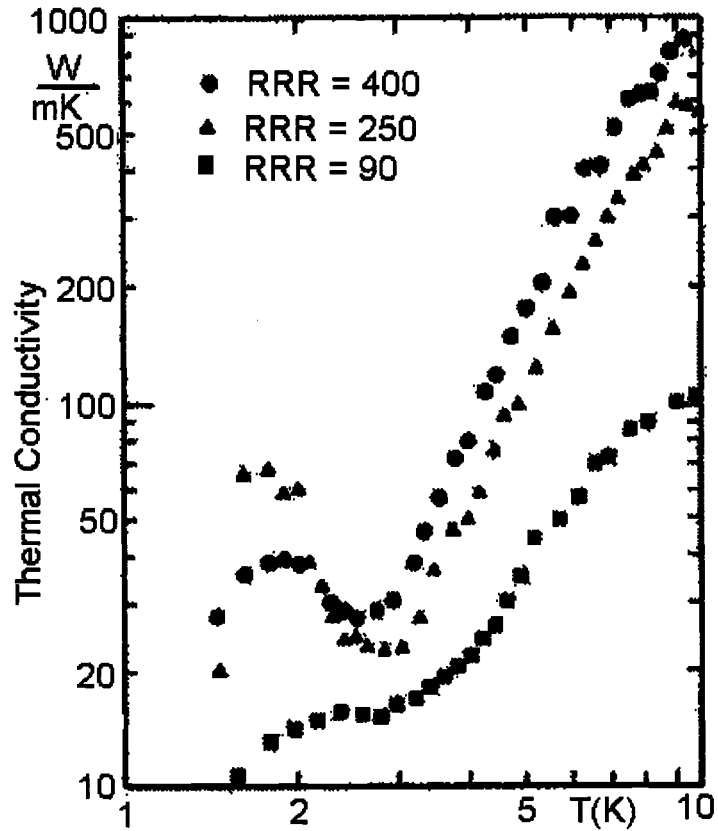
Figure 1.4: Temperature dependant thermal conductivity clearly shows the formation of a phonon peak at ~ 2 K. Adapted from Padamsee et al [9].

Much emphasis has been placed in the past on the techniques for improving thermal conductivity of the bulk Nb for temperatures above ~ 4 K to reduce the effect of 'localized defects' on the performance of the SRF cavities. In the case of cavities with a defect, which is of small size (on the order of micrometers) as compared to the wall thickness (~ 2-4 mm), a normal conducting defect causes an intense localized RF heating spot resulting ultimately in the thermal quench of the cavity. Due to poor thermal

conductivity of Nb, this localized heating remains thermally isolated from the surrounded pool bath of liquid helium. Thus, in case of thermal breakdowns due to defects, it is estimated [9] that since the temperature in the neighborhood of the defect is between the bath temperature and T_c, it is the high-temperature (4 to 9.2 K) thermal conductivity of Nb that is the most important and which will have the strongest effect on thermal breakdown. However, for defect free cavities, as has been discussed earlier, the total RF surface temperature rise is on the order of few hundreds of mK. Thus, the phonon thermal conductivity regime (< 3 K) of Nb plays the dominant role in determining the quench field of the defect free high frequency cavities. Nevertheless, for both of the cases, i.e. high frequency defect free cavities (< 3 K) or the cavities with defects (> 4 K), improving the thermal conductivity of Nb remains a paramount objective. The improved thermal conductivity at temperatures above ~ 4 K comes from improved purity of the metal quantified through its RRR value. Bulk Nb purity has improved greatly, from RRR of 10-30 to RRR > 250, in the last twenty years through improved purification methods, e.g. high vacuum electron beam melting [12].

Niobium can be further purified of interstitial oxygen by solid-state gettering [11], [12]. In gettering, the Nb is heated to ~1400 C, with exposure to either yttrium or titanium vapor. The vapor is absorbed into the surface of the Nb; the higher affinity towards O_2 of Y or Ti (compared to Nb) effectively removes the oxygen from the bulk Nb. Oxide layer at the outer surface is removed through acid etching, leaving purified bulk Nb. Typically, material with a RRR of 250 can be purified to a RRR of 500 through this process. Increasing the grain size or reducing the grain boundaries can also improve the microstructure of the bulk Nb, thus improving the phonon thermal conductivity of the

Nb. Annealing the Nb at temperatures above ~ 1400 C in a high vacuum furnace creates large grain size resulting in the formation of a "phonon peak" in the thermal conductivity of Nb, as seen in figure 1.4 [9].

1.4.2   Effect of Heat Transfer Through Liquid Helium on SRF Cavities

The other resistive parameter in the thermal circuit, as shown in figure 1.2, is the R_k, i.e. resistance to heat transfer through the liquid He. It has been shown [12] that in the case of defects on the RF surface of the cavity, the heat transfer coefficient at the Nb-He interface does not play as strong a role as the thermal conductivity in determining the quench field. This may be the reason that little attention has been given in the past to this particular aspect for the improvement of performance in SRF cavities. Although, a lot of information has been accumulated in the understanding of this mode of heat transfer in other spheres of scientific research, such as quench dynamics of superconducting magnets, relatively little attention has been paid toward this mode for the purpose of improving the performance of SRF cavities. Moreover, the importance of the heat transfer to the pool bath of liquid helium increases, as the thermal conductivity improves with purity, or as the Nb wall thickness is decreased, or if there are no defects such as that shown through simple thermal-magnetic simulations presented in figure 1.3. Therefore, it seems quite logical to explore various channels of pool boiling heat transfer, both at 4.2 K as well as at temperatures below 2.1 K, for the improvement of the cavity performance. For this purpose, basic understanding of heat transfer in liquid He is of primary importance and is presented in chapter 3.

2 Thermal Conductivity at Low Temperatures

To understand how thermal conductivity depends upon temperature, especially at low temperatures, it is useful to understand the basic mechanisms for energy transport through materials. There are three basic modes of energy transport (phonon, electron, and molecular), and hence heat conduction, through a solid. These are described below.

2.1 Phonon Conduction

Lattice vibrational energy transport, also known as phonon conduction, occurs in all solids, both dielectrics and metals. This mode dominates in nonmetallic crystals, some inter-metallic compounds and even exists in superconducting metals, such as Nb, below their transition temperatures. For single crystals at low temperatures, this mode of heat conduction can be effective, equaling or exceeding the conduction by pure metals. Phonon thermal conductivity may be mathematically expressed as

$$k_t = 1/3 \; C_v \, v \, \lambda \tag{2-1}$$

where, C_v is the lattice heat capacity of the material, v is the average propagation velocity of phonons, which travel at the speed of sound, and λ is the mean free path of the phonons between collisions or before scattering from the obstacles. The variability of these parameters with respect to temperature is illustrated in figure 2.1 [14]. The peak in phonon conductivity for Nb ($T_c = 9.2$ K) usually occurs near 2K, whereas for some non-metals it could be as high as about 30 K.

15

(a)

k_t

T

(b)

C_v

T

(c)

$\bar{v}$

T

(d)

λ

T
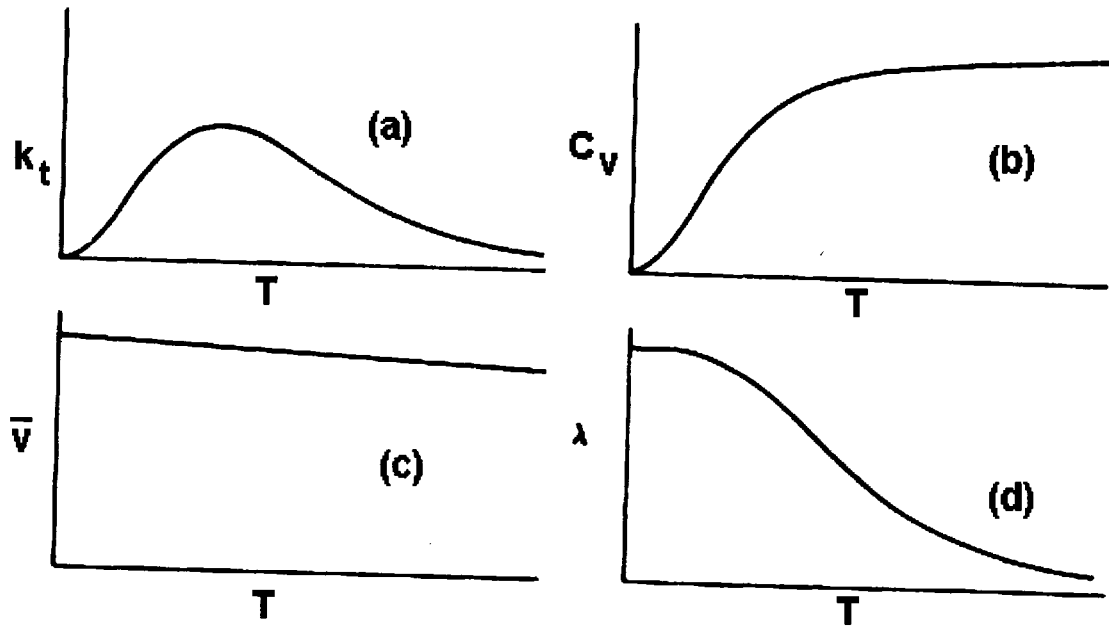
Figure 2.1: Thermal conductivity by phonon mechanism [14]

2.2 Electronic Conduction

Energy transport in metals is dominated by electron motion. Metals, of course, also have a lattice structure and hence experience a lattice contribution to the thermal conductivity, as well. However, thermal conductivity in pure metals is due primarily to the "free" conduction electrons, those that are only loosely bound to the atoms so that they wander readily throughout the crystal lattice and thus transfer thermal energy. Mathematically, electronic conduction of thermal energy may be expressed as

$$k_e = 1/3 \ C_v' \ v_e \lambda_e \qquad (2\text{-}2)$$

where, C_v' is the electronic heat capacity of the material per unit volume, v_e is the mean velocity of electrons also known as Fermi velocity, and λ_e is the mean free path of the electrons between collisions or before scattering from the obstacles. The variability of

16

these parameters with respect to temperature is illustrated in figure 2 [14]. For pure metals, the maximum in the electronic contribution to thermal conductivity, as shown in figure 2.2, appears roughly in the temperature range of 20 to 100 K.
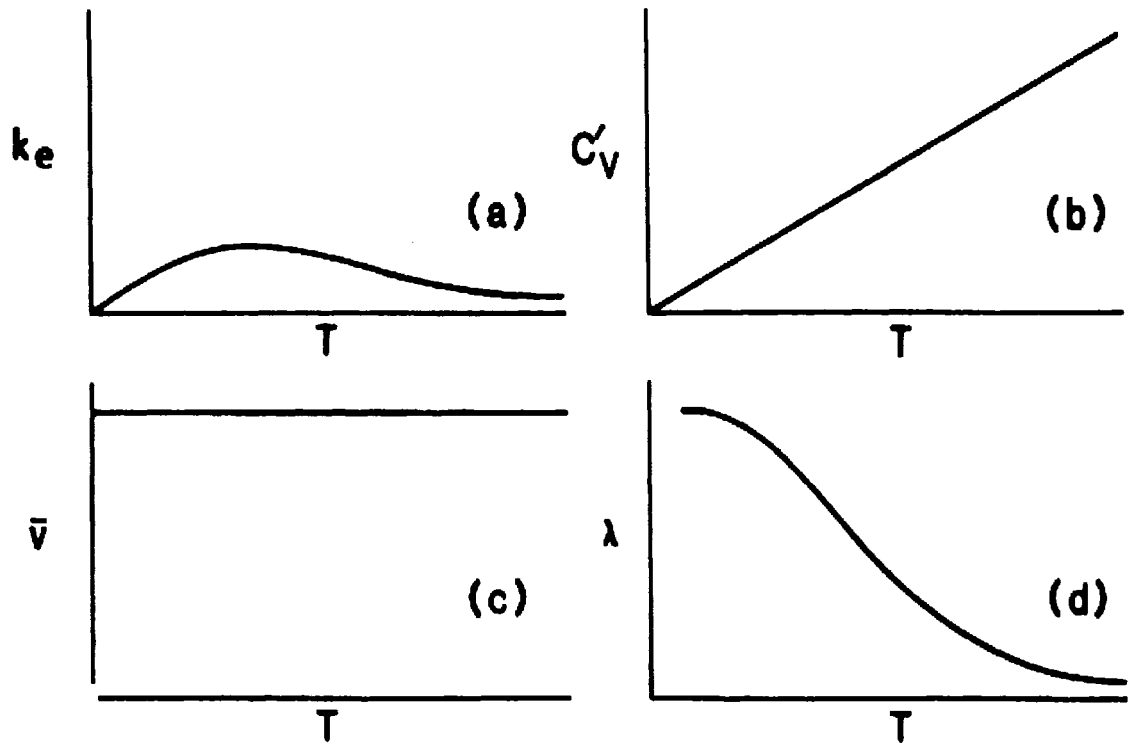
Figure. 2.2.   Thermal conductivity by electron mechanism [14]

2.3 Molecular Conduction

Molecular motion, such as noted in organic solids and fluids, is another energy transport mechanism [14]. This characteristic disorder, as well as lattice imperfections of organic solids, introduces resistances to heat flow. Even though the thermal energy carriers are the same, where phonons dominate over the electrons, the path to carry thermal energy (i.e. how disorderly molecules are chained and tangled together) in this

mode is what makes it different from the other two. Accordingly, the disordered dielectrics such as glass and polymeric plastics are the poorest solid conductors of heat. Since our current topic concerns structural (ordered) material, we shall ignore this energy transport mechanism.

2.4 Thermal Conduction in Niobium

Since thermal conduction in Nb has contributions from both of the first two mechanisms, namely, from electrons and lattice vibrations, the overall thermal conductivity of Nb is addition of both the terms given in equation 2-1 and 2-2, and is given as:

$$k = k_e + k_t \tag{2-3}$$

Below its transition temperature T_c, Nb metal enters into its superconducting state where electrons transform into Cooper pairs and are thus neither able to scatter phonons nor accept thermal energy to carry through. Therefore, below T_c, as shown in the right curve of figure 2.3 [15], the contribution of phonon conduction (equation 2-1) begins to increase. As the temperature is further lowered, more electrons freeze into Cooper pairs and are unavailable to conduct heat. Thus the thermal conductivity of Nb declines rapidly. At about 3 K or so, a local minimum in thermal conductivity is usually observed where the contribution of the two thermal conductivities, k_e and k_t, becomes comparable to each other. The "phonon peak" is seen with further decreasing temperature due to increased contribution of the phonon conduction mechanism [9], as shown in left curve of figure 2.3. This phonon peak in thermal conductivity of Nb, as the name suggests, is due to the large mean free path of the phonons before getting scattered. The magnitude of this peak depends upon the absence of electron-phonon scattering mechanism in the

superconducting state of Nb, the mechanism which otherwise exists at these temperatures for pure metals. Thus, for Nb, reducing the phonon scattering mechanisms, such as increasing the grain size as well as other scattering mechanisms, as discussed below, can form a local peak in the thermal conductivity near 2 K, as shown in Figure 2.3 [9].
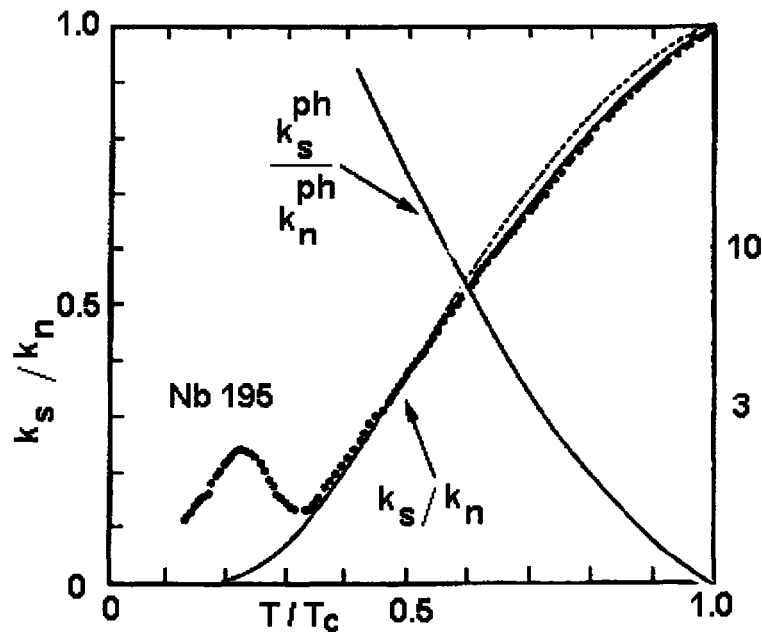
Figure 2.3. Measured thermal conductivity for a Nb sample as compared with a theoretical prediction. Steep decrease in electronic thermal conductivity is clearly seen below T_c. The curve on the right shows the rise in the theoretical prediction of phonon thermal conductivity when scattering of phonons from electrons is substantially reduced in the superconducting state as the temperature is decreased. This is the cause of phonon peak visible in the curve on the left [9].

2.5 Phonon Scattering Mechanisms

We have seen the importance of phonon heat conduction in Nb, which is unique among pure metals due primarily to its superconductivity below T_c. It is interesting to look at various phonon scattering mechanisms specifically in superconductor metals like Nb, which generally occur in dielectric solids. There are many characteristic phonon

19

scattering mechanisms that limit the mean free path of the phonons and hence limiting the thermal conductivity of the material. Since scattering increases the resistance, therefore it is often related in terms of a resistance parameter W [15], [16], where $W \propto 1/k$.

2.5.1 Phonon-Electron Scattering

This scattering mechanism results in thermal resistance on the order of $W_E \sim 1/T^2$. The mechanism is significant in metals at low temperatures. This is the main cause of reduction in thermal conductivity of Nb in the temperature range from just below T_c down to around 3 K.

2.5.2 Boundary (Grain or Specimen) Scattering

Boundary scattering, such as grain boundary or specimen boundary, results in thermal resistance on the order of $W_B \sim 1/T^3$ at very low temperatures, where the mean free path becomes comparable to crystal dimensions. In temperature ranges below ~1K the specimen size effects play a dominant role in determining the thermal conductivity of the material.

2.5.3 Impurity Scattering

Scattering of phonons due to interstitial impurities present another mechanism of resistance to thermal energy and is on the order of $W_D \sim 1/T^{3/2}$.

2.5.4 Dislocation Scattering

Scattering of phonons due to dislocation of atoms in the material or due to other defects results in thermal resistance on the order of $W_{dis} \sim 1/T^2$.

3 Liquid Helium and Its Pool Boiling Theory

3.1 Pool Boiling Heat Transfer in He-I

He-I, or normal He, is like an ordinary fluid with state properties that can be described by empirical relations. The general characteristics of He-I show rather low thermal conductivity and large volumetric heat capacity, which suggests that conduction heat transport is of little significance to the overall heat transfer.

The traditional approach of empirical relations to the interpretation of heat transfer is best suited for dealing with the He-I. The real phenomena of heat transfer through a heated surface into the fluid are quite complex and therefore are difficult to model from the first principles. A specific problem requires a solution of a complex set of equations, which are only treatable in the simplest geometries. Therefore, engineering problems are scaled on the basis of dimensionless variables, which are functions of the properties of the system. Usually, through the use of these dimensionless variables, fitting them to the experimental data develops functional relations. In general, for the problems of heat transfer, one of the important dimensionless parameters to consider is the Nusselt number, Nu. It represents a dimensionless heat transfer coefficient, defined by the relationship

$$Nu = hL/k \qquad\qquad (3\text{-}1)$$

where $h = q/(T_s - T_b)$, the heat transfer coefficient of the surface, T_s and T_b are the local surface and bath temperatures, k is the thermal conductivity, and L is a characteristic length in the problem. In pool boiling, L is the characteristic length of the heater, either its diameter or width as appropriate.

In the case of pool boiling heat transfer, the two relevant dimensionless numbers are the Grashof number (Gr) and the Prandtl number (Pr). The Grashof number indicates the ratio of buoyancy forces relative to the viscous forces. It is represented by the relationship

$$Gr = \frac{g\beta(T_s - T_b)L^3}{\nu^2} \qquad (3\text{-}2)$$

where, g is the acceleration due to gravity, β is the bulk expansivity, and ν is the kinematic viscosity. The Prandtl number contains most of the fluid properties and is given as:

$$Pr = \nu/\alpha = \eta C_p/k \qquad (3\text{-}3)$$

where, α is the thermal diffusivity, η is the viscosity and, C_p is the specific heat of the fluid.

In pool boiling heat transfer, when the dominant mechanism is natural convection, the Nusselt number is a function of these two numbers,

$$Nu = \varphi(Gr)\ \psi\ (Pr) \qquad (3\text{-}4)$$

where, φ and ψ are functions determined by empirical correlations of data.

Most empirical correlations for natural convection are given in terms of the Rayleigh number, which is simply the product of the Grashof and Prandtl numbers, i.e.,

$$Ra = GrPr = \frac{g\beta(T_s - T_b)L^3}{\alpha\nu} \qquad (3\text{-}5)$$

Simple correlations can be written in the form

$$Nu = C\ Ra^n \qquad (3\text{-}6)$$

where 'C' and 'n' are empirically determined parameters. The coefficient n depends mostly on the geometrical and flow conditions. Generally, n = 1/4 when flow is laminar

and n = 1/3 for turbulent flow in a vertically oriented heater in an open bath. The critical Ra_c is defined to distinguish between the two regimes. For flat plates, the transition between pure conduction and convection occurs for $Ra_c = 10^3$, while the transition between laminar and turbulent convection heat transfer usually occurs for $Ra_c = 10^9$. These relationships are only valid when no phase change process is taking place in the system. For an extensive review of natural convection, see Gebhart et al [41].

3.1.1   Regimes of Pool Boiling Heat Transfer in He-I

There are typically three regions of heat transfer in pool boiling of He-I as shown in figure 3.1 [17]: (1) natural convection, (2) nucleate boiling, and (3) film boiling. At the lowest heat fluxes up to a few mW/cm^2, heat is transferred by natural convection. Since no phase change is evident, density-driven mechanisms drive this heat transfer regime. The empirical correlation given in equation 3-6 can be used to estimate the surface temperature differences. As the heat flux is increased, bubbles of helium vapor begin to form locally at preferred sites on the heated surface, which are typically surface imperfections. Hysteresis in the heat transfer curve is caused by activation or deactivation of these imperfections by the low contact angle He-I. As the heat flux is further increased, the nucleation sites get fully activated with each site containing a bubble. This is the stage when any further increase in heat flux only serves to accelerate the rate of bubble growth and detachment. This in turn causes macroscopic turbulence where the heat transfer is near its maximum.
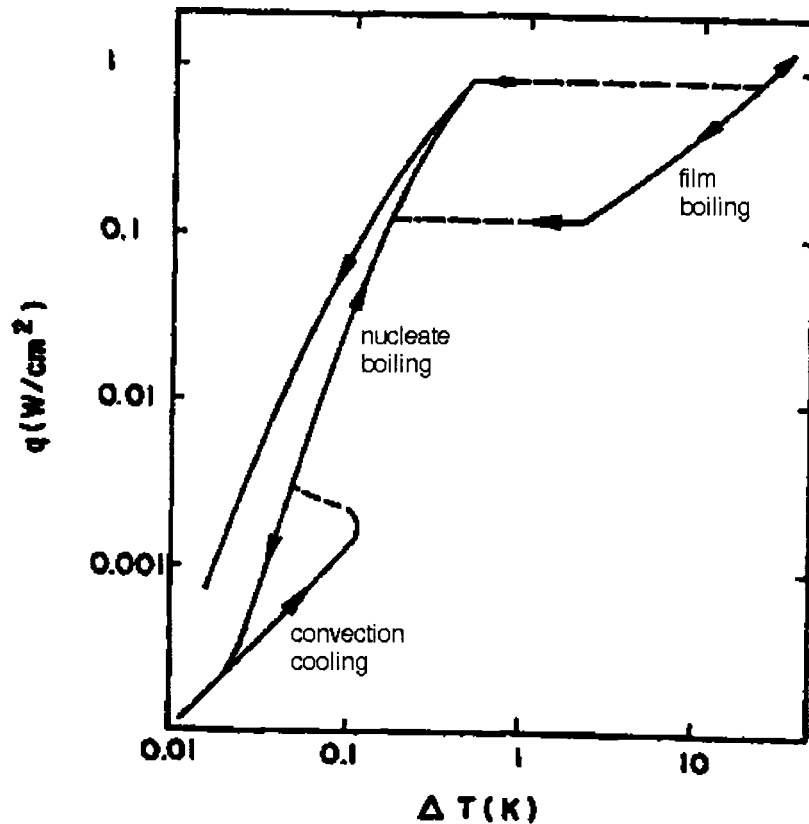
Figure 3.1 Typical heat transfer relationship for pool boiling He-I [17].

At still higher heat fluxes, the bubble size and frequency of detaching get so high that they become unstable and coalesce into continuous vapor films. The corresponding value of heat flux at this stage is known as peak nucleate boiling heat flux and the regime of nucleate boiling changes to film boiling. In the film-boiling regime, a vapor layer insulates the fluid from the surface and the cavity surface temperature difference is an order of magnitude higher than with nucleate boiling. The hysteresis in this regime of heat transfer is associated with the stability of a vapor film below a higher-density liquid.

3.1.2   Factors Affecting Pool Boiling Heat Transfer in He-I

As mentioned earlier, there are numerous factors that affect heat transfer characteristics. For example, surface orientation has a profound effect on heat transfer

behavior. Variation of the surface orientation with respect to the gravitational force can cause significant changes in the heat flux and the minimum film boiling heat flux. The highest values for both these quantities occur with the surface facing upward, because the buoyancy force aids bubble detachment[17].

The thermodynamic state of the liquid helium bath is also an important parameter in the heat transfer process. The bath temperature has a significant affect on various heat transfer parameters, especially the peak nucleate boiling heat flux q. Similarly, the bath pressure affects these values, particularly when considering the sub-cooled or supercritical state. These variables can be taken into account through the changes in the helium properties with temperature and pressure[17].

Variation in geometry can also have a profound effect on the heat transfer. Many engineering systems consist of channels, tubes, or other complex geometries, which are vastly different from the open "infinite bath" configuration. Due to the limited coolant volume associated with such geometrical limitations, difference in heat transfer can be expected. Some of the physical phenomena that can occur include heat-induced natural circulation and vapor locking in narrow channels[17].

The surface condition of the heat transfer sample can affect both the peak heat flux q and the ΔT_s in the nucleate boiling regime. The mechanism by which surface preparation affects the heat transfer characteristics, which also is the main aim of this research, is believed to be associated with the number of available nucleation sites. Improvement of pool boiling heat transfer in He-I through surface preparation holds significant potential in its application in the SRF cavity design. As discussed above, surface preparation

affects the heat transfer through the nucleation sites; therefore it is important to understand nucleate boiling heat transfer in more detail.

3.1.3 Nucleate Boiling Heat Transfer in He-I

In this mode of heat transfer, the helium is in two phases, liquid and vapor, mixed. Hence the free convection theory discussed previously is no longer valid. This phase of heat transfer is characterized by the formation of small bubbles at the nucleation site due to small (mW/cm^2) increases in the heat flux. The bubbles, when detached from the surface, rise above to the free surface thus carrying away the heat. The surrounding colder liquid quickly occupies the space left by the bubbles on the surface and thereby cooling the surface. As the heat flux is increased, essentially all of the nucleation sites are active. This condition is quite different from that of natural convection because it is controlled mostly by the hydrodynamics of bubble growth and detachment rather than convection in the liquid [17], [42].

The conditions under which bubble nucleation sites get activated are governed by nucleation theory. According to this theory, in order to have a bubble grow at a nucleation site, there must exist two conditions. Firstly, there must be a thin boundary layer of superheated liquid near the heat transfer surface interface, whose thickness may be approximated as,

$$\delta \sim k\Delta T_s / q \tag{3-7}$$

where, k is the thermal conductivity of the liquid, $\Delta T_s = T_s - T_b$ is the allowable superheat of the surface above the bath temperature, and q is the applied heat flux.

Typically, δ is of the order of 1-10 μm for the He-I near its normal boiling point. The reasons for the requirement of such a superheated boundary layer are envisaged in the

26

liquid near the interface being sub cooled due to hydrostatic head ($\Delta p = \rho gh$). So, the local temperature must rise above ambient before saturation conditions can be attained. Secondly, and probably more important, the surface tension of the liquid must be overcome in order for a vapor bubble to have a positive radius of curvature, as can be seen through the following equation:

$$p_v - p_s = \frac{2\sigma}{r} \tag{3-7a}$$

here p_v is the vapor pressure inside the bubble, p_s is the saturation pressure of the surrounding liquid and r is the radius of the bubble. Van Sciver et al [17], through some simplifying assumptions, has found the value of critical radius, r_c, of the bubble to be 0.0164 μm at saturation temperature and pressure conditions with $\Delta T_s = 0.3$. A bubble greater than r_c would be expected to grow while one smaller would collapse. This implies local surface imperfections must exist. These imperfections are necessary to provide preferential regions where bubbles can form. The imperfections are usually in the form of grooves or slots that allow bubble formation with a negative curvature, thus taking advantage of surface tension to stimulate the bubble nucleation.
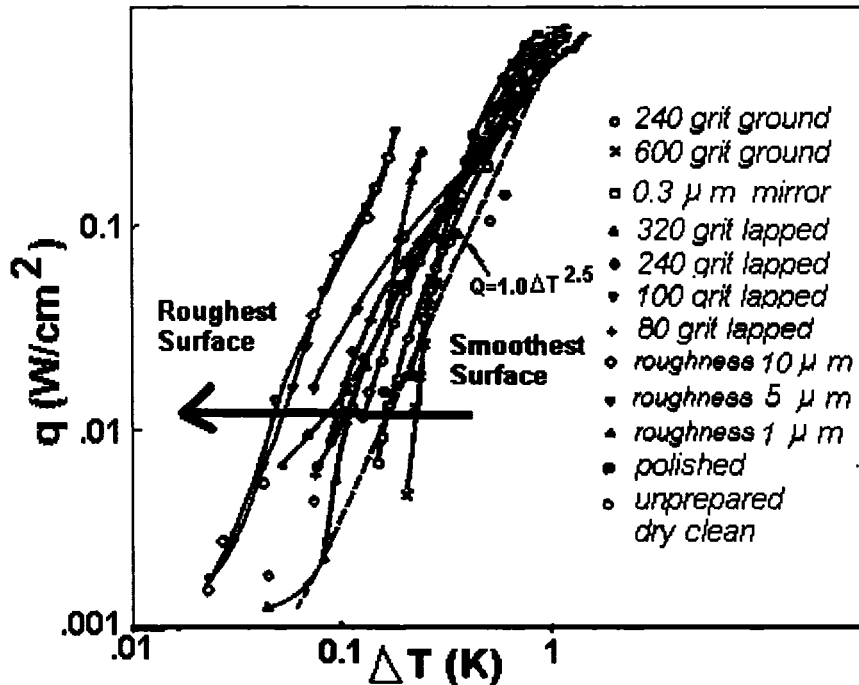
Figure 3.2: Nucleate boiling heat transfer to He I. Variation in the data is seen through a difference in surface roughness where increasing surface roughness lowers the surface super heat. Plotted empirical fit is by Schmidt and adapted from Van Sciver [17].

Though some engineering correlations do describe the nucleate boiling regime quite satisfactorily, especially those given by Kutateladze and Schmidt, there is wide variation in experimental data owing to differences in sample preparation, surface material and sample orientation. Based on the hydrodynamic arguments presented above, the different surface preparations would yield much different results. Figure 3.2 is a compilation [17] of nucleate pool boiling data for a flat copper surface facing upward as a function of heat flux. The empirical fit used by Schmidt is also plotted in figure 3.2. Due to its conservative form it is more popular for engineering applications. The data vary over at least half an order of magnitude in ΔT for a given q, with the smoothest surfaces

28

apparently allowing larger superheat. This is consistent with the arguments presented earlier based on the nucleation theory. Therefore, a rough surface is preferable for increasing the heat transfer by providing preferential nucleation sites for the bubbles formation.

3.2 Pool Boiling Heat Transfer in He-II

High field measurements on SRF cavities are routinely done at temperatures below 2.1 K where the state of liquid helium is super fluid. The appearance of super-fluidity only at low temperatures suggests that quantum effects exists on a macroscopic scale, whose character can be explained through the Bose-Einstein condensation model. Therefore, He-II is considered to be an ideal fluid to aid in understanding quantum effects.
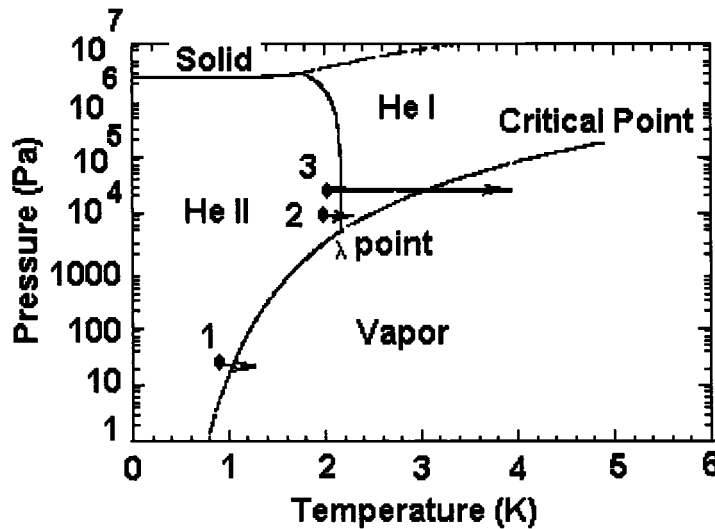
Figure 3.3: Phase diagram of Liquid Helium

As discussed earlier, liquid helium can exist in either of the two phases. Normal helium or He-I exists above T_λ whereas super fluid He-II exists below T_λ. The λ-line as shown in figure 3.3 of the phase diagram, separates these two liquid states. The transition

between these two states of the liquid is associated with a change of slope of the entropy. Thus, the λ-transition is a second-order phase transition and has no latent heat associated with it. The transport properties of He-II are therefore best described through a Two-Fluid Model. This model assumes the He-II to be comprised of two interpenetrating fluids: normal fluid, which contains all the viscosity in the liquid, and the super fluid, which has no viscosity. The normal fluid component of He-II, which must be distinguished from He-I, is assumed to behave as an ordinary liquid. It is described by having density ρ_n, viscosity η_n and specific entropy s_n. On the contrary, the super-fluid component has density ρ_s, no viscosity ($\eta_s=0$) and no entropy ($s_s=0$). The overall properties of the fluid must be comprised of a linear combination of the two components.

$$\rho = \rho_n + \rho_s \tag{3-8}$$

And, since the super-fluid has no entropy, it follows that the total entropy (S) of the He-II can be written in terms of the product of the normal fluid components alone:

$$S = \rho s = \rho_n s_n \tag{3-9}$$

The two-fluid model has successfully explained many unusual phenomena peculiar to He-II such as the fountain effect, thermo-mechanical effect, and the second sound in He-II, the details of which are given in reference [17]. However, it must be realized that this is just a hypothesis and the existence of super-fluid and normal fluid components may not be taken too literally.

Unlike common fluids, the heat transfer from a solid boundary to He-II occurs at a very thin interface. In this process, surface heat transfer is more controlled by the interfacial character, including the properties of the solid rather than that of the bulk He-

II alone. In general, there are two regimes of interface surface heat transfer in He-II. At low ΔT, no boiling occurs and the heat transfer is controlled by a phenomenon called Kapitza conductance. At high ΔT, and for heat fluxes greater than q^*, the surface is blanketed by a film of He-I, or vapor, or both, depending upon the bath conditions of the He-II. In this region, primarily the character of this film controls the heat transfer. As shown in figure 3.3, if the state of He-II corresponds to point 1, then the surface will be blanketed by the helium vapor. If it corresponds to point 2 with q not very high, then the surface will be blanketed by He-I surrounded by He-II. If it corresponds to point 2 with a heat flux greater than q^* then the surface would be blanketed by both He-I and vapor. For operation of SRF cavities, thermal magnetic simulations have shown that due to the characteristically small temperature rise, this research concerns itself with the first problem, that is of heat transfer directly from the solid surface into the liquid He-II, or Kapitza conductance.

3.3 Kapitza Conductance

In 1941, Kapitza [43] observed the first evidence of thermal boundary resistance (R_{Bd}) at the interface between solid and He-II. During his experiment to study the flow of heat around a copper block immersed in the liquid He-II, he observed that within the He-II the temperature gradients were negligible. However, a considerable temperature difference occured between the copper block and the He-II. Analogous to conventional heat transfer coefficient, by definition, the Kapitza conductance (reciprocal of boundary resistance) is defined in the limit where q and ΔT_s are vanishingly small, that is,

$$\frac{1}{R_{Bd}} = h_{ko} = \lim_{\Delta T_s \to 0} \frac{q}{\Delta T_s}$$

(3-10)

here, the 0 subscript refers to the limit as $\Delta T_s \to 0$. This quantity, h_{ko}, has a quite strong

temperature dependence going as T^n with n varying anywhere from approximately 2 to 4.

A more general definition of Kapitza conductance, for small ΔT, is to simply relate it to

the finite values of q and ΔT_s:

$$h_{ko} = q \, / \, \Delta T_s \qquad\qquad (3\text{-}11)$$

It is important to note that the equation 3-11 is valid only for experiments with low

values of heat flux (approximately from 10 mW/cm^2 to 40 mW/cm^2) and the T_s remains

smaller than the super-fluid transition temperature [35]. However, for many practical

engineering applications of He-II involving large heat fluxes, large ΔT_s ($\approx T_{bath}$) may be

encountered resulting from large heat flux imposed on the surface. It follows that the

Kapitza conductance for finite ΔT_s is larger than h_{ko} by the magnitude of this expression

[17],

$$h_k(\Delta T) = h_{ko}\left[1 + \frac{3}{2}\frac{\Delta T_s}{T_b} + \left(\frac{\Delta T_s}{T_b}\right)^2 + \frac{1}{4}\left(\frac{\Delta T_s}{T_b}\right)^3\right] \qquad\qquad (3\text{-}12)$$

where, for $\Delta T/T_{bath} \approx 0.5$, the bracketed quantity is approximately 2. This relation is an

analytic expansion of a more general equation, equation 3.13, to describe heat transfer

rate in the Kapitza regime with an exponent n = 4. It is given as:

$$q = a(T_s^n - T_b^n) \qquad\qquad (3.13)$$

here a and n are adjustable parameters. This equation obtained from phonon radiation

laws [17] has close resemblance to photon radiation. The expansion given in equation 3-12

makes the initial assumption of an explicit T^3 dependence of h_{ko}. However, experimental

observations vary considerably from this exact form, obeying power laws varying between T^2 and T^4.

When the discovery was first made, it was thought that this resistance ($R_{Bd}=1/h_{ko}$) was due to some special property of super-fluid helium. Only later was it realized that such a Kapitza resistance, exists at the interface between any pair of dissimilar materials. In non-boiling He-II, the heat transfer coefficient is all the result of Kapitza conductance. Although the Kapitza conductance is an experimentally defined quantity, the considerable theoretical work aimed at understanding this complex phenomenon helps in analyzing different aspects associated with the transfer of heat that can have practical applications on SRF cavities.

Unlike the conventional concepts such as treating the convection heat transfer coefficient through the properties of the fluid only, such as its thermodynamic state and its velocity profile, understanding of the Kapitza conductance is obtained through the properties of interacting phonons of both the liquid helium as well as the solid. Phonons can be visualized as quantized lattice vibrations, similar to photons in EM wave theory. Their effect on the Kapitza conductance can be accounted for through:

- Number of carriers (phonons) incident on the interface
- Energy carried by each phonon.
- Probability that each phonon is transmitted across the interface.

Different models have been theorized to interpret the physical understanding of this phenomenon. Each of these theories distinguish themselves as to how they model the phonon transmission probability, that is, the total fraction of the energy transmitted across the interface. Enhanced phonon transmission implies an increase in Kapitza conductance.

3.3.1 Acoustic Mismatch Model (AMM)

In 1952, Khalatnikov [19] presented a model approximating what is now known as acoustic mismatch model (AMM), to explain the thermal resistance at the boundary interface. The acoustic mismatch is extremely large at the interface between helium and most ordinary solids because the density and sound velocity of helium are very much less than for other materials. However, Mazo and Onsager in 1955, independent of Khalatnikov's model, gave the modern form of acoustic mismatch model, which takes care of some other channels of phonon interactions through internal reflections and are discussed later in the section. Although quite a comprehensive review of the AM model is available [18], [19], only some of its salient features are presented here.
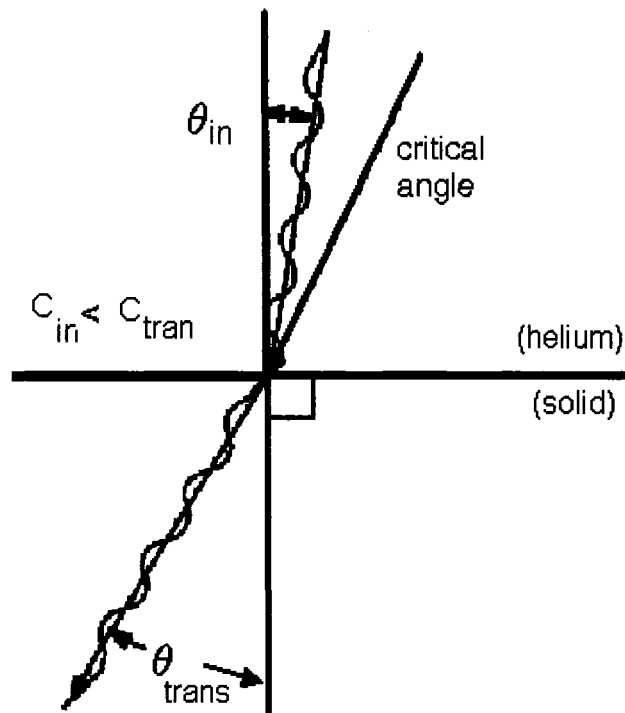
Figure 3.4: Incident and transmitted phonon angles, related according to Snell's law. If the velocities and angles of the incident and transmitted phonons are C_{in}, θ_{in}, C_{tran}, and θ_{tran}, respectively, then $\sin \theta_{in}/C_{in} = \sin \theta_{tran}/C_{tran}$ (Adapted from Swartz et al. [18])

- In this model, it is assumed that the phonon system is governed by continuum acoustics.

- The interface is treated as a plane and, as shown in Figure 3.4, the phonons are treated as plane waves in a continuous medium.

- The phonons transmit specularly without any scattering at the interface.

- The interface has no intrinsic property but merely joins the two grains. As an example, the AM model gives the phonon energy transmission coefficient t_{AB} in material A incident normal to the interface with material B as:

$$t_{AB} = \frac{4Z_A Z_B}{(Z_A + Z_B)^2}$$

here, $Z = \rho c$ is the acoustic impedance (analog of Fresnel equations), with c and ρ being the speed of sound and mass density, respectively.

3.3.2 Diffuse Mismatch Model (DMM)

While the AMM was able to explain the existence of Kapitza resistance, the value of R_k (or $1/h_k$) calculated was between 10 and 100 times larger than typical experimental values measured at 1 to 2 K. This indicates that phonons are able to cross the interface more easily than expected. A crucial assumption made in AMM is that no scattering occurs at the interface. However, various phonon scattering measurements reveal that significant phonon scattering takes place especially for high frequency phonons (> 100 GHz) at helium-solid interface. This scattering of phonons leads to a significant reduction of the thermal boundary resistance by opening up new channels for heat transport. This

effect of phonon scattering resulted in Diffuse Mismatch Model, first presented by Swartz in 1987. The salient features of this model are [18]:

- Assumes that the transmittance of phonons on the interface is a diffuse phenomenon as oppose to specular.

- All phonons striking an interface from both sides lose memory of from where they came.

- The fraction of energy transmitted is independent of the structure of the interface.

- Scattering probability into a given side is proportional to the phonon density of states on that side and the density of states are proportional to ω^2/c^3; where ω is the frequency of the phonons and c is the speed of sound.

- Since the speed of sound in helium is on the order of 20 times lower than in most solids, the density of relatively low-frequency phonon states in helium is on the order of 10^4 higher than in most solids. This results in almost only forward scattering of the phonons incident on the interface from solid to the liquid helium.

3.3.3   Phonon Radiation Limit (PRL)

The Kapitza resistance has always been found to be lower than predicted by the AMM, often by orders of magnitude, as shown in figure 3.5. This had led to the formulation of the so-called phonon radiation limit, sometimes referred to as the perfect match model, was first proposed by Snyder [36] in 1970. The salient features of this limit are [18]:

- PRL is not a new model but a limit at which the maximum possible (phonon-dominated) thermal boundary conductance can be achieved.

36

- As an extension of AMM, it is assumed that all the phonons from the solid side (a side with lower phonon density) are transmitted. From the helium side (with higher phonon density), precisely enough phonons are transmitted to satisfy the principle of detailed balance (i.e. no more than all the phonons from the solid can be transmitted) and second law of thermodynamics.

- Although this is the maximum transport that is allowed by the principle of detailed balance, no physical mechanism is described that allows precisely the correct number of phonons to transmit from the side with higher phonon density.

- PRL is not a model but simply a limit, however, due to closer theoretical agreement between the results of this limit and the diffuse mismatch model, the two are sometimes considered equivalent especially in problems involving helium.

Experimentally, there is a large variation in the Kapitza resistance values even for the same material as seen in Figure 3.6. The difference in the theoretical predictions of Kapitza resistance by the two models is also shown with the upper solid line corresponding to AMM and the lower corresponding to DMM with more than two orders of magnitude.
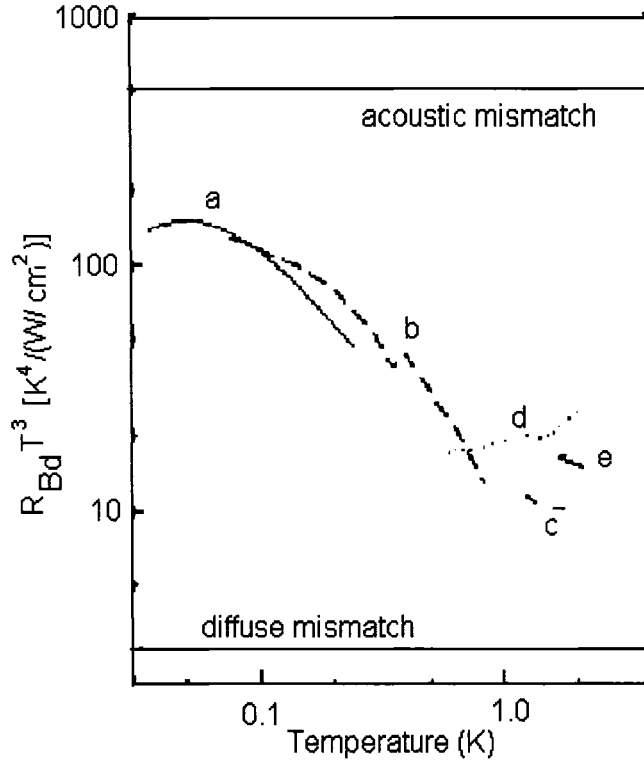
Figure 3.5: Experimental data of various researchers shown as a,b,c,d and, e (adapted from Swartz et al. [18]) for the measurement of Kapitza boundary resistance ($R_{Bd}=R_k$) between copper and He-II, multiplied by T^3 to remove the strong temperature dependence. Note the drop in $R_{Bd}T^3$ with temperature above 0.1 K. The upper solid line is the prediction of AMM and the lower one is the prediction of DMM, almost two orders of magnitude different. The kink in the curve b is the result of irreproducibility of Kapitza resistance even on the same sample from run to run, and does not reflect any physical phenomenon.

3.4 Factors Affecting Kapitza Resistance

As mentioned earlier, the SRF cavities are routinely made from pure Nb which becomes a superconductor at temperatures below T_c = 9.2 K. The metal has a characteristic Debye temperature of θ_D =275 K, which is above average for common elements used in cryogenics [17]. Debye theory of materials has been very successful in predicting the low temperature heat capacities of various solids by treating the solids as infinite elastic continuum and considering the excitement of all possible standing waves

38

in the material. With this in mind, it is easier to remain focused on the present research while analyzing the trend of numerous experimental studies done to categorize the effect of solids on Kapitza resistance. In many of the experiments, the effect of damaging or oxidizing the surface of the solid has been ambiguous. It has been even observed [20], [21] that the lowest Kapitza resistances corresponded to samples with the least damaged surfaces, contrary to the present understanding. Such trends imply that the boundary resistance to dense, soft (low-Debye-temperature) solids will be much closer to the prediction of AMM than will be the boundary resistance to light, hard (high-Debye-temperature) solids. Thus, the trend is found [18] independent of whether the solid is metallic or dielectric. This conclusion is also confirmed through another analysis [22], when a plot of reduced boundary resistance, let us say P (reduced logarithmically so that a value of 1 corresponded to AMM and a value of 0 corresponded to DMM), is made against $T\theta_D$, the product of temperature and the Debye temperature of the solid. This plot is reproduced in Figure 3.6 [22]. As seen in this plot, for a given solid, $R_{Bd}T^3$ drops from near the AMM prediction at low temperatures toward a very low value at high temperature. By plotting the reduced boundary resistance as a function of $T\theta_D$, all the data follow approximately the same curve. This is the same conclusion as reached in the case described above where the boundary resistance to solids with high Debye temperatures, such as sapphire or LiF, will drop relative to the AMM at lower temperatures than will the boundary resistance to softer solids, such as lead or mercury. Niobium is clearly shown to be on the middle to lower half of the plot indicating its inclination to follow the prediction of DMM as compared to AMM, especially at temperatures around 1.8 to 2.1 K.
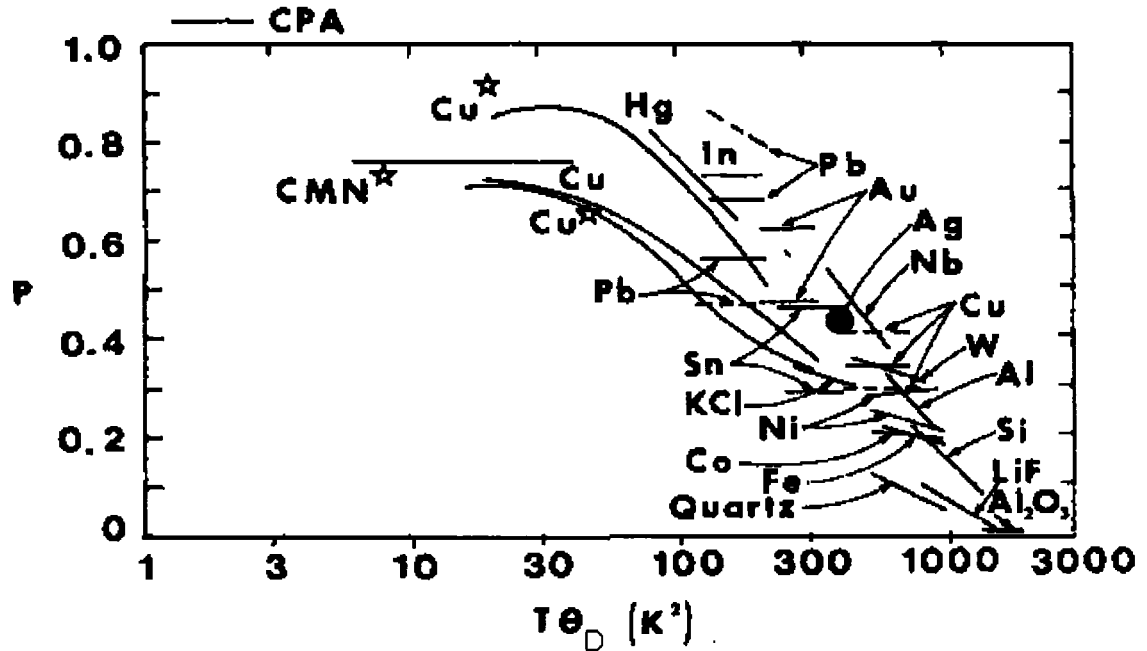
Figure 3.6: Plot of the reduced thermal boundary resistance P as a function of Tθ_D. The stars indicate measurements between the solid and ^{3}He. The data is by several researchers and compiled by Swartz et al [18].

The analysis of much of the existing Kapitza resistance data often involves the proposal of a new transmission mechanism or "channel". No single channel can be responsible for all the observations, rather, for a given observation, several channels may contribute. For different interfaces, different channels may be important. Some of the commonly known channels are discussed in the subsequent paragraphs.

3.4.1 Effect of Boundary Layer

At the interface between He and a solid, due to strong van der Waals attraction forces, the (first few mono layers) boundary layer thickness is around 30 Å. The pressure in this boundary layer is very large on the order of tens of atmosphere. Therefore, this boundary layer is thought [18] to be acting as an anti-reflective coating. For long-wavelength phonons, i.e. at temperatures less than 0.1 K (the wavelength in the layer is much longer

40

than the thickness of the layer), the effect of a dense layer would be small. There is no drop in Kapitza resistance, R_k, and the effect of the boundary layer remains small. For shorter-wavelength phonons, however, i.e. at temperatures more than about 0.5 K, (wavelength in the layer comparable to four times the layer thickness), the layer could greatly enhance the transmission. Hence the drop in Kapitza resistance is quite evident.

3.4.2 Effect of Pressure

As we know, the speed of sound in helium is a strong function of pressure. Thus, AMM would predict great pressure dependence for Kapitza resistance. However, as seen from Figure 3.7 [18], R_k has pressure dependence only at temperatures less than 0.5 K. At temperatures above 0.5 K, the R_k is almost independent of pressure. Close similarity of Kapitza resistance of ^{3}He plotted in figure 3.8 with that of ^{4}He in figure 3.6 is also quite evident.

This effect of the pressure independence of Kapitza resistance at temperature above a few tenths Kelvin has also been explained by observing that the pressure in the interfacial layer (due to van der Waals attraction) is very large and is independent of the pressure of the bulk. At low temperatures, where the boundary layer is unimportant, the pressure dependence is unaffected by the layer, but at temperatures where the boundary layer is important, pressure dependence is reduced.
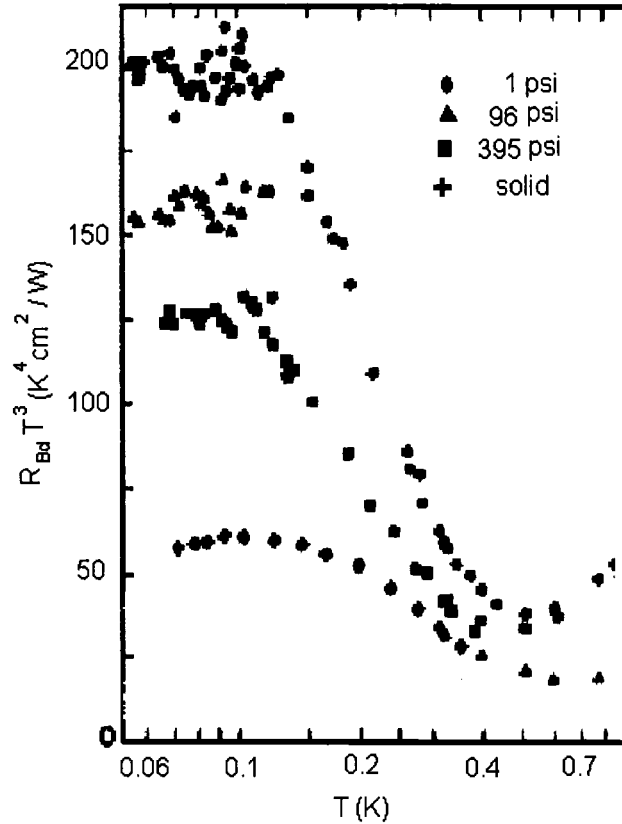
Figure 3.7: Measured Kapitza resistance between electro-polished copper and ^{3}He, multiplied by T^3 to remove strong temperature dependence. The pressure dependence is seen well below the 0.5 K, but near 0.5 K and above, the Kapitza resistance is nearly pressure independent. Adapted from Swartz et al [18].

3.4.3 Effect of Attenuation

The effect of attenuation is to broaden the critical cone and lower the predicted value of R_k. In the case of Kapitza resistance, with reference to AMM, if the phonon from the helium side is incident upon the interface from outside the critical cone (see figure 3.4), the phonon will be totally internally reflected. An evanescent wave is generated in the solid to satisfy the boundary condition. An evanescent wave is an electromagnetic wave observed in total internal reflection, undersized wave-guides, and in periodic dielectric hetero-structures. While wave solutions have real wave number k, k for an evanescent

42

mode is purely imaginary. Though the amplitude of this evanescent wave decreases exponentially with respect to distance within the solid, the coupling of energy transfer across the interface does take place. Thus the total internal reflected phonon can end up being transmitted. Physically, this effect is accounted for by including classical phonon attenuation in the model. As much as factor of three reductions in R_k has been approximated due to attenuation. It is this effect that results in modified AM model.

3.4.4 Effect of Conduction Electrons

In addition to the effects of electrons in metals attenuating phonons and thereby broadening the critical cone, other significant effects of electrons on thermal boundary resistance are through:

- Magnetic Field Effects: The effect of the conduction electrons in superconductors can be expected at a Kapitza interface. When the metal is in a superconducting state, the electrons play little or no role. The application of a magnetic field to drive the superconductor "normal", allows the electrons to contribute to the thermal transport process across the interface. However, due to extremely small electronic contribution, direct measurement of this effect still remains inconclusive.

- Effect of Oxide Layer: Halbritter et al [23], [24] has suggested a relationship between the observed RF losses at non-ideal metal surface interfaces and the observed phonon scattering at such interfaces. The coupling arises because electrons can be localized in, for example, oxide layers at the metal surface. Phonons incident on these localized electrons cause them to vibrate and generate RF fields, which interact with other localized electrons. The result is strong diffuse scattering and therefore, a reduction in Kapitza resistance. Some models have also been proposed [25] for the microscopic

interactions of trapped individual and coupled electrons in thin oxide layers. This also may relate directly to diffuse phonon scattering.

3.4.5 Effect of Localized States at the Interface

All non-acoustic channels invoked to couple phonons across a boundary require excitations at the interface, which couple phonons on both sides of interface. If a surface contains a large density of defects or loosely bound impurities, then their excitations can couple the phonons on both sides of the interface through surface waves. It has been shown by Gel'fgat and Syrkin [26] that a layer of loosely bound impurities on the surface could increase phonon transport across the interface by coupling through surface waves. Some models have also been proposed [27], [28] by assuming the defects as localized masses and springs. These defects and loosely bound impurities promote the coupling between bulk phonons and the surface acoustic waves, which couple to the phonons in the helium. However, the model has not been worked out quantitatively in three dimensions due to complications introduced by the inclusion of phonon attenuation and boundary layers.

3.4.6 Effect of Surface Roughness

The acoustic mismatch theory (AMM) assumes perfect, planner interfaces. There exists experimental evidence [29] to support this theory whereby the in-situ cleaving of a LiF crystal at 1 K created a nearly ideal surface. The experimental result demonstrated excellent agreement with AMM. However, real surfaces are usually quite rough on the scale of hundreds of Å, i.e. the typical phonon wavelength in solids at 1 K.
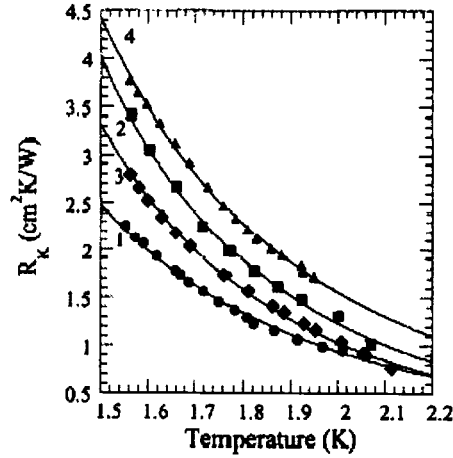
Sample #; RRR	Surface Treatment	$\sigma_{rms}(\mu m)$	$R_K (cm^2 K/W)$	R_K at T= 1.8 K
# 1 (●); 178	CE(~30µm)	1.8 ± 0.4	10.7 x T^{-3.55}	1.328
# 2 (■); 178	EP	0.85 ± 0.25	21.3 x T^{-4.11}	1.902
# 3(◆); 647	A+CE (~30µm)	1.3 ± 0.4	16.1 x T^{-3.93}	1.598
# 4 (▲); 647	A+CE +EP	0.2 ± 0.1	19.1 x T^{-3.61}	2.288

Figure 3.8: A Kapitza resistance of the four samples, along with their surface treatment and corresponding roughness data are shown in the chart. The graph shows the relative effect of surface roughness on R_K with temperature variation. CE stands for chemical etch, EP means electropolishing and, A stands for annealing. (Adapted from Amrit et. Al. [31])

One of the effects of surface roughness is to couple bulk phonons (or other excitations) on either side of the interface through Rayleigh (or surface) waves. The phonons with wavelengths comparable to the characteristic dimension of the roughness are most strongly scattered, hence, lowering the Kapitza resistance. Since the wavelength of the phonons increase as the temperature is lowered, a larger length scale surface

45

roughness start interacting in the scattering of phonons. This is seen as an increase of Kapitza resistance with lowering of temperature.

A variation of Kapitza resistance with temperature must be expected. This effect is evident in some of the recent experiments conducted by Amrit et al. [30], [31] between 1.5 K and 2.1 K on well-characterized superconducting Nb samples of different surface roughness with He-II. As clearly seen from figure 3.8 (graph), the effect of an increase in surface roughness results in a decrease in R_k.

The wavelength of phonons in liquid helium is on the order of ~ 4/T nm within the temperature range of 1.5 to 2.1 K [18]. Now on a macroscopic length scales, the ordinary surface contains large number of micro-length scale roughnesses superimposed on the larger scale roughnesses such as seen in figure 3.9. However at micro-length scale levels, we see even smaller (~nm) length scale roughnesses are superimposed on the micro length scale roughnesses. Thus, based upon these observations, it can be argued that increasing the exposed surface area of Nb to He-II at a macro level statistically results in more of the nano-length scale roughnesses. Therefore, increased surface index (SI) of the surface can lead to reduced Kapitza resistance. SI, here, is defined as the ratio of exposed surface area to that of the projected area.
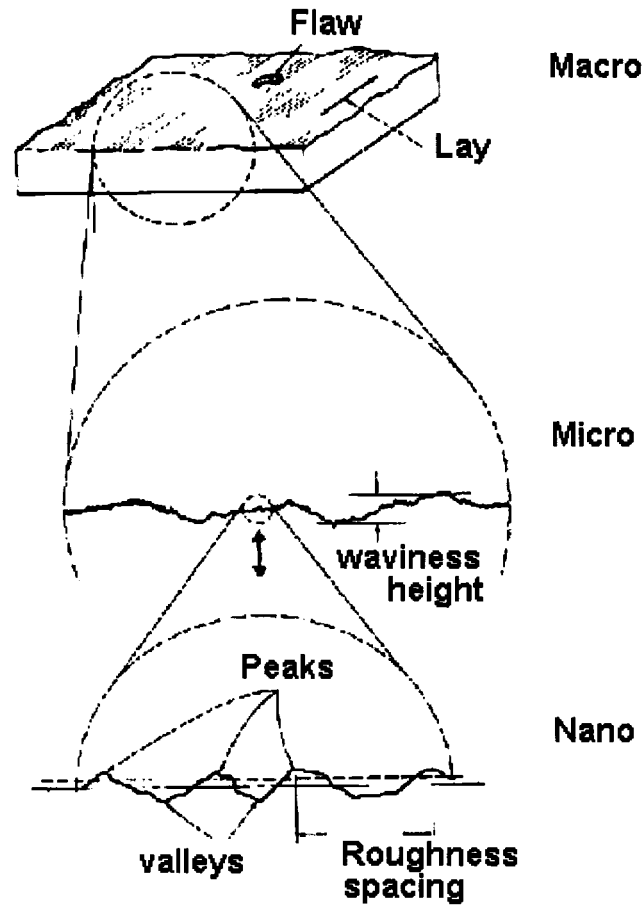
Figure 3.9: Pictorial display of surface characteristics with associated different levels of length scales.

3.4.7 Effect of Titanium Getter Material

As discussed earlier in chapter 1, gettering is a technique in which usually Ti is evaporated on the surface of the Nb to about a 1 µm thick layer. Since Ti has a greater affinity to the interstitial contents (e.g. H, C, O), than does Nb, all of these impurities get attracted towards the surface. After removing this layer from the surface, the metal left behind is much purer with a higher RRR value. The influence of a layer of foreign atoms close to the surface in the solid has also been studied [30]. Here, a distinction must be made between the case of foreign atoms, where Ti has been deposited acting as a solid

layer of almost 30 μm deep into the metal, with those of loosely bound foreign atoms, as discussed in section 3.4.5 above.
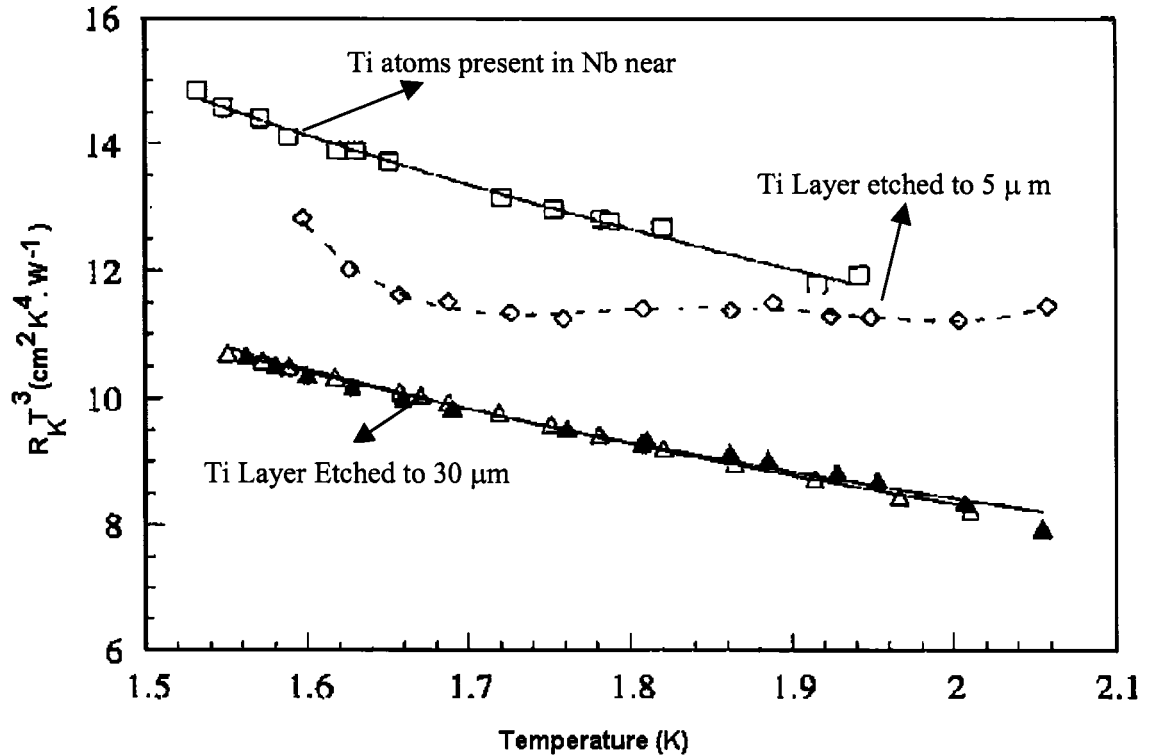
Figure 3.10: Effect of Ti atoms present in Nb near the interface on Rk (Adapted from J. Amrit et al [30]).

In this case, the effect of the Ti layer resulted in an almost twofold increase in the value of R_k. After etching the surface to 30 μm, as shown in the figure 3.10 [30], R_k decreased and became comparable to that of the initial sample within the limits of experimental error.

3.4.8 Effect of Deposited Thin Films on Kapitza Conductance

Phonon scattering experiments have been performed to analyze the effect of surface roughness on the Kapitza conductance. The study has concluded [18] that surface roughness, even at very low amplitude, causes strong geometric and Rayleigh scattering,

suggesting that surface roughness could be a very important transmission channel in the Kapitza conductance. It has been observed that diffuse phonon scattering is directly related to enhanced transmission of phonons across the interface, increasing the observed Kapitza conductance. Thin films of varying thicknesses (usually of the order of few Å to tens of Å) of hydrogen, deuterium, or neon were deposited on a silicon surface [32], [33], [34] to analyze the effect of diffuse phonon scattering at the interface. At low enough temperatures (minimum temperature of measurement was 50 mK), no significant scattering was observed. However, as the temperature was increased, the scattering from the films increased, often with sharp onset. Depending upon the type of thin film, island or continuous, the dominant phonon wavelength at the onset temperatures of diffuse scattering in all cases corresponded to the characteristic dimension of the film, whether it was based on island diameter or film thickness. Other types of films studied included oxides, ion-implanted regions, and metal thin films. The scattering rates, in all these experiments, reached a limit when the film thickness was no more than a few times the dominant phonon wavelength in the film (at a given temperature). This work clearly shows that the phonon scattering from geometric imperfections, such as roughness, adsorbates, or thin deposited films, is very large, causing increased Kapitza conductance.

4 Experimental Apparatus

4.1 Cryogenic Dewar

The most commonly used technique of testing the SRF cavities is through a long cylindrical cryogenic Dewar filled with liquid helium, whose bath temperature is controlled through pressure regulation. Usually the liquid helium is supplied to the testing Dewar through transfer lines at ~ 4.3 K. A schematic diagram of a cryogenic Dewar is shown in figure 4.1, along with the lid assembly carrying sample housing.

The lid assembly for the experimental setup acts as a testing stand, which is inserted into the cryostat Dewar. The lid contains the receptacles for filling with liquid helium, warm gas return and feed-throughs for connecting various sensors on or around the cavity for instrumentation purposes. To minimize thermal losses inside the cryostat, there are a number of layers of insulation surrounding the Dewar. The outermost insulation layer is of a vacuum jacket along with another layer of liquid nitrogen shield to minimize the heat leaks to the interior. A layer of super insulation (multiple layers of aluminized myler) is placed in the room temperature and liquid nitrogen gap, as well as the liquid nitrogen as liquid He gap to further reduce the heat leaking inside the tank. The inside of the Dewar is filled with liquid helium to the desired level. Nucleate boiling heat transfer coefficient measurements are performed at temperatures ~ 4.2 K and 1 atmosphere pressure in He-I. For the measurements of Kapitza conductance, the pressure on the liquid helium is gradually lowered by pumping out He gas to about 23.8 torr so as to bring the bath temperature at 2.0 K. Below 2.175 K, the liquid helium becomes He-II, a super fluid. The quantity of the He in the Dewar is monitored using a superconducting wire as a level sensor.

50
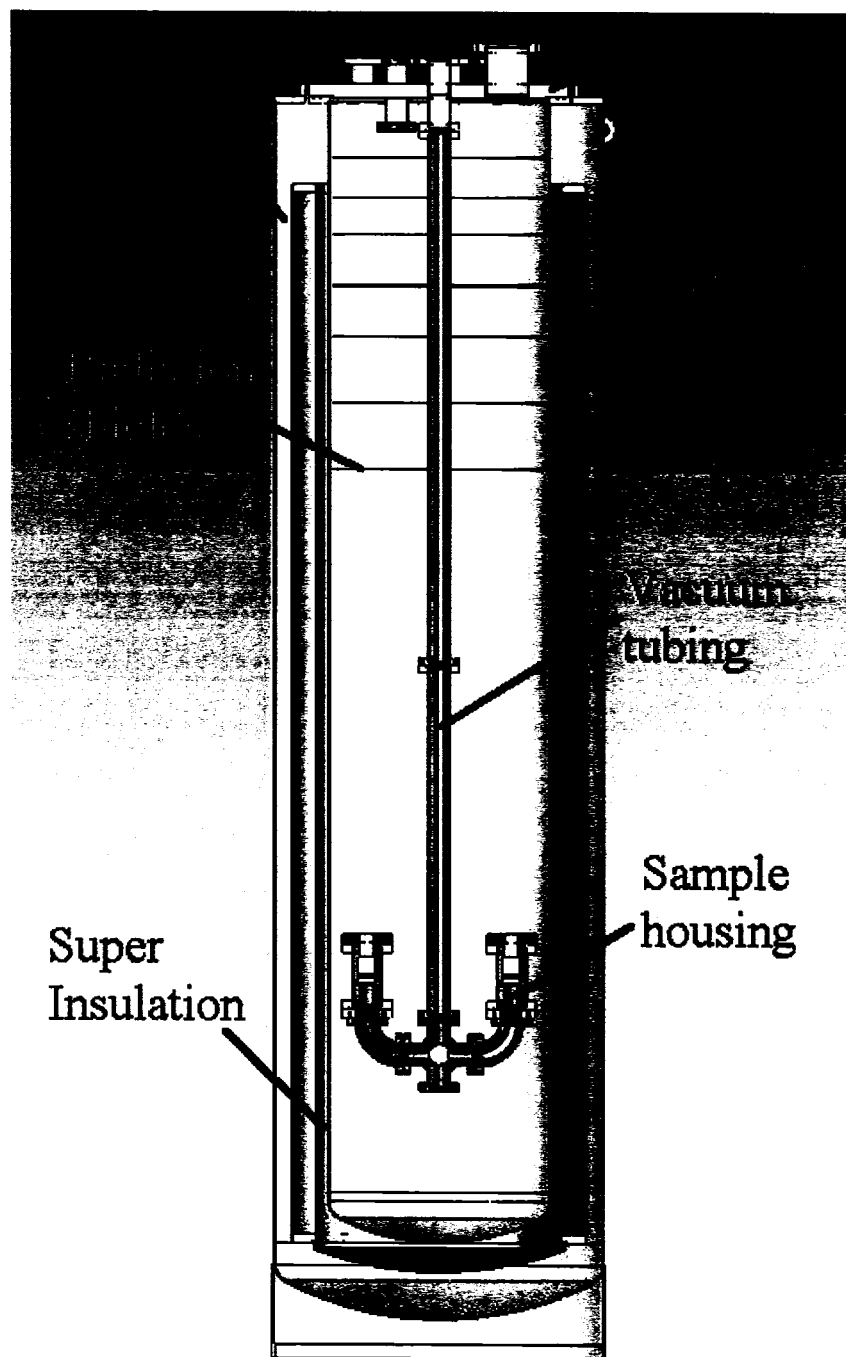
Figure 4.1: Schematic diagram of the cryostat Dewar with experimental setup hooked up on a lid assembly inside the Dewar.

4.2 New Lid Insert Assembly

Since the cleaning requirements for SRF cavities are critical, to avoid contamination to the already existing vacuum line used for testing the SRF cavities, a new lid insert assembly was built for measuring the thermal conductivity and the interface heat transfer coefficient of Nb samples as shown in figure 4.2. The assembly has various ports and feed-throughs mounted on the top of the lid. The lid, the sample housing assembly is mounted on long vacuum tube through a six-way cross Conflat flange and a zero length reducer. Baffle plates are also seen in figure 4.2 for radiation shielding and better insulation from the top end of the Dewar. The description of each component on the lid assembly is discussed in the subsequent paragraphs.
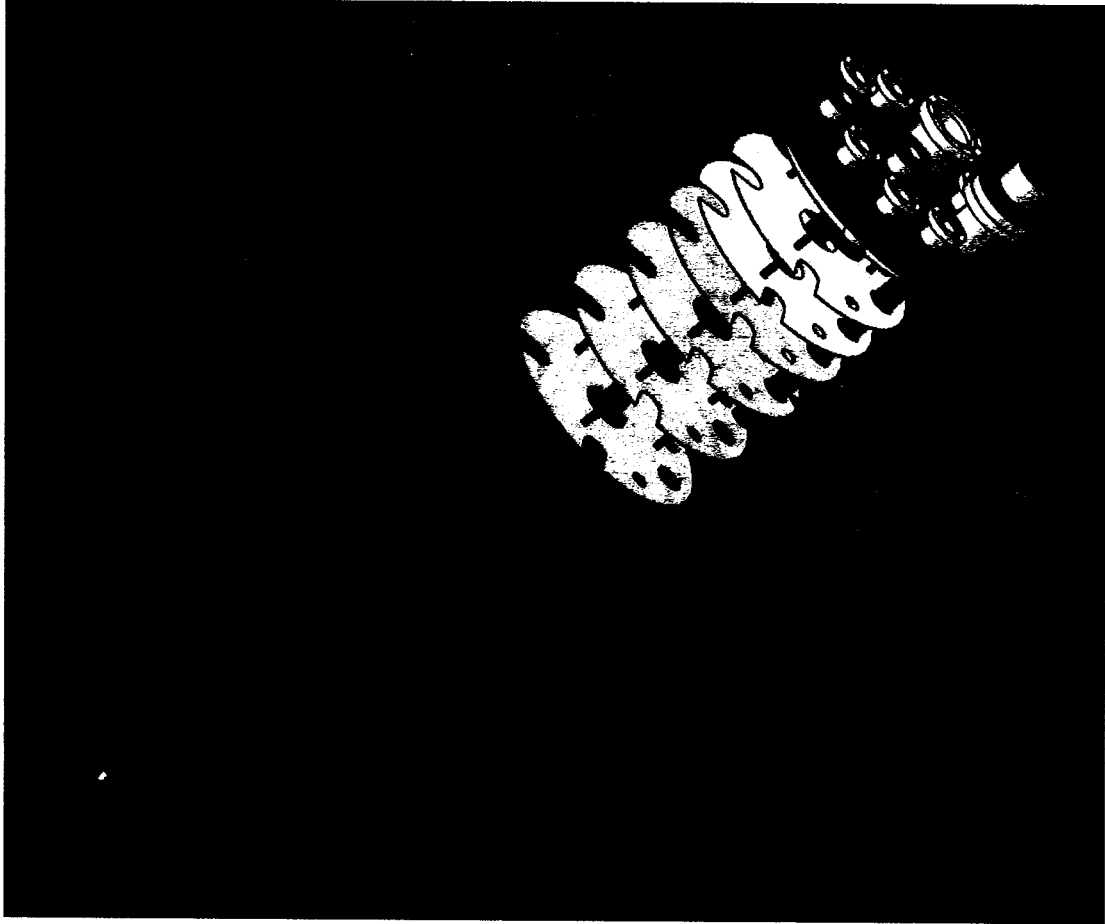
Figure 4.2: New lid assembly carrying two sample holder assemblies.

4.3 Dewar Lid Top Plate

The lid of the cryogenic Dewar has a ~ 2.5 cm thick stainless steel base plate with various ports and receptacles attached to it. The top view of the plate is shown in figure 4.3. The vacuum port, shown in the center of the figure, provides not only a line connection to the vacuum pump but also a port for electrical feed-through for sensors and heaters that are mounted on the sample holder assemblies inside the vacuum chamber. Essentially everything outside this vacuum port on the lid is on the liquid helium side of the cryostat Dewar. Provision of the heater port, as shown in figure 4.4, on the helium side allows quick boil off of left over helium to warm up the Dewar after completion of the experiment. To physically see the liquid helium inside the Dewar, a viewing port is also provided on the lid top plate. A port for the pressure transducer is provided to monitor the helium vapor pressure inside the Dewar. Some of the ports have been intentionally left blank for future expansion / needs.

4.4 Thermal Radiation Shields

On the underside of the lid, there are seven thermal radiation shields, as shown in figure 4.2 and 4.5, which are made of 6061T6 Aluminum alloy. The shields have access holes drilled through them to provide space for passing electrical wiring, and pipelines for vacuum, helium fill, and gas return.
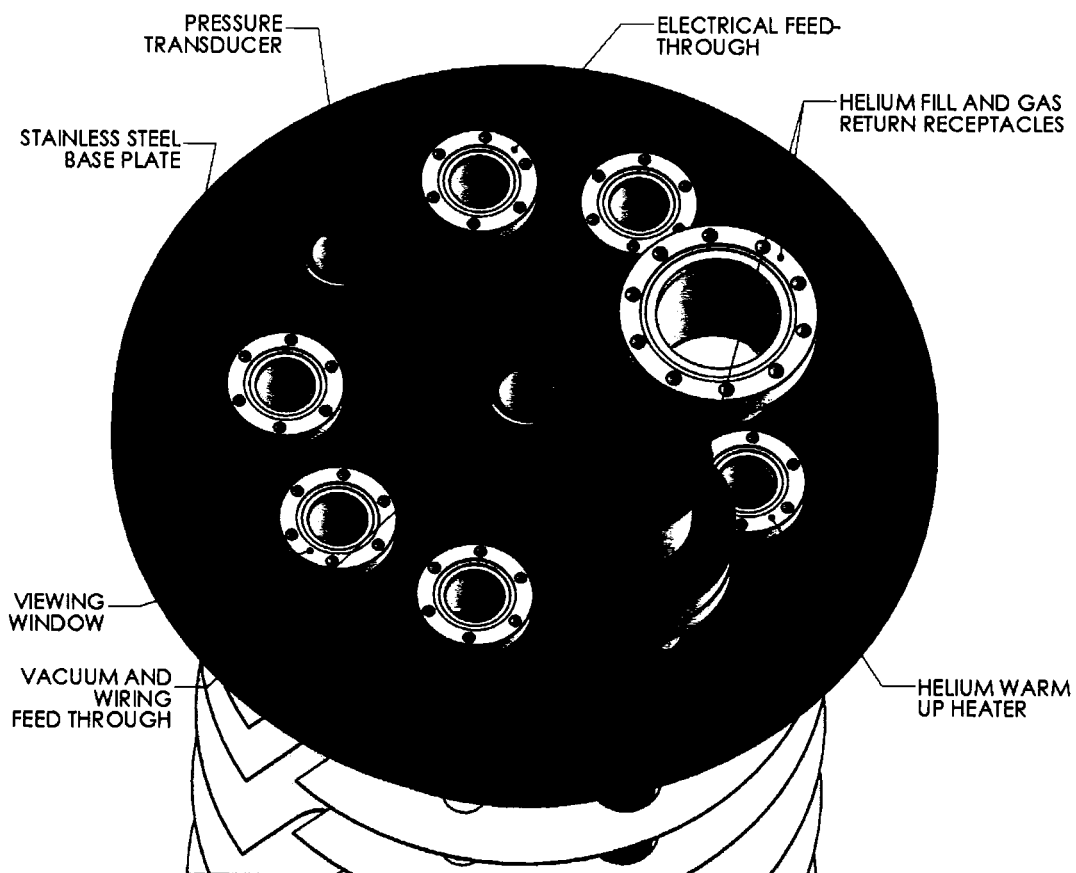
Figure 4.3: Dewar lid top plate with various ports and receptacles

4.5 Sensors and Wiring on Liquid Helium Side

A specially built [39] multi-connector electrical feed through, as shown in figure 4.4, is mounted on the lid plate to accommodate all the interconnection wiring requirements on the helium side of the Dewar. Standard ribbon cables and connectors, as shown in figure 4.5, are used inside the Dewar to carry electrical signals from the sensors to the feed through at the top of the lid. Three platinum temperature sensors having temperature measurement range from room temperature to 30 K are mounted on the thermal shields for estimation of heat leaks through the lid. They are located on the top, middle and bottom shields as shown in figure 4.5. Usually the top shield sensor varies in temperature from 300 K to 285 K, indicating good thermal insulation. The bottom shield temperature sensor remains below its calibration limits most of the time when the liquid helium level is closer to it, but occasionally rises to ~ 35 K as the liquid He level drops to the bottom of the tank. To measure the level of liquid helium, a He level sensor is also mounted on one of the stainless steel support rods used for holding the thermal shields in place. This is a 30 inches long (29 inches effective length) He level sensor supplied by American Magnetics, Inc. Other than the temperature sensors on the radiation shields, there are two Ge temperature sensors to measure the bath temperature of the bulk liquid helium, one in the open bath conditions and the other is inside the stainless steel tube, closer (~ 1-2 cm away) to the sample interface surface as shown in figure 4.6.
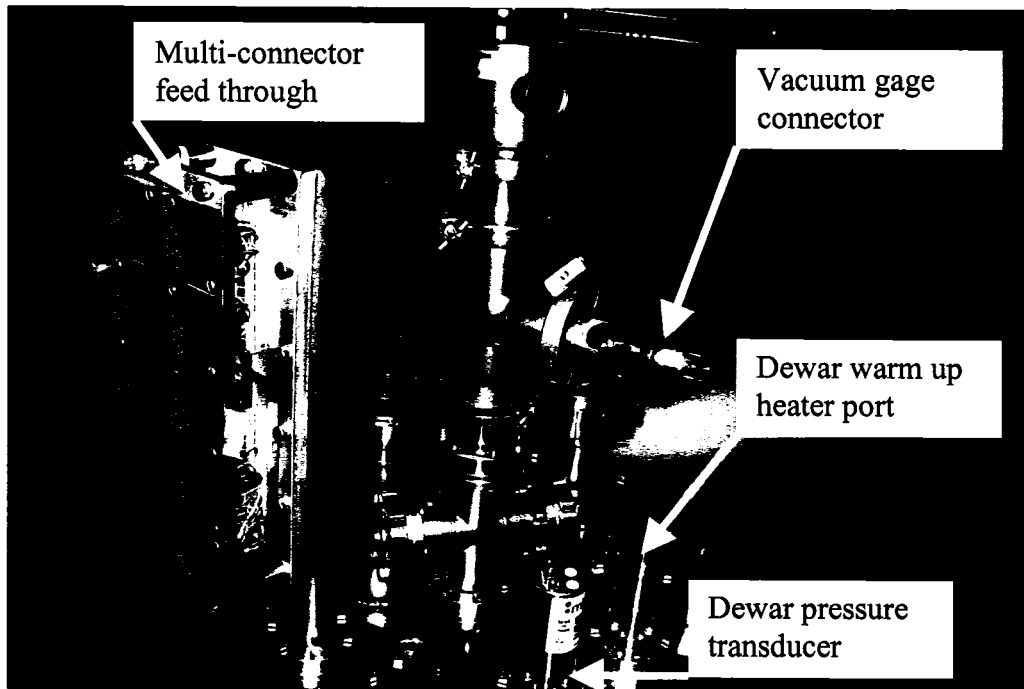
Figure 4.4: Top plate of lid assembly has various ports and feed-through assemblies. Multi-connecter electrical feed-through is a custom made assembly designed and assembled at NSCL [39]
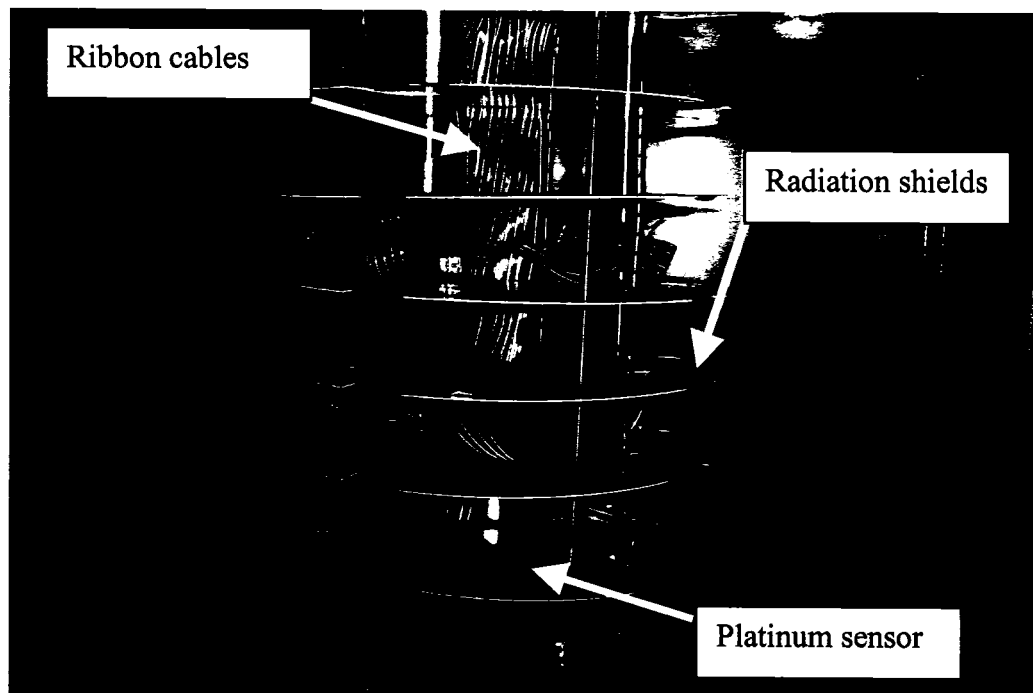
Figure 4.5: Ribbon cables from the multi-connector feed-through on the top plate are passing through the radiation shields. A platinum sensor is shown on the lower shield.
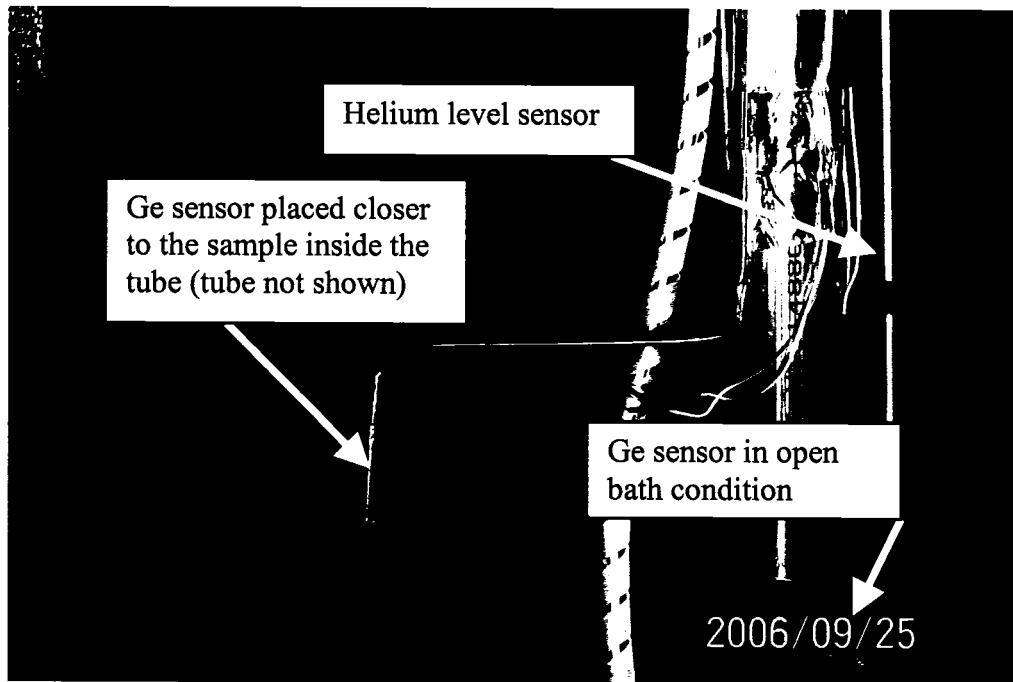
Figure 4.6: Helium level and temperature sensors are placed in liquid helium.

4.6 Housing for Sample Holder Assemblies

At the very bottom of the vacuum pipe on the lid of figure 4.2, there are two housings for sample holder assemblies mounted on a six-way cross Conflat flange. A close up view for this part of the lid assembly is shown in figure 4.7. The set up can be extended for additional two housings on this flange, however, for the present study, only two of them are used for testing two Nb samples at a time. A zero length reducer is used to connect 3 3/8" Conflat flange housing with the 2 3/4" six way cross Conflat flange.

4.7 Sample Holder Assembly

The sample holder assembly, shown in figure 4.7, consists of a standard 3 3/8" Conflat flange with an opening in the middle of the flange for a thin stainless steel tube (2.5 cm diameter). The full view of this assembly is redrawn in figure 4.8 (a). The one end of the tube is welded flush with the top end of the Conflat flange whereas the other end has a knife-edge surface to cut through the Nb sample for sealing against the vacuum leakage. There are six symmetric blind tap drill holes on the sealing end side of the Conflat flange for attaching the six threaded support rods for holding the sample base plate, and are shown in figure 4.8 (b). The stainless steel base plate holds an insulating circular disc of G-10, a thin foil heater, a 5 mm thick copper disc and the cylindrical Nb sample, all in the same order of arrangement. The six stainless steel threaded rods, as also shown in figure 4.9, on the base plate are then hand tightened against the bottom end of the Conflat flange in the holes provided for them. In this configuration, the knife-edge of stainless steel tube cuts deep enough into the Nb sample to seal the vacuum effectively.
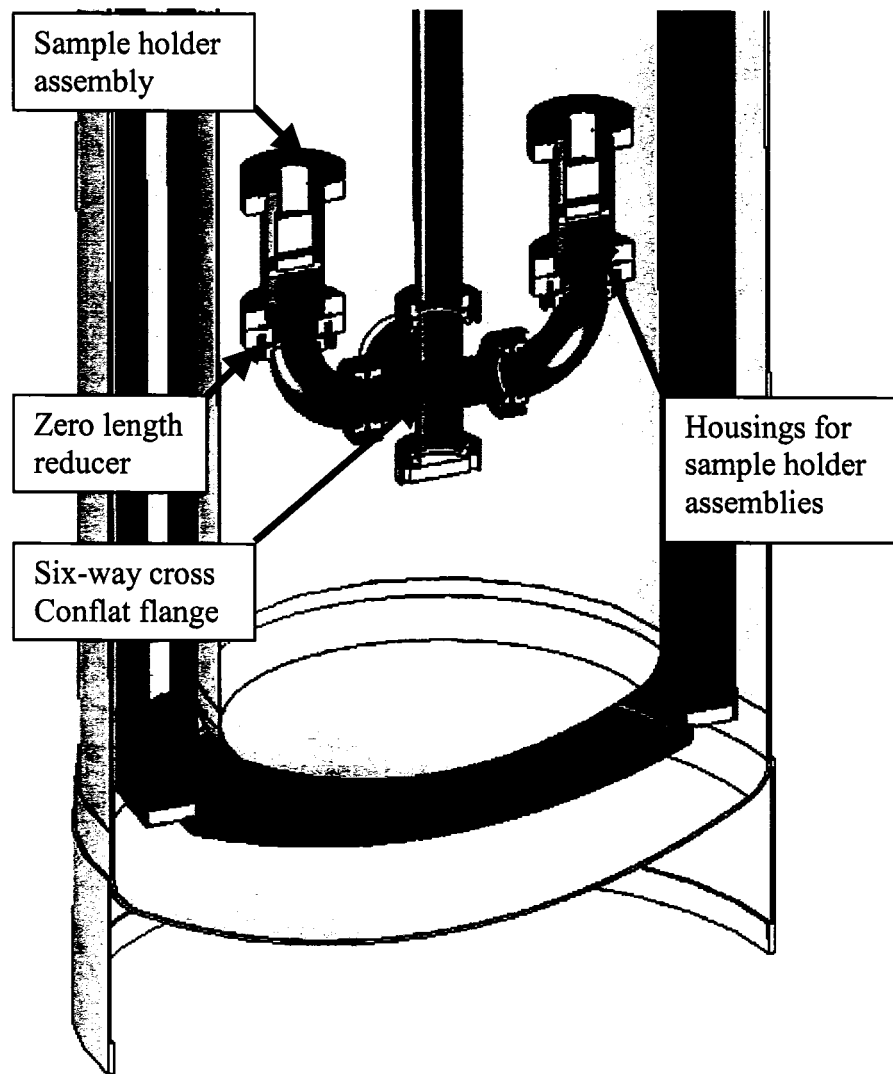
Figure 4.7: Cut away view of the housings for sample holder assemblies mounted on the six-way cross conflate flange.

(a)

(b)
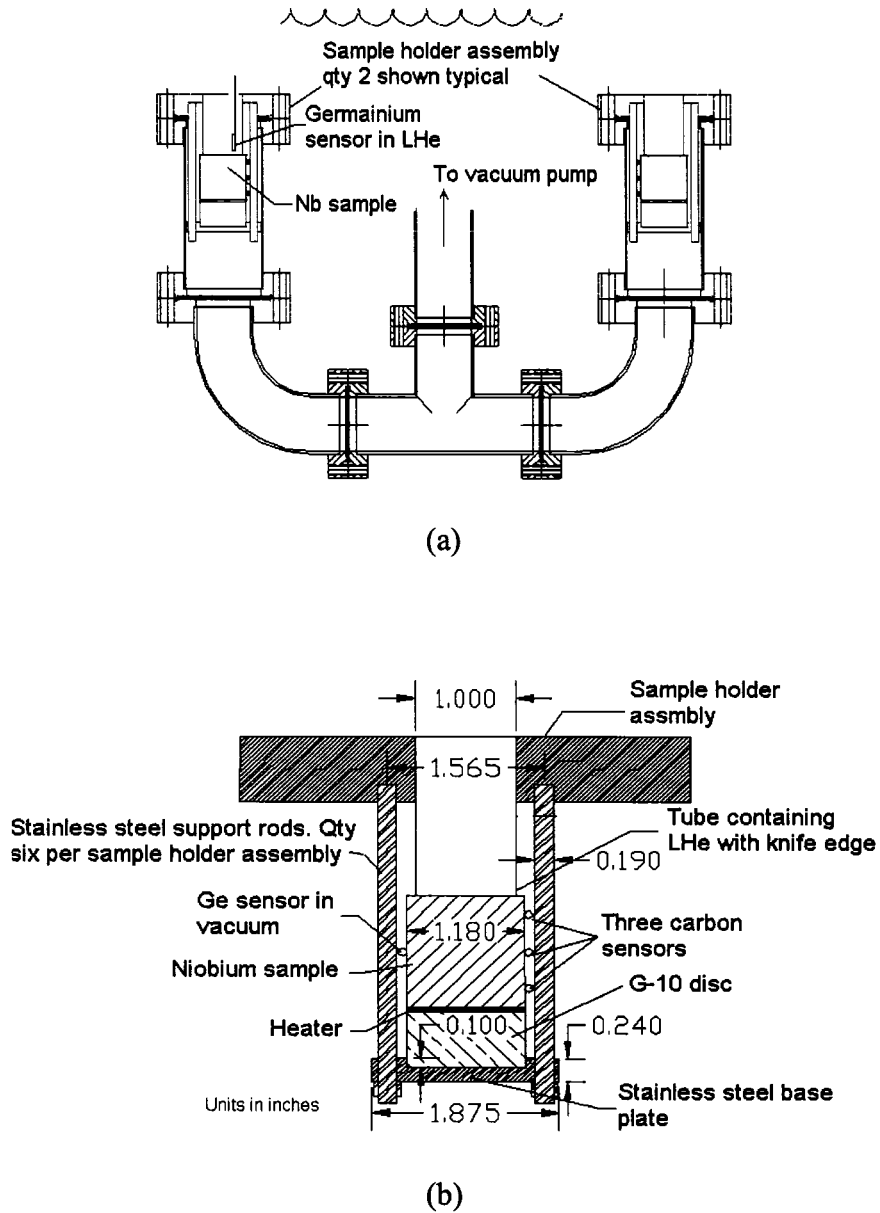
Figure 4.8: The two housing (a) for the two sample holder assemblies (b) are connected to a common vacuum line. This sample holder assembly is used to measure thermal conductivity as well as the interface heat transfer coefficient of the sample simultaneously in one experimental setting.

61

Despite several thermal cycles of the assembly down to 1.6 K from 300 K and back again over a period of several months, the sealing remained effective, maintaining the vacuum pressure down to mtorr vacuum pressure levels.

4.8 Sample Heater

A thin (~ 0.3 mm) foil heater, as shown in figure 4.9 is supplied by Minco® and is pasted on a copper disc (5 mm thick) to provide a homogeneous heat flux, into the Nb sample. Typical voltage (~100 mV) and current (~0.5 mA) measurements for power calculations are made with the help of digital meters with resolution of 1 mV and 1 μA respectively. As mentioned in the last section, the power leads to the heater need special attention for minimizing the heat leakage into the sample through their high thermal conductor copper wires. Cold sinking the wires at several locations all along the length of the vacuum tube provides adequate thermal isolation. However, closer to the heater end, the nearest cold sink is provided at least 5 cm away from the heater, just to avoid the heat from the heater when it is switched on for test, flowing back through the wires into the cold sink. Error induced due to such heat leaks are analyzed in appendix C.

4.9 Temperature Sensors and Wiring in the Vacuum

There is a wide range of sensors available in the temperature range of 1.5 K and above. Carbon sensors (100 ohm 1/8 W Allen Bradley resistors) are the most commonly available and the least expensive. Carbon sensors are remarkably good in low temperature measurements. Since their resistance increases exponentially at low temperatures, their sensitivities are better than most of the sensors available for cryogenic use. Typical sensitivity values of a carbon sensor in comparison with a germanium sensor are listed in appendix E.
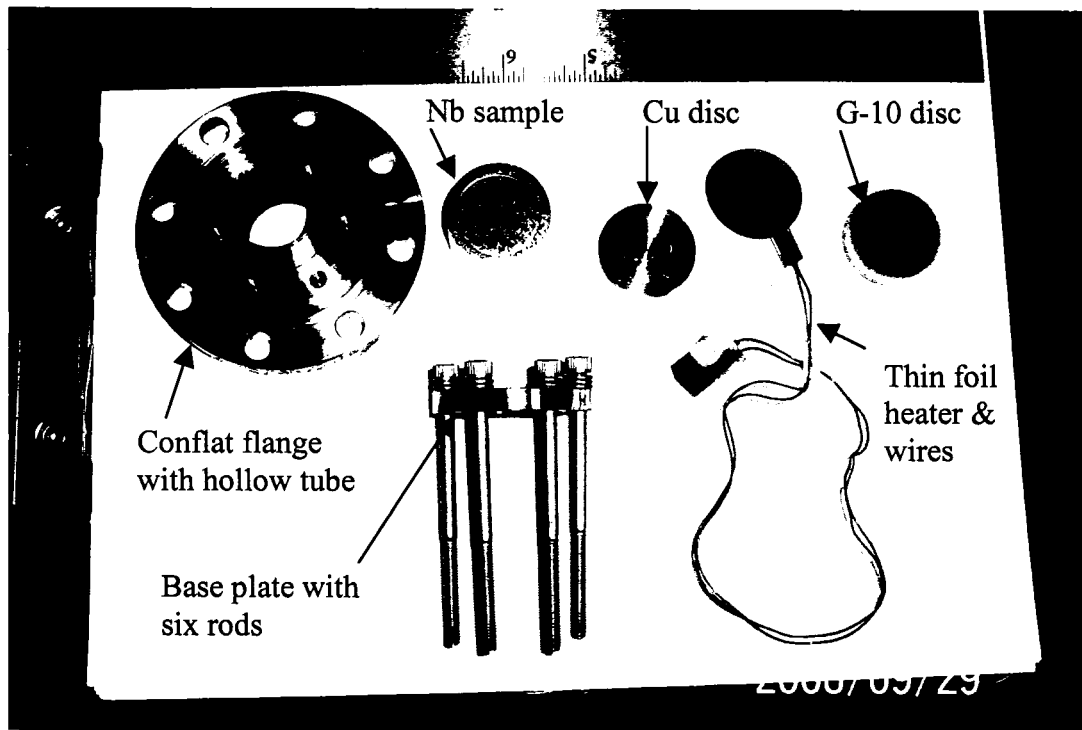
Figure 4.9: Unassembled components of cylindrical sample holder assembly

Each sample has an attachment of three co-linear carbon sensors as shown in figure 4.10 for cylindrical sample and figure 4.11 for flat samples. There is also one 4-wire factory calibrated germanium (Ge) sensor on one of the two samples for in situ calibration of the carbon sensors. Before mounting each carbon sensors, their outer varnish is peeled off and its cylindrical body is made slightly flat with emery cloth on one edge to increase its contact area with the Nb sample. Each sensor is mounted with the help of a Stycast epoxy using a very delicate and careful procedure to ensure that adequate pressure is maintained on the sensor through the curing time of the epoxy. The usual room temperature curing time for Stycast epoxy is ~14 hrs. A good bonding of the sensors with the sample is an important and essential step in the sample preparation for testing at cryogenic temperatures. The carbon sensors are attached with a thermally

insulating 45 cm long 36 AWG manganin wire (provided by LakeShore®). Beyond this 45 cm insulating length of the manganin wire, the signal from the sensors inside the vacuum pipe to the top of the lid is carried through 28 AWG multiple stranded copper ribbon cables. Also, to avoid spurious heat leaks into the test samples, the signal cables for all the sensors as well as for the heaters, are anchored at several places along the length of the vacuum tube to provide adequate heat sinking.
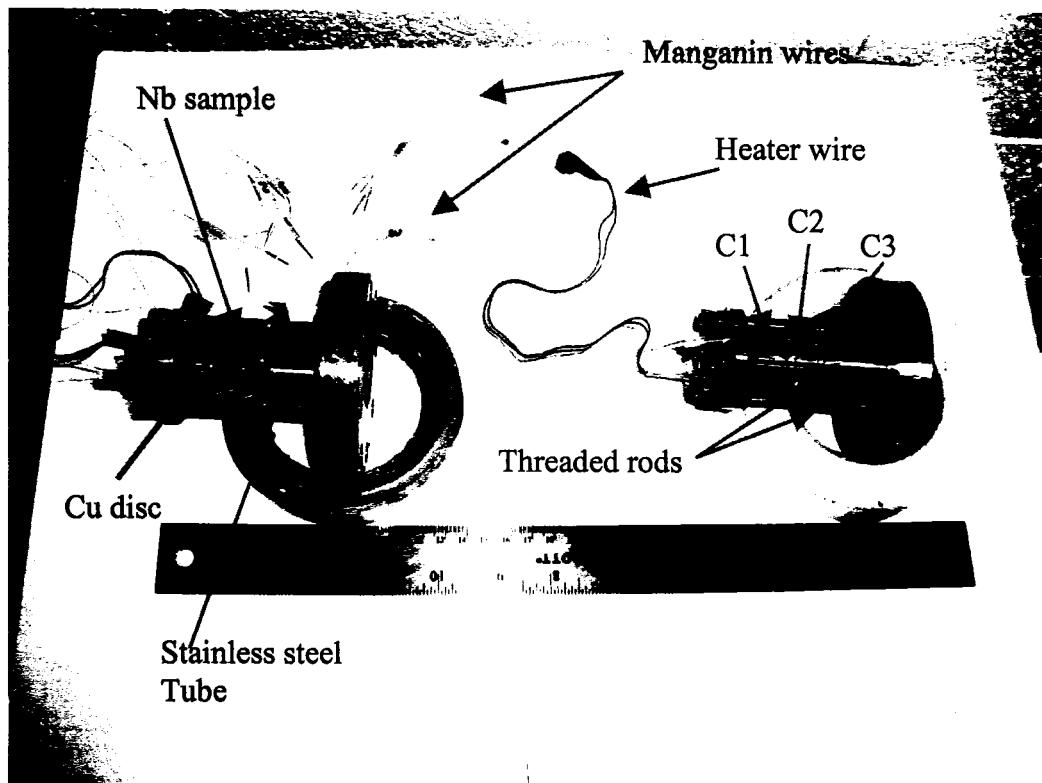
Figure 4.10: Assembled Nb samples in a sample holder assembly. Three carbon sensors with manganin wires are also visible. Sensor C1 is closer to the heater end of the Nb sample and sensor C3 is closer to the He interface.

The electrical resistance, R, of the carbon sensors is measured with the help of LakeShore® instrument, employing a four lead method, and is recorded through custom made LabView® data acquisition software. This also helped in avoiding carbon sensor's self-heating problem where the instrument employs constant current source of 10 μA for resistance measurements. However, for temperatures below 1.9 K, the resistance of a typical carbon sensor becomes more than 7500 Ω, an upper limit for the Lakeshore instrument® to measure. To resolve such a situation, a resistor with about 10 kΩ resistance is attached in parallel with the temperature measuring carbon sensor, thus limiting the current going into the sensor and reducing the overall resistance of the measurement. With this technique, temperature measurements down to 1.6 K are made without any significant loss of sensitivity.

4.10 Calibration of Carbon Sensors

Calibration of the carbon sensors is carried out before every test. Thus, when no power is applied to the heater, the He pressure is varied at various settings and the resistance values of carbon sensors are compared against the temperature of Ge sensor in vacuum. By adjusting the gas return valve so as to raise the internal pressure of the Dewar, raising the temperature of the bath to obtain calibration points above 4.2 K. For safety reasons the maximum temperature reading needed for a useful calibration data remain below ~ 4.5 K, corresponding to a pressure of ~ 980 torr. Two or three temperature data points in between them are sufficient for reliable calibration. Sufficient settling time is allowed at each calibration temperature data point for steady state to be achieved for all sensor readings. A similar procedure is applied for calibration between 4.2 K to 2.0 K where about 10 intermediate calibration data points are sufficient to obtain

a reasonable calibration fit having a typical standard deviation of better than 0.1 mK at T_b of 2.0 K.

4.11 Flat Plate Sample

The sample holders shown in figure 4.10 are for measuring both the thermal conductivity as well as the heat transfer coefficient in the same experiment. However, to measure only the thermal conductivity of the Nb sample, a much simpler sample holder is used.

To measure only the thermal conductivity of an actual Nb sheet that is used for the fabrication of SRF cavities, rectangular flat plate Nb samples are used as shown in Figure 4.11. The sample holder assembly for these samples is simply a blank Conflat flange with a blind tap drilled hole in the middle for the attachment of the sample plate. The thin foil heater is pasted on the free end of the plate with three collinear carbon sensors (~ 1 cm apart) are pasted on the middle section as shown in Figure 4.12. A calibrated Ge sensor is pasted on the bottom side of the plate at the same axial position as the middle sensor. The cold sink end of plate is attached with the Conflat flange with the help of a brass screw. Apizon® N grease (a high thermal conductive cryogenic grease) is applied between the mating surfaces to reduce contact resistance between the sample plate and the Conflat flange.
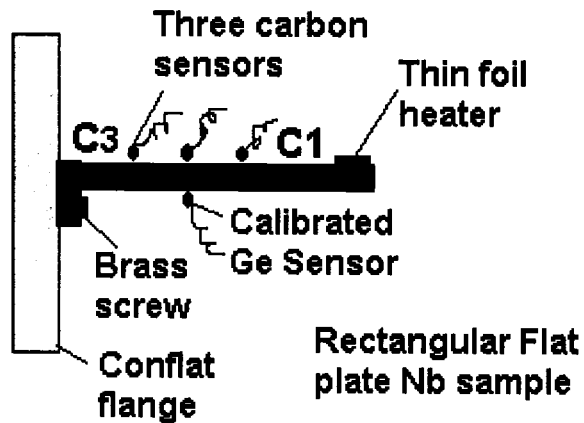
Figure 4.11: Rectangular flat plate Nb sample (11 X 1.4 X 0.3 cm) attached to a 2 ¾" Conflat flange with the help of a brass screw. Three collinear carbon sensors are placed to measure the thermal conductivity of the sample. (Drawing not to scale)
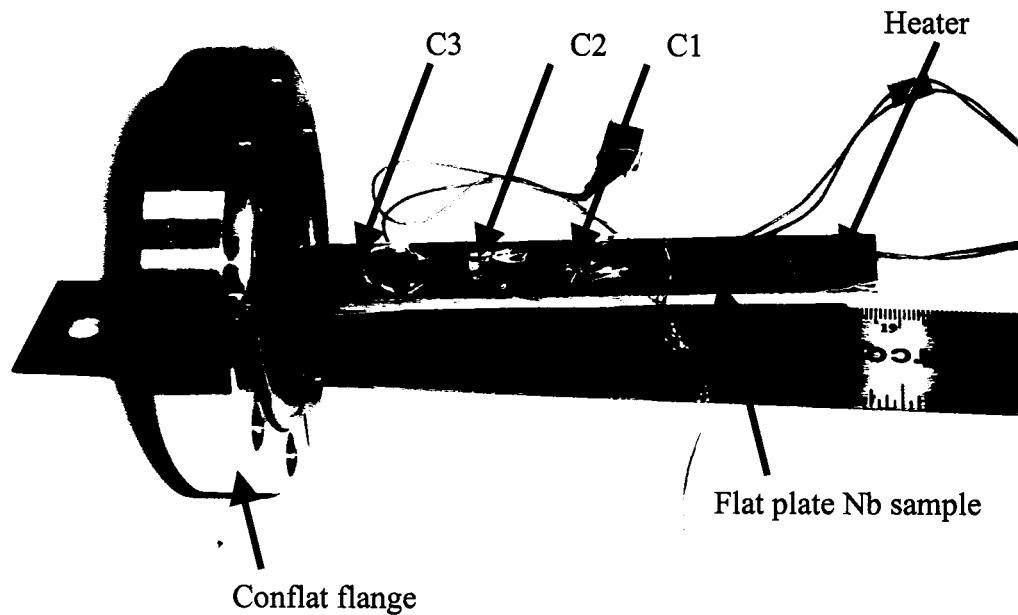
Figure 4.12: Flat plate Nb sample is attached to a Conflat flange. Three collinear carbon sensors (C1, C2 and C3) are placed to measure the thermal conductivity of the sample. A thin foil heater on the free end of the sample is also shown.

4.12 Cold Shock and Leak Test

In order to verify the sealing of the vacuum system, especially through the improvised sealing of the Nb sample with the sharp knife-edge stainless steel tube, the assembly must be tested against cold shock and leaks. Since most of the thermal contraction and expansion takes place above 100 K, liquid nitrogen provides a reliable cold shock test, as shown in figure 4.13. During the cold shock test, the leak detector with a gas sensitive filament detects any evidence of seal leaks.

Figure 4.13. Lid assembly is on a test stand and hooked up with a leak detector. The housing assembly is immersed in a pool of liquid nitrogen for cold shock.

4.13 Steady State Measurement Technique

Traditionally, the experimental technique to measure Kapitza conductance is through steady state measurements. The experimental arrangement, as described above, has the advantage of measuring both the thermal conductivity as well as the Nb-He interface heat transfer coefficient at the same time. The sample holder assembly in figure 4.5(b) has a resemblance to the one used by Mittag [35] except some improvement in the design to reduce the parallel heat losses. The helium bath temperature T_b in the helium-sample chamber is stabilized to within 14 Pa by using the Dewar pressure control valve. T_b is measured with the help of the factory calibrated germanium sensor installed inside the tube. The temperature distribution along the sample is measured with the three carbon-resistance thermometers, C1 to C3 with C1 being closer to the heater end as shown in figure 4.10 and 4.12. Another calibrated germanium sensor is placed next to C2 on the sample in vacuum to provide accurate in situ calibration of the carbon sensors. The distance between C3 and the interface surface is 5 mm.

Measurements of both k and h at a given bath temperature, typically consists of recording all three temperatures and the corresponding heater power. The residual calibration errors are minimized by the method discussed in section 4.1.3 and the sample interface temperature is estimated by linear extrapolation as also employed by Mittag [35]. Heat leaks into liquid helium through the six rods via the base plate and the G-10 disc from the heater as well as heat leaks from the heater current wires, as shown in appendix C, are estimated to be less than 1%. Heat leaks along the sensor leads were estimated to be negligible. Also, heat leaks through the stainless steel tube sealing the vacuum from the liquid He, as shown in appendix D, are estimated to be negligible (approx 0.110 % at

2 K). The, reduction in the area of the sample surface exposed to liquid helium is also accounted for in the data deduction.

5 Results and Analysis

Test results from two types of samples, i.e. cylinders and flat rectangular plates, are presented here. The cylindrical samples, S1 and S2, were taken from a long Nb rod of small grain supplied by Tokyo Denkai with an ingot RRR of 232. Measurements of both, the thermal conductivity and the Kapitza conductance are reported for these two cylindrical samples. Wah Chang supplied the two rectangular flat plate samples, F1 and F2, for thermal conductivity measurements to evaluate the possibility of partial crystallization in the "as received" Nb. The supplier for these samples reported a RRR value of 300. (Specification sheets from each lot of the samples are given in appendix F).

5.1 Cylindrical Sample Preparation

A series of tests were conducted on the two Nb cylindrical samples, to evaluate the effect of various surface and bulk conditions. Table 5.1 lists the treatments of each test performed on these samples in chronological order. Sample conditions that may have an effect on the bulk material properties, such as plastic deformations and heat treatment or annealing, their thermal conductivity results, are analyzed. Also, those conditions that affect the Nb surface interface with He, such as BCP etching, mechanical polishing, surface roughness, and annealing, are also analyzed. Here, the word "BCP" stands for Buffer Chemical Polish, a chemical etching procedure routinely employed on SRF cavities to remove surface contaminations and improve surface texture. A standard BCP solution comprised of three chemicals i.e. HF, H_3PO_4, and HNO_3 in a mixture ratio of 1:1:2 [13]. Figure 5.1 shows the general surface conditions of sample S1 and S2. The rough surface of sample S2 can be qualitatively compared with that of relatively smoother surface of sample S1. As discussed earlier, titanification is a gettering process

71

usually employed on the SRF cavities to improve the purity of the Nb. This should result in increased RRR value of the Nb by removing the interstitial impurities. Since the process takes place at moderate temperatures of ~1300 °C to 1400 °C, the grain size of the Nb also increases significantly. Subsequently, the outer contaminated surface, ~45 to 50 μm, is removed through regular BCP etching.

Table 5.1: Surface and bulk preparation of the two cylindrical niobium samples

Date	Sample	Surface	Process
Nov 2005	S1	Flat & clean surface	Machine cut & light BCP etch (10-20 μm)
Nov 2005	S2	Flat surface	Machine cut
May 2006	S1	Flat smooth	Mechanical. polish to a mirrored surface & light BCP etch (5-6 μm)
May 2006	S2	Rough on the order of 1-2 mm	Cut surface with stainless steel knife-edge through mechanical hand press deep enough for SI > 3. Light BCP etch (5-6 μm)
June 2006	S1	Flat smooth	~ 3% of total length plastically deformed axially & mechanical polish to mirrored surface and light BCP etch (10-15 μm)
June 2006	S2	Rough on the order of 1-2 mm	BCP etch cleaning & heat treatment at 750 °C for 2 hrs
Oct 2006	S1	Flat smooth	Mirror polished & titanification at 1300 °C for 2 hrs and 1200 °C for 4 hrs & BCP etch (~50 μm)
Oct 2006	S2	Rough on the order of 1-2 mm	Titanification at 1300 °C for 2 hrs and 1200 °C for 4 hrs & BCP etch (~50 μm)
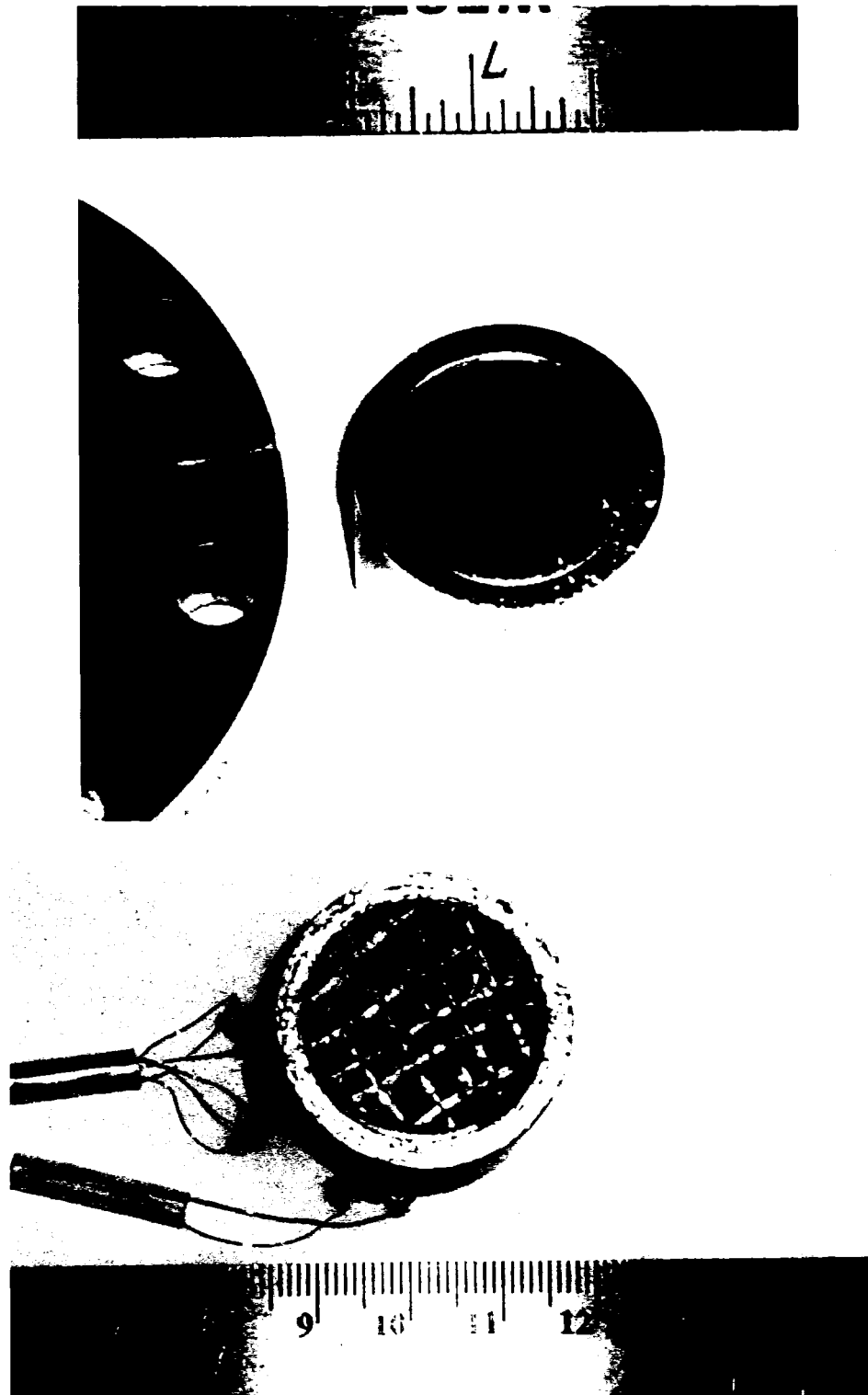
Figure 5.1: Two cylindrical samples S1 (upper view) and S2 (lower view) are shown. S2 sample has a rough surface (~ 1-2 mm) as compared with smooth surface of sample S1.

5.2 Flat plate Nb Sample Preparation

Each of the flat plate samples is identical to the other and has undergone the same heat treatment (750 °C for 2 hours) process as that for cylindrical sample S2, prior to its June 2006 test. Table 5.2 lists the preparation details of these samples prior to each test.

Table 5.2: Bulk preparation of two flat plate niobium samples

Date	Sample	Surface	Process
March 2006	F1	Flat smooth	Ordinary cleaning
March 2006	F2	Flat smooth	Ordinary cleaning
July 2006	F1	Flat smooth	BCP etch cleaning & heat treatment at 750 °C for 2 hrs
July 2006	F2	Flat smooth	BCP etch cleaning & heat treatment at 750 °C for 2 hrs

5.3 Thermal Conductivity Measurements

5.3.1 Repeatability Analysis

(a) Comparison at Different Bath Temperatures

Thermal conductivity measurements of Nb sample S1 tested in November 2005, is shown in figure 5.2 for 3 different bath temperatures i.e. at 1.6 K, 2.0 K and 2.1 K. Here, values of thermal conductivity for the sample are given for each of the two pair of sensors measuring temperature rise (i.e. pair 1 corresponds to sensor 1 and 2 and pair 2 corresponds to sensor 2 and 3) and are plotted as a function of average temperature of each pair of sensors. In this nomenclature, sensor 1 is closest to the heater. Though the error bars have been placed only on the result at 2.0 K to avoid clutter, the figure shows reasonable repeatability through overlap of measurement values at three different bath temperatures. Below ~ 3 K, the hump in thermal conductivity is due to phonon conduction where the maxima occurring at ~ 2 K is known as 'Phonon peak' and is discussed earlier in chapter 2.
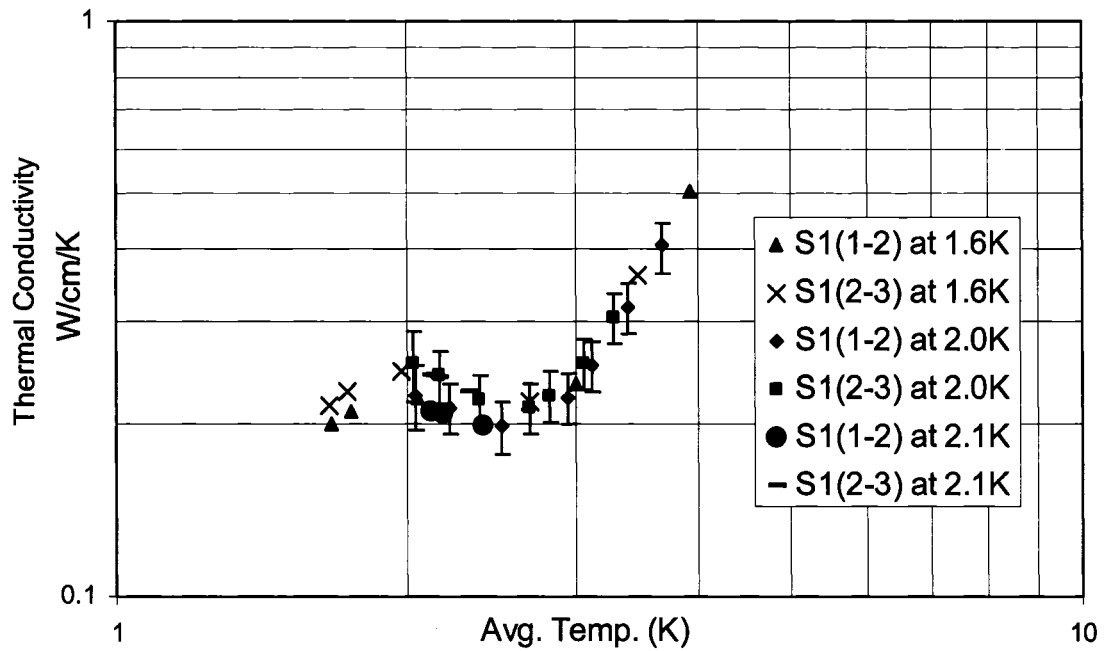
Figure 5.2: Thermal conductivity of sample S1 at three different bath temperatures, as shown in the legend, measured in Nov 2005. Error bars are on the graph with bath temperature of 2.0 K.

(b) Comparison of Both Samples

Thermal conductivity measurements of both the Nb samples, S1 and S2, tested in November 2005, are shown in figure 5.3 to demonstrate the repeatability of the measurements. Again, the error bars have been suppressed to avoid clutter and for clarity of the comparison. Clear formation of a phonon peak at around ~2 K in both of the cylindrical samples is evident. As expected, there is no significant difference in the thermal conductivity measurements of the two samples as both are from the same bulk material. This comparison in figure 5.3 provides reasonable confidence in repeatability of the experimental setup where two identical but independent samples provide identical results. There is slightly more dispersion in the data of the two samples below ~ 3 K, in the phonon conduction regime where microstructure of the bulk Nb plays a dominant role in determining its thermal conductivity. A closer look on the figure 5.3 reveals that this dispersion in the data is more pronounced within the two pair of sensors i.e. (1-2) and (2-3) on the same sample, than within the two samples. Since no measurements for the microstructure of the samples have been done, therefore, no certain explanation can be provided. However one possible source for the variation in the microstructure within the sample could be due to the stresses induced within the vicinity of stainless steel tube sealing against the Nb surface. This effect has also observed by Mittag [35] in this kind of experimental apparatus.
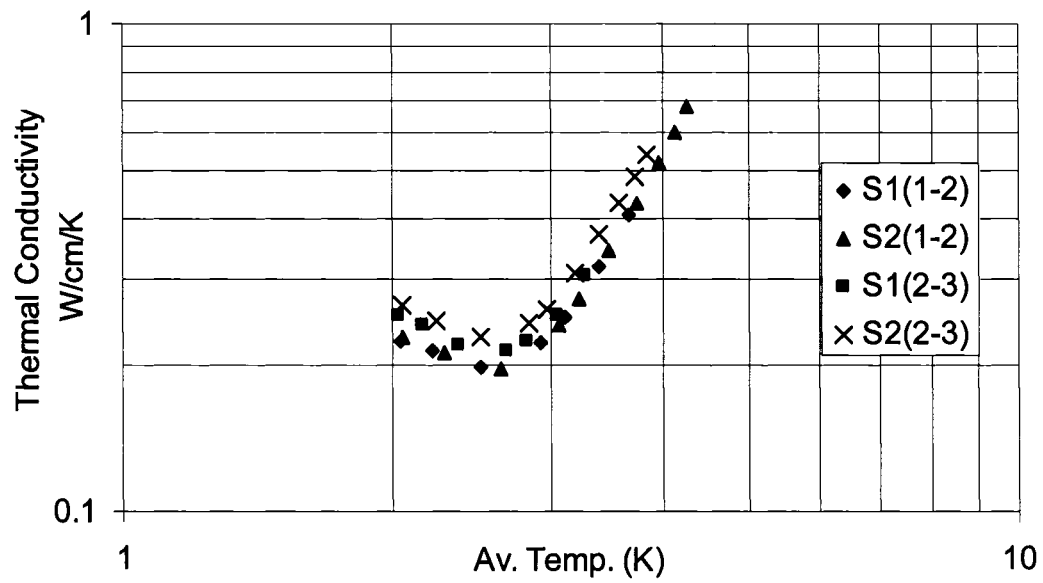
Figure 5.3: The phonon peak is shown near average temperature of 2 K in thermal conductivity measurements of the two samples, S1 and S2, in November 2005 tests. $(T_b=2$ K).

5.3.2 Validation Comparison with Literature Data

The comparison of the results with data from the literature [9] for thermal conductivity of Nb with different RRR values is given in figure 5.4. Here, the results of the sample S2 is shown in the figure for a test carried out prior to November 2005 [40]. Close agreement with data from the literature [12] suggests validity of the experimental design and execution.
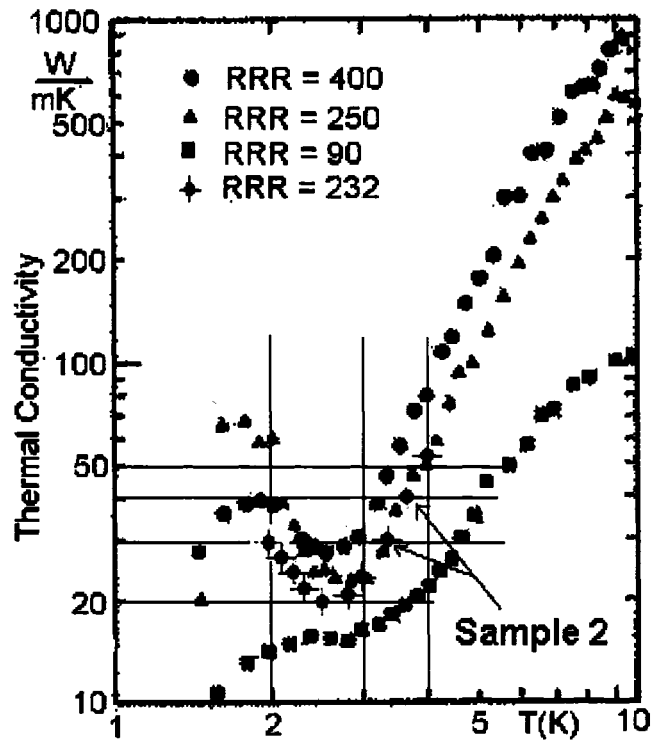
Figure 5.4: Variation of thermal conductivity with temperature for sample S2 is shown along with data [40]. (Literature data adapted from Padamsee [12]).

5.3.3 A New Trend in the Data

(a) Effect of Plastic Deformations

Measurements of the thermal conductivity performed in May and June 2006 are compared in figure 5.5 for sample S1. As noted from table 1, prior to the June test, sample S1 was intentionally compressed axially to induce a nominal axial strain ($\Delta L/L$) of ~3% in the sample because of plastic deformation. The absence of a phonon peak and a nearly 80% reduction in thermal conductivity at 2 K in the June measurements on S1, in contrast with the values from its May 2006 test, are considered to be the effect of plastic deformation on the thermal conductivity of Nb. As expected, this effect is insignificant at temperature above ~ 3 K, where the electronic contribution to thermal conductivity of Nb starts to dominate and no significant difference in the results from the two tests is evident.

May: Unstrained sample
June: 3% axial strain
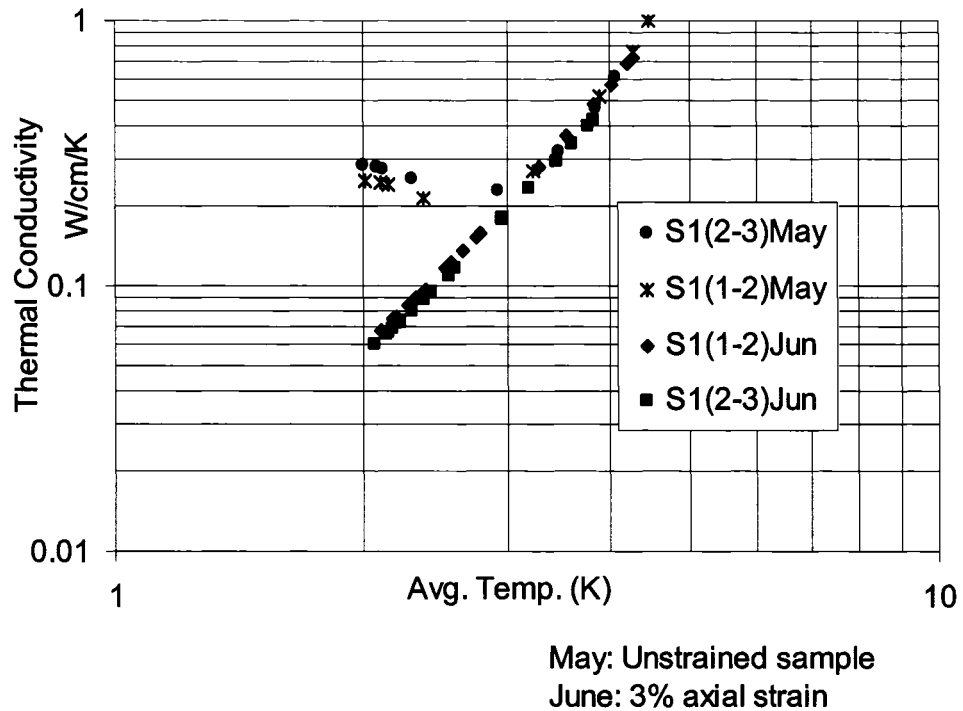
Figure 5.5: Phonon peak is clearly absent in the thermal conductivity measurements of sample S1 in the tests carried out after 3% strains induced in the sample (June 2006 test) as compared with its tests performed in May 2006

80

b) Effect of Low Temperature Heat Treatment

For sample S2, the absence of a phonon peak in the measurements of May 2006, in contrast with those of November 2005, can be understood as surface roughness preparation protocol, as described in table 5.1 and shown in figure 5.1, with the stainless steel blade pressing against the surface, causing inadvertent strains in the bulk Nb, similar to those induced intentionally in S1.

Low temperature annealing (750 °C for 2 hrs) on S2, intended to recover the phonon peak in the Nb and shown in figure 5.6, is insufficient, although S2 demonstrates a small increase (~30%) in thermal conductivity over the temperature range measured.

May: Axially strained sample
June: Heat treated
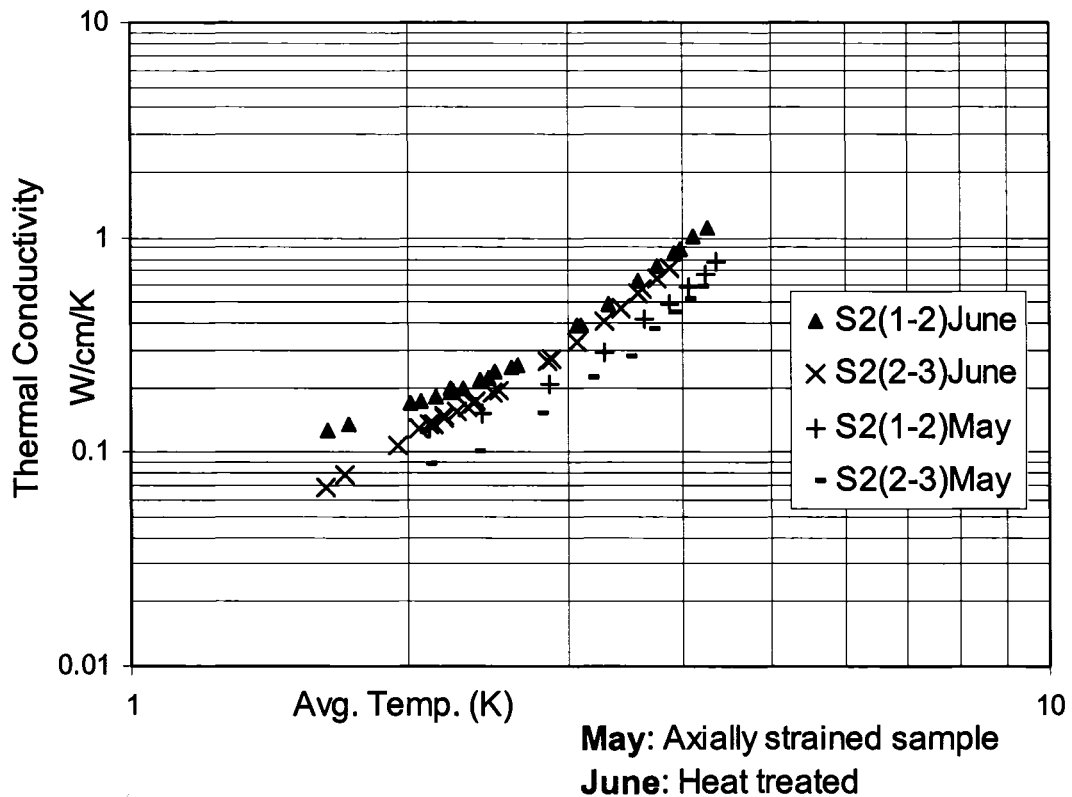
Figure 5.6. The phonon peak did not reappear after it was lost during the compression process in preparation of (May test) sample S2. Low temperature heat treatment (June test) has small effect on the thermal conductivity of the niobium.

This is possibly due to knocking off some of the hydrogen impurities at the annealing temperatures causing a slight increase in the RRR value of the sample. The same effect of low temperature annealing is also observed in thermal conductivity measurements done on the two flat plate samples. The initial measurements on flat samples done in March 2006 did not reveal a phonon peak in the as received material, possibly due to partial re-crystallization in the material. After annealing them at 750 °C for 2 hours, no significant change in their thermal conductivities was observed for most of the temperature range measured. However, a slight improvement below ~ 3 K can still be observed due to the low temperature heat treatment. The result for F1 is presented in figure 5.7(a) and those of F2 is in figure 5.7(b). Close agreement of these results increases the confidence in the experimental results.

Based on these observations, it can be argued that low temperature annealing is insufficient to recover the lost phonon peak in the thermal conductivity curve of Nb with RRR ranging from 200 to 300.
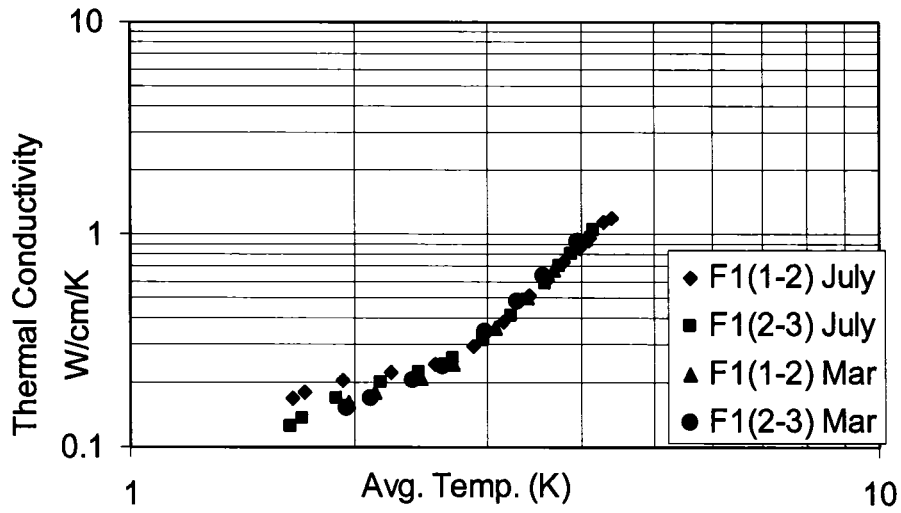
(a)
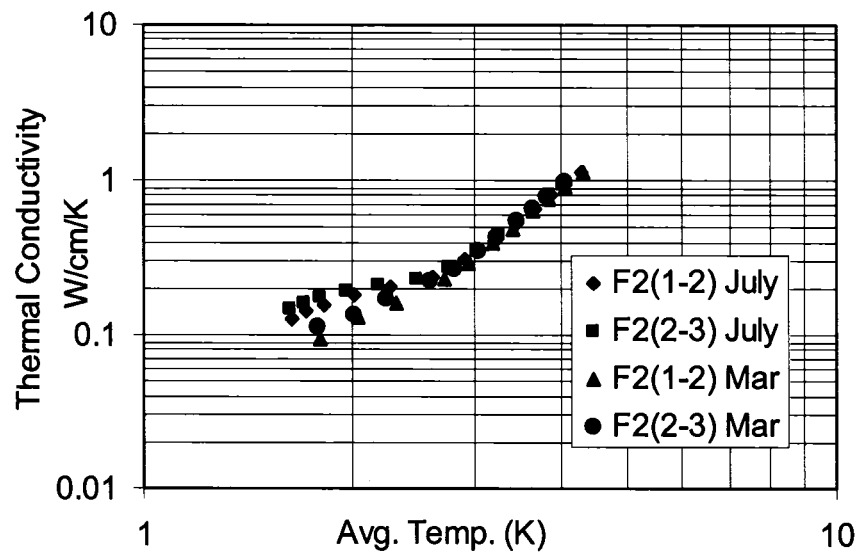
(b)

Figure 5.7 (a) and (b): The low temperature heat treatment (July 2006) has slightly increased the thermal conductivity of flat samples in phonon conduction regime, from their previous test in March 2006 on the as received samples.

(c) Effect of Titanification

As mentioned earlier, during the titanification process the temperature of the sample is raised to ~1300 °C in high vacuum conditions. At these moderate temperatures, sufficient annealing within the Nb takes place to relieve internal strains in the material. Also, the grain size of Nb grows from the order of μm to mm. As shown in figure 5.8 for sample S1 and figure 5.9 for sample S2, this process resulted in the recovery of phonon peaks in the thermal conductivity for the two Nb samples that were lost due to induced strains. There is slightly more recovery of phonon peak for sample S2 after titanification than it was in the as received sample. This could be due to the fact that the sample S2 had already under gone low temperature annealing with slight increase in its thermal conductivity below 3 K, as mentioned in section (b) above. Possibly, this second annealing at moderate temperatures augmented the reformation of phonon peak slightly more than it was in the as received sample.

Unexpectedly, a slight decrease in the thermal conductivity above ~3 K is also noticeable in both the samples, ~20 % in sample 1 and ~8 % in sample 2 at 4.2 K, as compared to their values before annealing. This is understandable since the purification process through titanification relies on the diffusion of oxygen in the bulk to the surface of niobium where they are captured by titanium. The diffusion rate of oxygen at these temperatures is ~ 1 mm per hour [45], and the titanification process is optimized to treat 2 to 3 mm thick Nb cavities. However, the cylindrical samples have 30mm diameter. It seems quite reasonable that much longer time than the 6 hours, namely (15 mm / 1. mm/hr) 15 hrs [46], for the cylindrical samples were needed for complete purification.
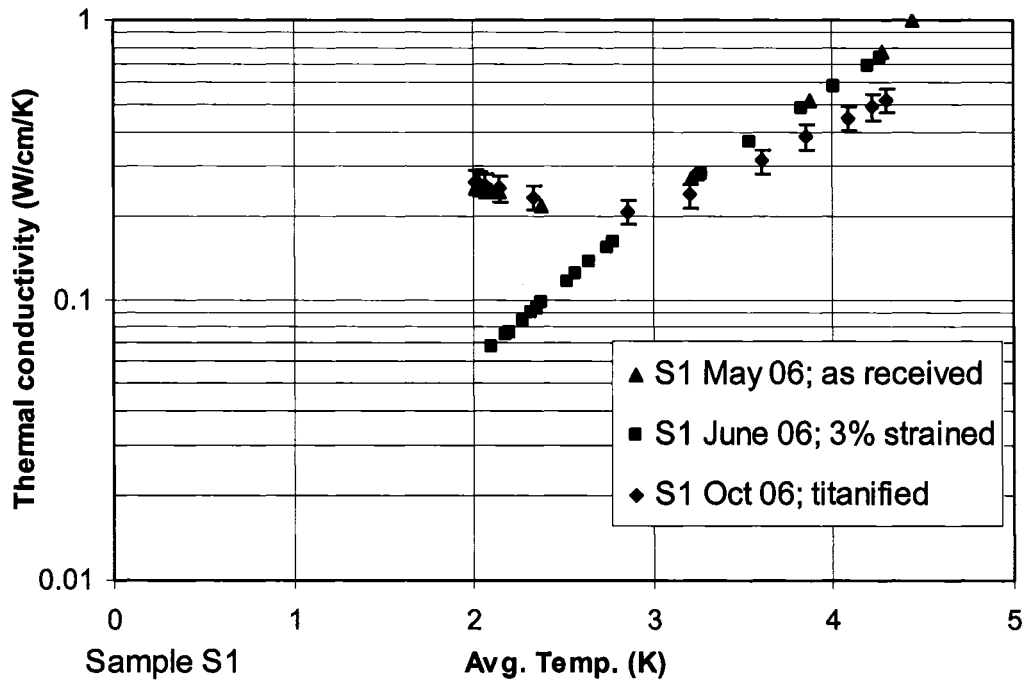
Figure 5.8: Moderate temperature annealing during titanification process resulted in the reformation of the phonon peak (Oct 06) after it was lost due to induced strains (June 06) in the as received Nb sample S1 (May 06)
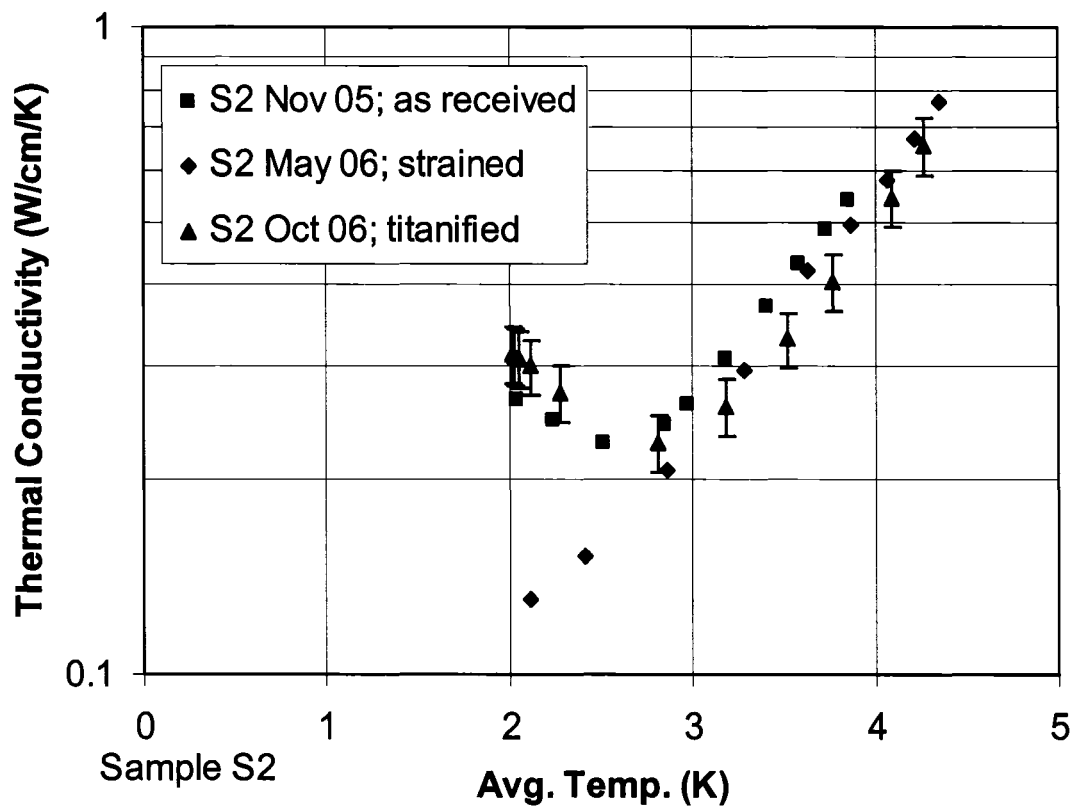
Figure 5.9: Moderate temperature annealing during titanification resulted in the reformation of phonon peak (Oct 06) after it was lost due to inadvertent strains induced (May 06) in the as received Nb sample S2 (Nov 05)

5.4 Nucleate Boiling Heat Transfer Measurements

As discussed in chapter 3, in the nucleate boiling regime, heat transfer is governed primarily through the nucleation sites on the heater surface. The rough surface provides nucleation sites of preferential locations for the bubbles to form more readily than on a smoother surface. As is generally understood, the surface roughness varies with the type of process performed on the surface. The effect of surface roughness due to different processes, as mentioned in table 5.1, on the nucleate boiling heat transfer has been studied both qualitatively and quantitatively on each of the two cylindrical samples, S1 and S2. For quantitative analysis, optical microscope has been used for the surface roughness measurements. However, when the surface roughness increased beyond the optical resolution of the microscope, results are qualitatively discussed. The qualitative analysis is based on either visual observations or wherever possible, a use of improvised depth gauge is made in order to estimate the surface character.

5.4.1 Surface Roughness Measurements

Figure 5.10 and 5.11 shows the surface roughness measurements on sample S1 and S2 respectively prior to their November 2005 test. Also, the data provides the value of surface index as well. From table 5.1 recall that both of the samples, S1 and S2, had a machine cut surface, however, the sample S1 went an additional step of a light BCP etch as is usually performed on the SRF cavities for surface texture improvements. Visually comparing the surfaces of sample S1 and S2, sample S2 obviously appeared rougher than the S1.

The surface roughness parameters for the two samples obtained from the optical microscope can be compared with each other. By comparing their average roughness

parameter, Ra, for instance, at a first glance it appears that S1 with Ra = 9.87 µm is at least two times rougher than S2 with Ra = 4.57 µm. This is a misleading result, although both of the measurements have been made with the same magnification and on the same length scales with the same sampling size. The reason for such an unexpected result is basically the limited optical resolution of the microscope for the rougher sample. The amount of valid data, as shown in the figures 5.11, obtained by the microscope for a visually rough sample S2 is 31.2% only as compared with relatively smoother surface of sample S1 having 88.4% of valid data and shown in figure 5.10. Thus, the statistical parameters so computed for sample S2 are not the true representative of the actual surface and thus are unreliable and can't be compared with the more reliable data of sample S1. It is in such situations that nucleate boiling results are discussed in qualitative terms. More detailed information about surface roughness parameters is given in appendix G.

Estimates of surface index on the Sample S2 after it has been made further rough prior to its May 2006 test were made through an improvised depth gauge. In this, the thick depth rod of the gauge was replaced by a custom made thin pin having tip diameter not more than 0.65 mm. Since the surface of sample S2, as shown in figure 5.1, looks like a 2-D horizontal grid made of grooves / valleys while the mountain or the peaks appearing on the intersections of these valleys in the vertical dimension. Thus by estimating the width and the length of the grooves along with the height of each of the mountain like structure on the surface and a known diameter of the surface, provided a reasonable value of surface index (SI) > 3 for the sample S2.
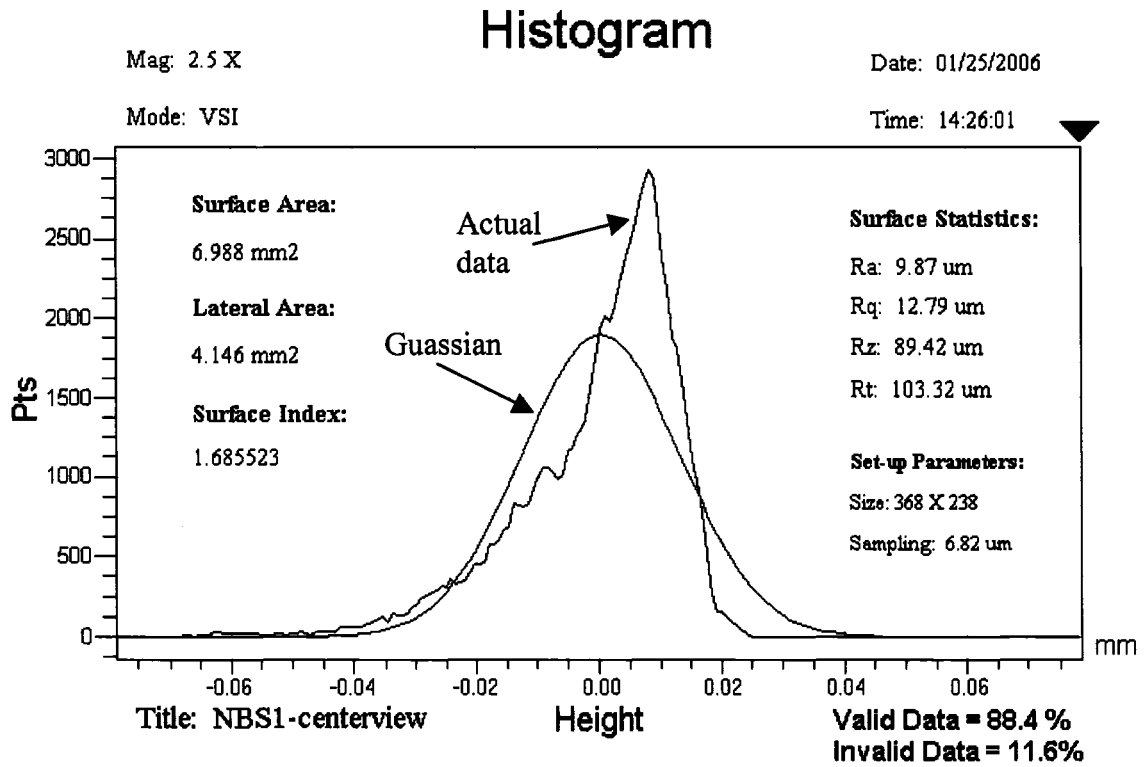
Figure 5.10: Histogram as well as different surface roughness parameters is shown for sample S1.

Histogram

Mag: 2.5 X

Mode: VSI

Date: 01/25/2006

Time: 14:16:20

Surface Area:

2.412 mm2

Lateral Area:

1.471 mm2

Surface Index:

1.639924

Actual data

Guassian

Surface Statistics:

Ra: 4.57 um

Rq: 6.25 um

Rz: 46.10 um

Rt: 54.85 um

Set-up Parameters:

Size: 368 X 238

Sampling: 6.82 um

Title: NbS2-Center View

Height

Valid Data = 31.2 %
Invalid Data = 68.8%
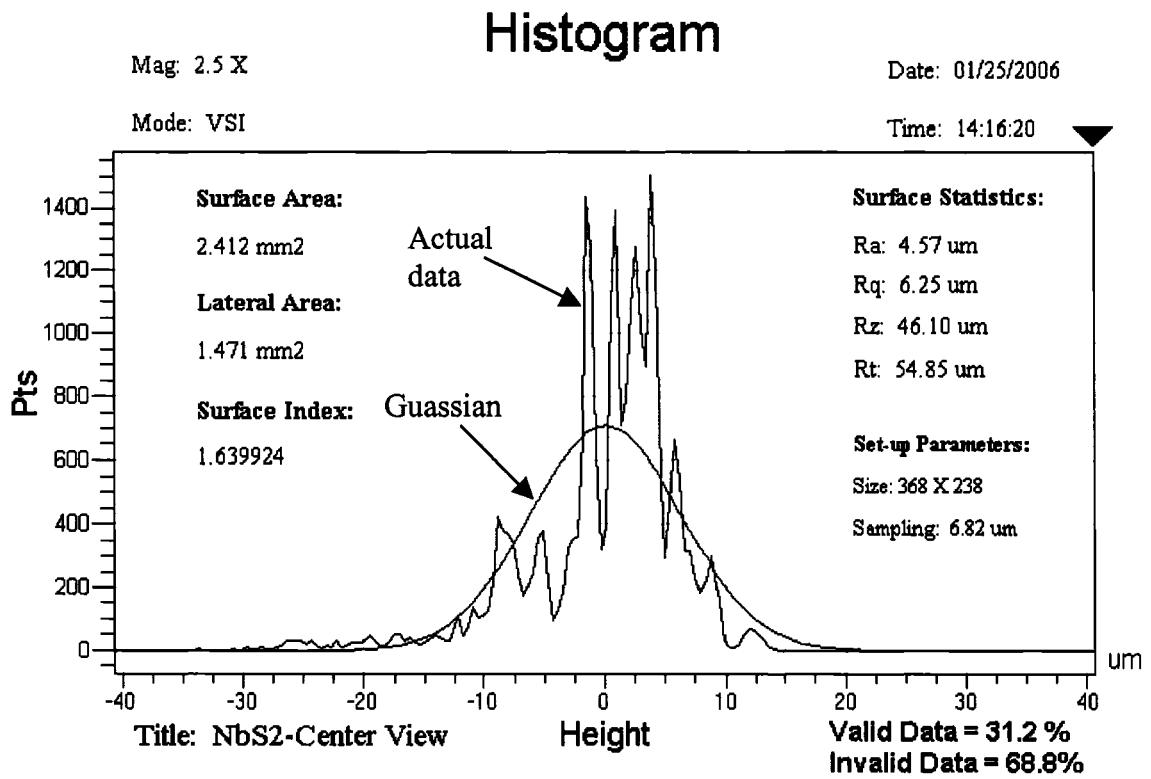
Figure 5.11: Histogram as well as different surface roughness parameters is shown for sample S2. Note that the valid data is only 31.2 % in this measurement.

90

5.4.2 Comparison of Machine Cut and BCP etched Surfaces

The effect of surface roughness on nucleate boiling heat transfer in liquid helium is well known and has been discussed in chapter 3. Also recall that the empirical correlation provided by Schmidt [17] and shown in figure 3.3 is conservative with most experimental data demonstrating lesser superheat than the one predicted by the correlation. The same observation can be made in comparison of the test results for the two samples, S1 and S2, obtained in November 2005 and shown in figure 5.12. Here S1, with improved surface texture through BCP etching is visually smoother than S2. As expected, this resulted in more superheat than S2, but is still less than that predicted by the empirical correlation.
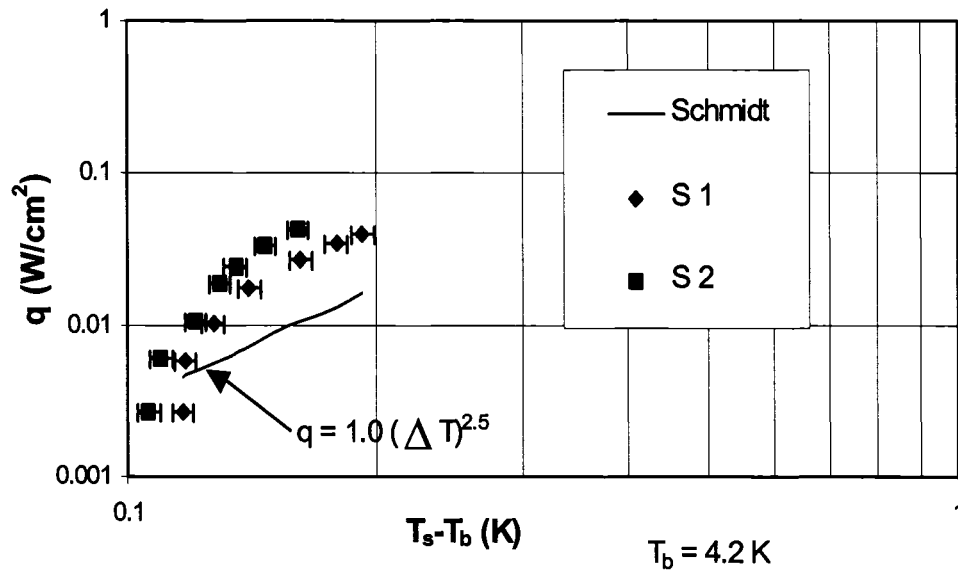
Figure 5.12: Nucleate boiling heat transfer measurements for the two cylindrical samples made in November 2005 tests at bath temperature of 4.2 K. Schmidt correlation is the same as the one in figure 3.3.

5.4.3 Effect of Mechanical Polishing

The effect of mechanical polishing on the sample S1 is shown in figure 5.13 by comparing its nucleate boiling results in three different tests. Both the May and the June 06 tests are of mechanically polished surface of sample S1. This resulted in increased superheat for the same amount of heat flux for the sample S1 as compared with its relatively rough surface in Nov 05 test. As expected, this increase in the superheat is due to the effect of mechanical polishing on the nucleate boiling characteristics of liquid helium for smoother surfaces. The results of mechanically polished surface (May and June 2006) are closer to the conservative correlation provided by Schmidt [17]. Also note the variation of the result within the mechanically polished surfaces. This is attributed to slight differences in the surface preparations for the two tests. Differences in etch rates / duration during the BCP etching or variations within the mechanical polishing procedure may cause such variations in the nucleate boiling heat transfer.
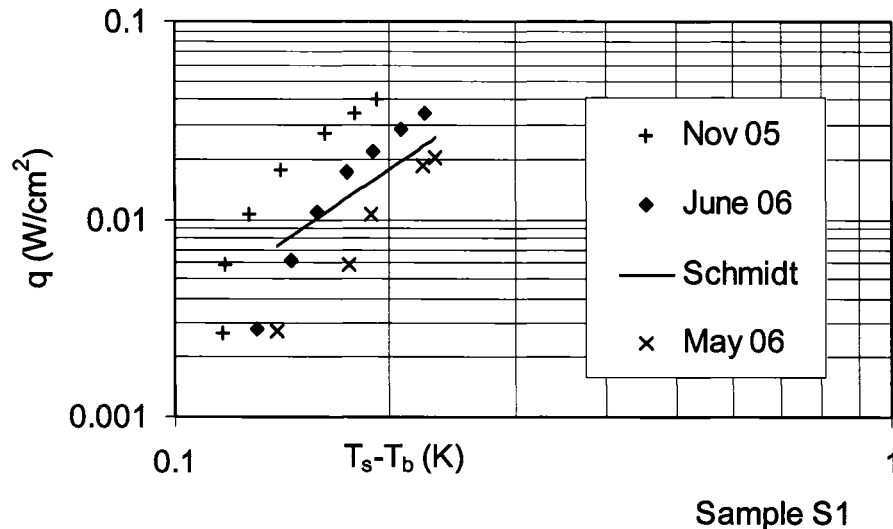
Figure 5.13: Effect of mechanical polishing on sample S1 has resulted in an increase of superheat for the same applied heat flux.

5.4.4 Effect of Surface Index (SI)

From table 5.1 and the figure 5.1, it is noted that surface preparations on S2 for May 06 test resulted in SI > 3. Considerable decrease in superheat for the same heat flux resulted for its June 06 measurements, shown in figure 5.14, as compared with its November 05 result. This decrease is more prominent at low heat fluxes, where few bubbles are formed and natural convection effects still play a significant role in transferring the energy, as compared with those at relatively higher heat fluxes where increased numbers of bubbles are formed on the surface thus increasingly removing the energy from the surface. The same trend is seen, though less pronounced, in the June 06 test before which the S2 was BCP etched and heat-treated. At this time there is no quantitative explanation for the increase in superheat in sample S2 measured in the June 06 test as compared with the May 06 tests. The BCP etch done prior to the heat treatment, due to the change in surface texture, could be one possible explanation for this observation.
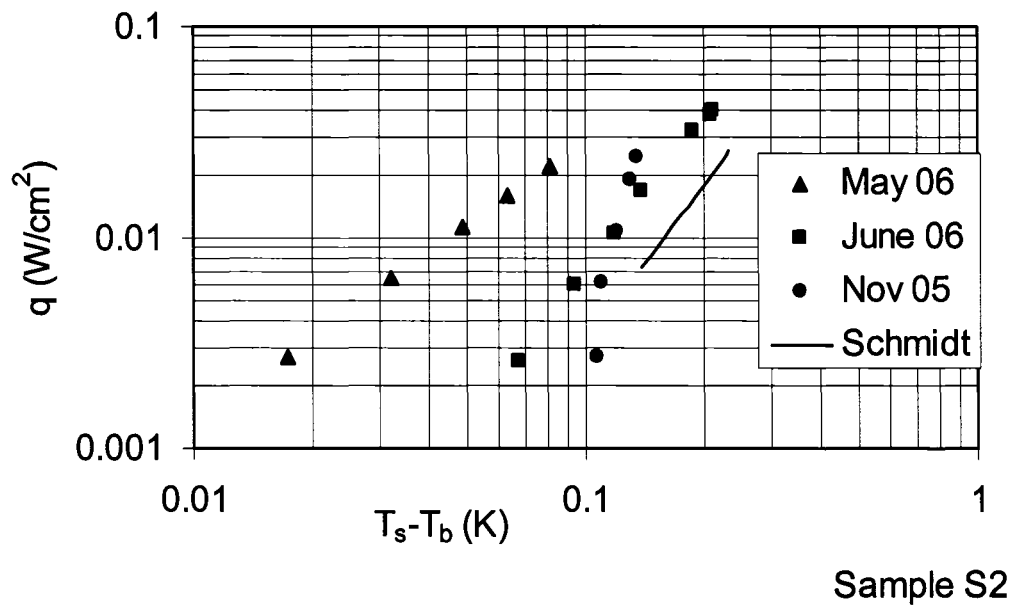
Figure 5.14: Decrease in superheat due to increase in SI of sample S2 is seen in May 06 measurements as compared with Nov 05.

5.4.5   Overall Effect of Surface Roughness

The overall effect of surface roughness on the interface heat transfer can be realized

qualitatively from the figure 5.15 where the results from all of the measurements made

during this study for both samples S1 and S2 have been presented on a common scale.

These data tend to confirm the trend already discussed in chapter 3 where an increase in

surface roughness decreases the surface superheat for a given heat flux or allows more

heat flux for a given temperature rise on the surface.
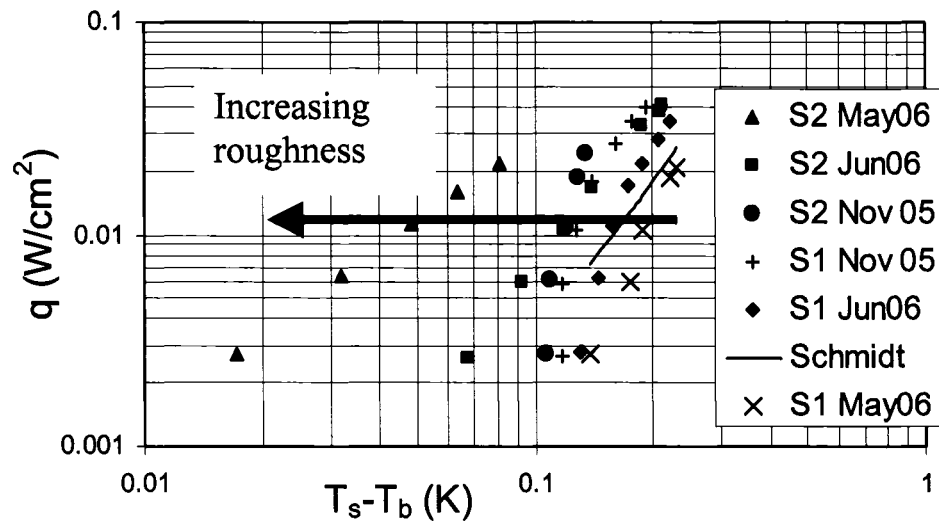
Figure 5.15: The effect of increasing surface roughness is to reduce the superheat for a given heat flux.

5.5 Kapitza Conductance Measurements

Recall from chapter 3 that nano-meter length scale surface roughness plays an important role in increasing the Kapitza conductance. At a macroscopic level, larger scale roughness carry more number of smaller scale roughness superimposed onto them. Thus increased SI of the surface may lead to enhanced Kapitza conductance.

5.5.1   Comparison with Literature Data

The BCP etched sample S1, having a cleaner surface than S2, has Kapitza conductance at 2 K that is about two times as that of S2, as shown in figure 5.16, for the test carried out in November 2005. The Kapitza conductance measurements of S1 are in reasonable agreement with the values provided in the literature by Bousson et al. [38] for Nb having comparable RRRs and from the same supplier. This provides confidence in the validity of the current experimental results.
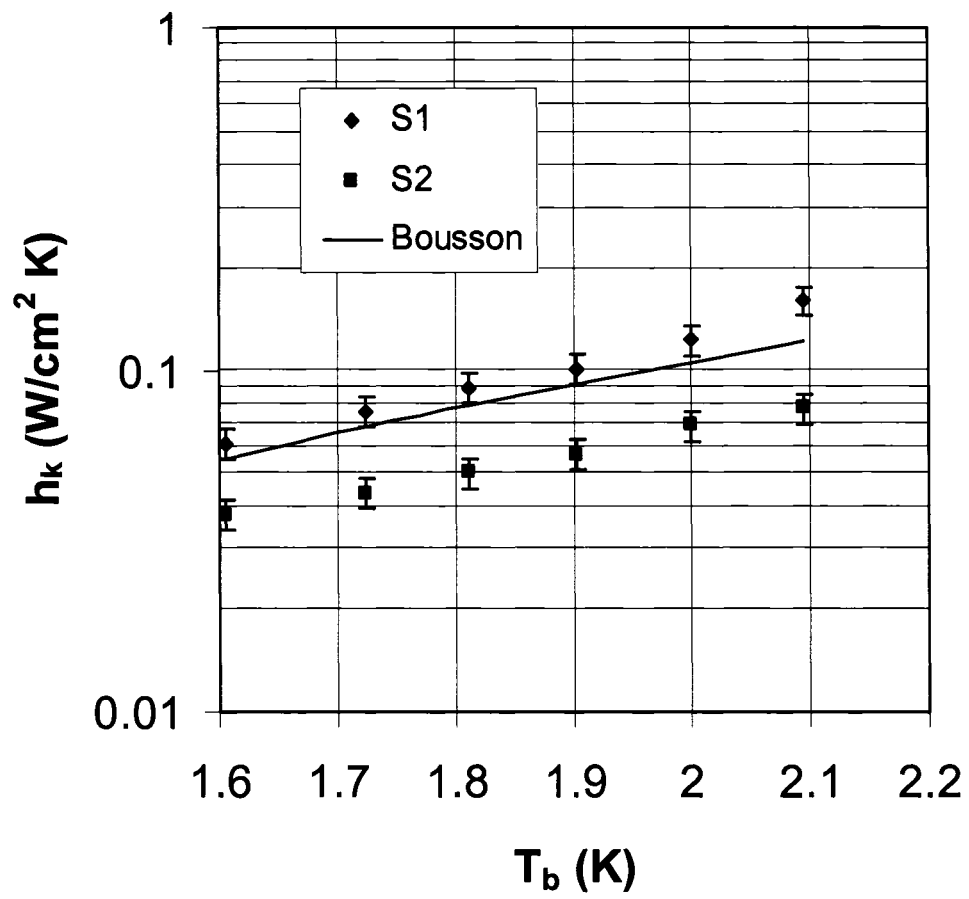
Figure 5.16: Kapitza conductance measurements for the two cylindrical samples, S1 and S2, carried out in November 2005, are compared with the one given by S. Bousson et al. [38].

5.5.2 Repeatability

The measurement of Kapitza conductance of the sample S1 before and after plastic deformation, as shown in figure 5.17, does not reveal any significant difference. This is likely due to the surface preparation for the two tests being identical on sample S1, i.e. mechanical polish and a light BCP etch.
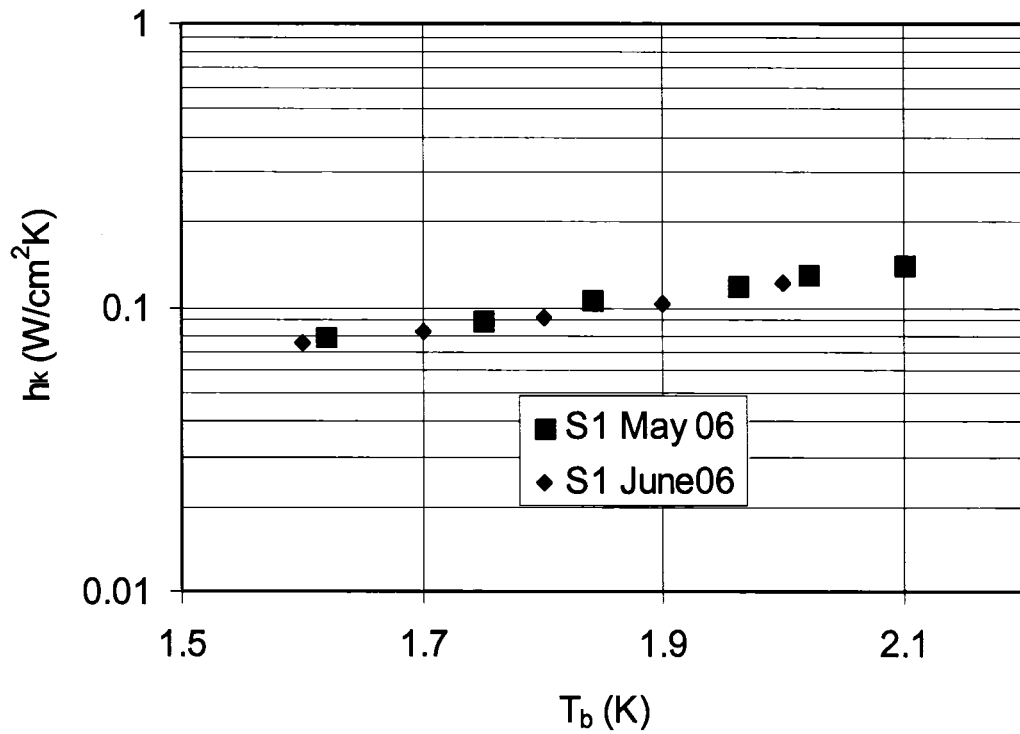
Figure 5.17: Kapitza conductance measurements of the sample S1 before and after the plastic deformations reveal no significant difference.

5.5.3 Effect of Surface Index

In order to evaluate the effect of large SI on Kapitza conductance, the surface roughness of sample S2 was increased such that its surface index became greater than 3. A sharp stainless steel edge surface was pressed against the Nb with the help of a hand press. Several deep (1-2 mm) cuts both in a horizontal as well as in vertical directions, like a 2-D grid on a flat surface and shown in figure 5.1, resulted in an overall SI > 3. Results of Kapitza measurements of sample S2 as shown in figure 5.18 can be compared for its May 06 test (SI >3) with those of its Nov 05 test (Machine cut surface). Although there is ~64% increase in h_k in May 06 measurements from its Nov 05 values and brought the values closer to the data by Bousson et al. [38], however, this is still below the values expected proportionately to SI > 3. This increase in hk can possibly be due to the BCP etching of the surface that took place prior to the May 06 testing and thus simply increased the values of sample S2 closer to the literature data and the data of sample S1 for its Nov 05 test that was shown in figure 5.17.

One possible explanation could be the effect of surface strains on the Kapitza conductance that might have been inadvertently induced on the surface during the roughness process described above. More discussion on the issue is made in subsequent sections and the next chapter.

5.5.4 Effect of Low Temperature Annealing

The same sample surface on S2, after annealing (June 06) at 750 °C for 2 hours, resulted in a nearly doubling in its Kapitza conductance values at 2 K, as shown in figure 5.18. This result may provide some help in understanding the effect of low temperature

annealing on the Kapitza conductance by relieving some of the induced surface strains during the process.
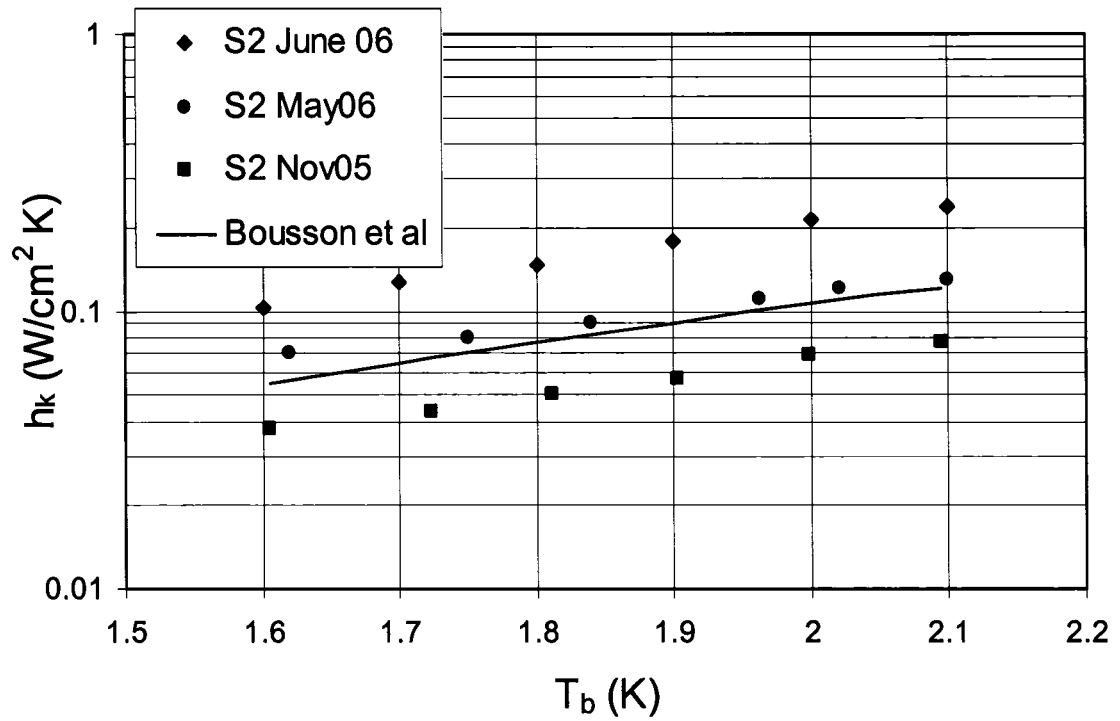
Figure 5.18: The Kapitza conductance of sample S2 surface with SI > 3 (May 06) and the effect of low temperature annealing with SI > 3 (June 06) is compared with the machine cut surface (Nov 05). Literature data is adapted from Bousson et al. [38].

5.5.5 Effect of Moderate Temperature Annealing

The moderate temperature annealing employed during the titanification process relieves the stresses not only inside the Nb but also on the surface as well. This surface effect on the Kapitza conductance is shown in figure 5.19 for sample S1 and in figure 5.20 for sample S2. The greater than two fold increase in Kapitza conductance at 2 K for sample 1 from its June test is possibly due to the moderate temperature annealing that occurred during the titanification process. For sample S2, the increase in Kapitza conductance is about ~30% as compared to its June test when its value was already increased through low temperature annealing as discussed in section 5.5.4 above.
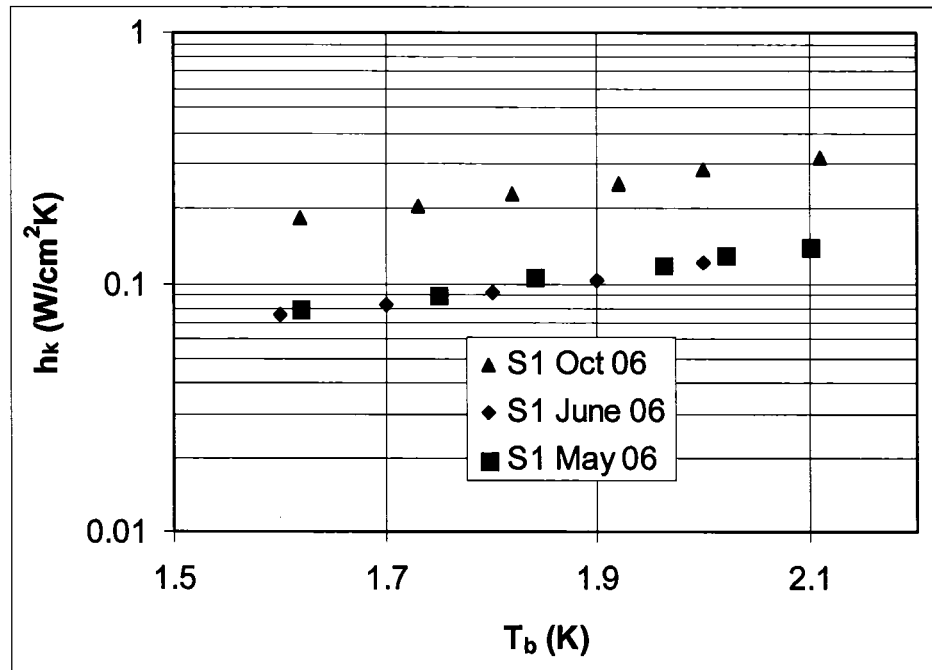
Figure 5.19: Kapitza conductance for sample S1 comparison before (May and June 06) and after titanification (Oct 06).
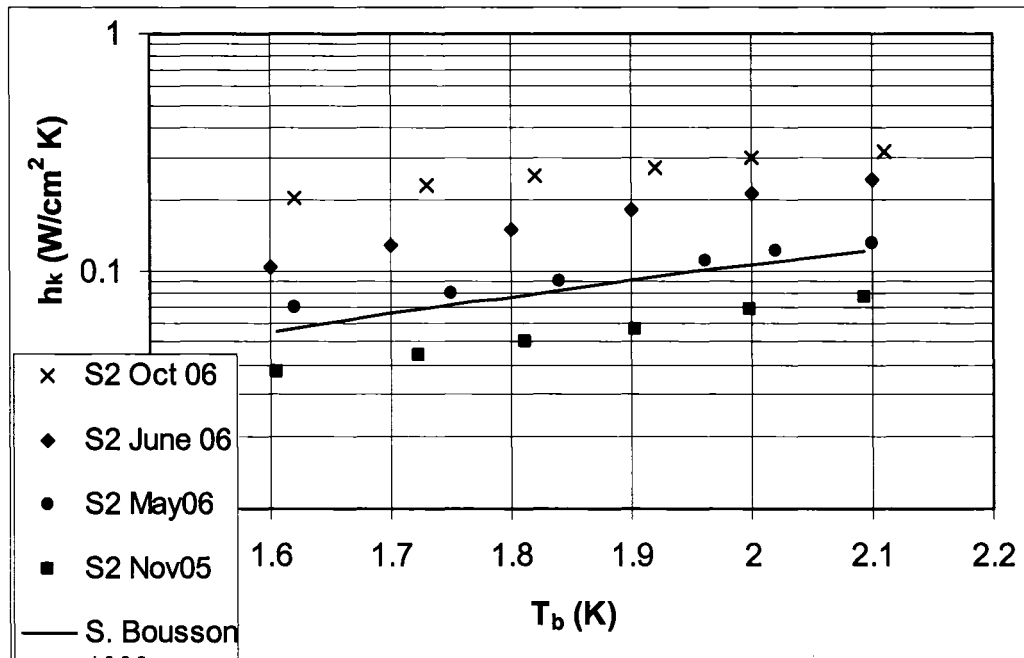
Figure 5.20: Kapitza conductance increase history for sample S2 through all the processes especially after titanification (Oct 06).

If the increase in Kapitza conductance is compared for the two samples together, as shown in figure 5.21, it is shown that after the titanification process both the samples (S1 Oct 06 and S2 Oct 06) attained comparably close values for the Kaptiza conductance. This is despite the fact that both the samples have surface roughness drastically different from each other. It is recalled from figure 5.1 that sample S1 has a smooth and plane surface where as sample S2 has a rough surface (on the order of ~1-2 mm) resulting in SI > 3. Although, the increase for the sample S2 (S2 Oct 06) is about 4 times from its initial state (Nov 05), this result suggests that surface effects due to titanification could be more stronger on increasing the kapitza conductance of the Nb samples than from the simple

area increase. The exact nature of these effects that resulted in the increase of Kapitza conductance after titanification is still undetermined. Surface strains relieved during moderate temperature annealing in titanification process could be one possible reason. Other factor that may result in this unexpected result could be from the distribution of crystal orientation (<111> or <110>) on the surface. The crystal size growth during the titanification process may result in substantially different distribution of crystal orientation closer to the surface as compared to their distribution before the titanification process. If the distribution of crystal orientations on the surface were more random than a uniform distribution of the same crystal orientation, the overall surface would be rough at the scale lengths of nanometer, the scale lengths, which are also comparable to the phonon wavelengths of He-II at these temperatures. This understanding may help explain the observation of comparably closer kapitza conductance values for the two samples after titanification despite their apparent differences in surface roughness at macro level. Nevertheless, this is the future work required for the subsequent studies in completely understanding the Kapitza conductance.
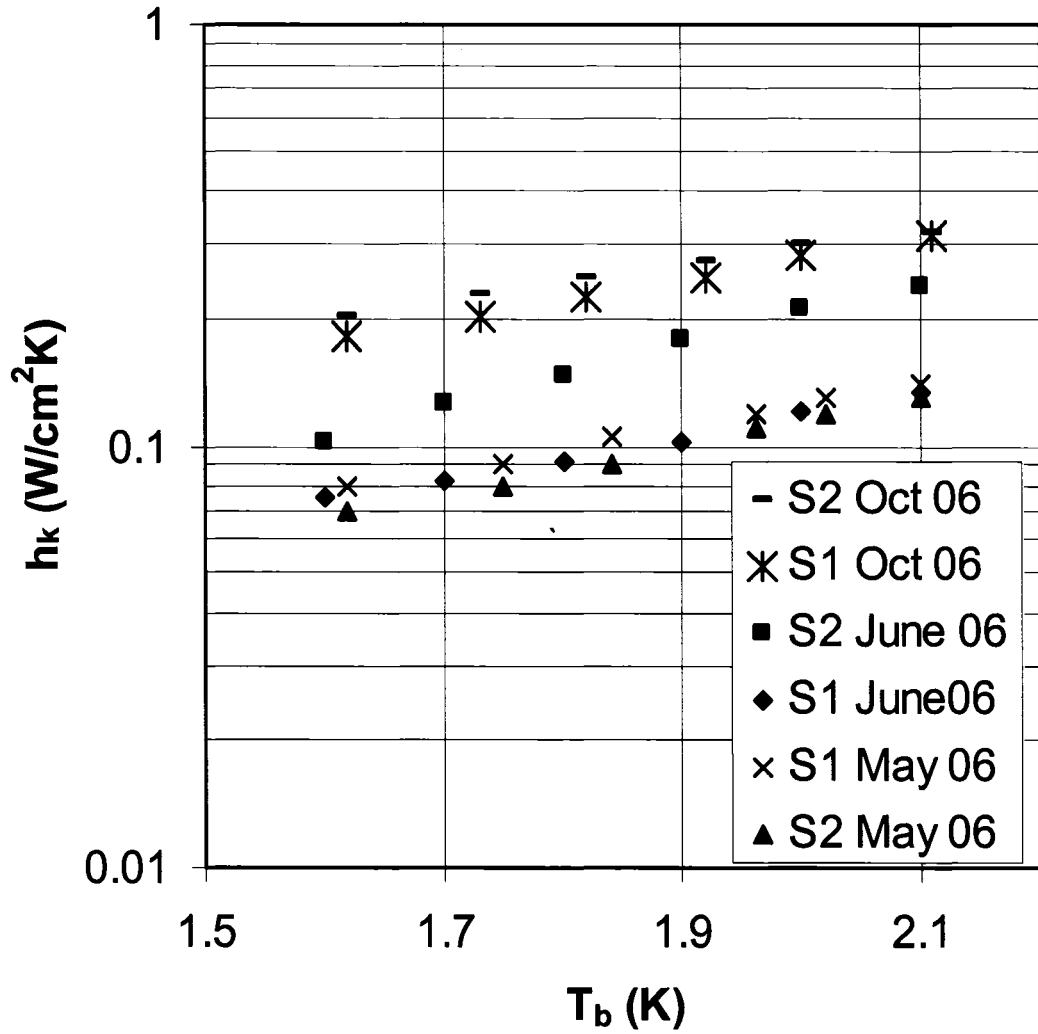
Figure 5.21: Comparison of Kapitza conductance values of the two samples, S1 and S2, after titanification (Oct 06).

6 Discussion

Several test for the thermal conductivity and Nb-He interface heat transfer measurements have been carried out. Thermal conductivity measurements are made on two different shapes of Nb samples i.e. Cylinder and flat plate. These measurements show not only close agreement with each other but also with the already published literature data to authenticate the results both for their repeatability as well as validity. Nb-He interface heat transfer measurements are done on two cylindrical samples S1 and S2. At temperatures 4.2 K, the nucleate boiling heat transfer characteristics are analyzed for various surface conditions. Similarly, at temperatures below 2.17 K, i.e. below T_λ when He is in super-fluid state, the Kapitza conductance measurements are made for various surface conditions.

6.1 Thermal Conductivity Above 3 K

As discussed in chapter 2, theoretical predictions require RRR value of Nb at 4.2 K to be directly proportional to its thermal conductivity at that temperature. This is given as:

$$RRR = 4 \, k$$

Table 6.1 has been compiled to verify the existence of such a correlation in the measurements carried out in this study as well as that of the data in the literature [9], [45]. The data from this table is then plotted in Figure 6.1 to show the variation of RRR values with thermal conductivity at 4.2 K. The least square fit to this data provides the slope of the data as ~ 4.08, which is reasonably close to the expected value of 4 within the experimental error.

Table 6.1: RRR values of Nb samples against the measured values of thermal conductivity at 4.2 K.

Nb Samples	Vender RRR	Measured K (W/m/K) at 4.2 K	Measured by
S1	232	62	A. Aizaz in this research
S2	232	60	
F1	390	98	
F2	390	95	
Pad1	400	95	Padamsee et. al. [9]
Pad2	250	62	
Pad3	90	22	
Bouch1	38	14	Boucheffa et. al. [45]
Bouch2	270	53	
Bouch3	194	45	
Bouch4	186	48	
Bouch5	100	30	
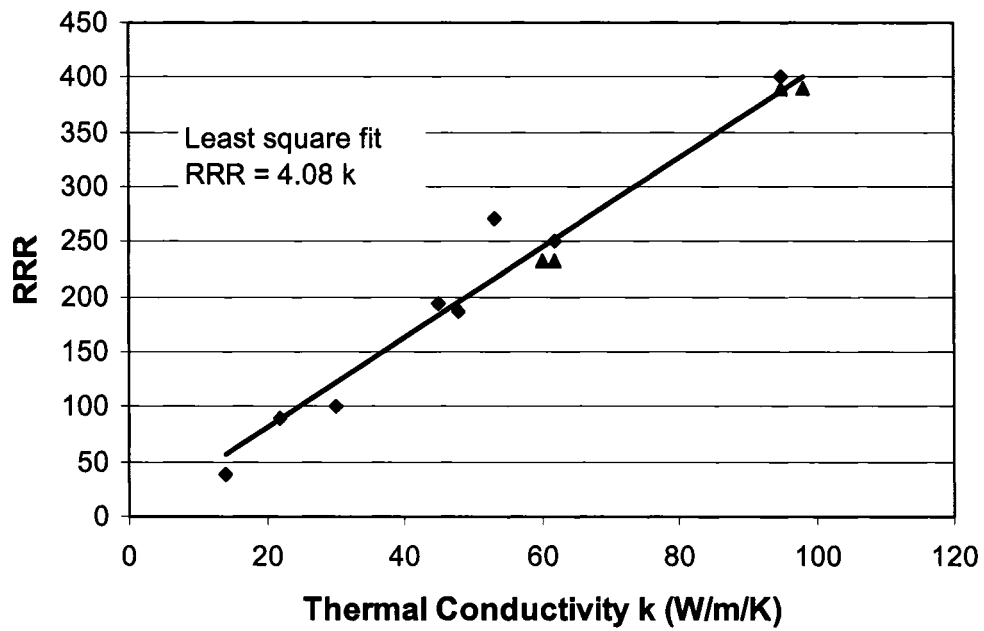
Figure 6.1: A linear correlation (least square fit) is shown for the variation of RRR values with those of thermal conductivity at 4.2 K. The (▲)data points in the plot are from current research.

6.2 Thermal Conductivity Below 3K

The thermal conductivity of Nb below its transition temperature is atypical of pure metals because of the superconductivity of Nb. At temperatures less than Tc, phonon conduction starts to play a significant role along with the electron conduction of thermal energy. This role of phonons keeps increasing, as we keep moving down away from the transition temperature, where increasing numbers of electrons are formed up into Cooper pairs. Thus, below ~3 K, the phonons become the dominant energy carriers and the microstructure of the bulk Nb becomes very important in determining the shape of thermal conductivity curve.

Although the thermal conductivity of Nb above 3 K is well correlated with its RRR value, as demonstrated above, the same is not true when the temperature is below 3 K. As discussed earlier, it is in this range of temperatures when the thermal conductivity of Nb is dominantly governed by phonon conduction. Thus the history of microstructure of the material becomes important. Higher purity (high RRR) Nb doesn't necessarily mean presence of phonon peak in the thermal conductivity at 2.0K. Even small amount of plastic deformations (~ 3% of strains) induced at any stage of material processing can cause the loss of phonon peak, as demonstrated in this research. This results in significant reduction (about 80 % at 2 K) of the thermal conductivity. This is especially important when the SRF cavities are routinely fabricated through the deep drawing process in which plastic deformations are deliberately induced to shape the cavity to the design requirements. Moderate temperature annealing, as demonstrated in this research, is a viable remedy to recover back the lost phonon peak in order to achieve higher gradients in the SRF cavities.

The major advantage of the improved phonon peak in the thermal conductivity is for high frequency defect free cavities operating at 2 K. To realize the significance of the phonon peak on the improved performance of SRF cavities, figure 1.3 is redrawn in this section for illustrative purposes. Recall that the simulations in this figure are with constant thermal parameters, i.e. constant thermal conductivity and the Kapitza conductance. To a first order approximation the simulations shown in figure 1.3 provides a good performance indicator for SRF cavities with lost phonon peak as compared with the recovered phonon peak. Also, since the total temperature variation on the RF surface is on the order of few hundreds of mK, the constant property approximation is not a bad choice.
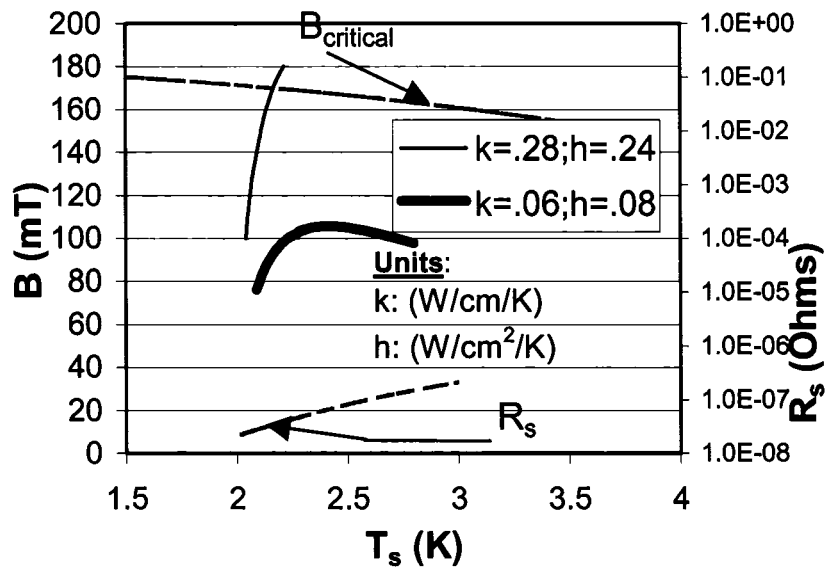
Figure 1.3: (Redrawn for illustration purposes) Thermal-magnetic simulations with constant thermal properties, k and h, for the two cases are shown. About five times increase in k and three times increase in h resulted in almost 50% improvement in applied magnetic fields.

Recall that figure 1.3 shows the two cases of selected thermal parameters, k and h_k, for which the applied magnetic field, B, is displayed against the calculated RF surface temperature T_s. The lower curve (thick line) is shown for a case of thermal conductivity without the phonon peak and the upper curve (thin line) is with phonon peak. Also note that the corresponding values of Kapitza conductance so chosen for the simulations have also been duly demonstrated in this study, which are close to the two cases of Kapitza conductance i.e. before and after moderate temperature annealing. The simulations shown in figure 1.3 reveals that applied magnetic field rose from 105 mT to 170 mT. Thus ~50% improvement in the applied magnetic field is realizable due to the presence of phonon peak and improved Kapitza conductance. Also both of these objectives, namely the phonon peak as well as improved kapitza conductance, can be attained through one single process of moderate temperature annealing of the Nb cavities.

For future research, moving forward in this direction, it is possible that much higher phonon peak is realizable than the one demonstrated in this research either through high temperature annealing (~1800 to 2000 °C), which may have a draw back of considerable reduction in the yield strength of Nb, or for longer durations of annealing at moderate temperatures. Also, since it's the strains in the microstructure of the Nb, which determines the presence of the phonon peak, it would be interesting to analyze the effect of unstrained single crystal / large grain Nb material on the size of phonon peak as compared with the polycrystalline Nb. Not to limit here, the effect of annealing of large grain / single crystal material may also be a fruitful option to explore.

6.3 Nucleate Boiling Heat Transfer

Operation of low frequency SRF cavities is carried out at 4.2K, the boiling temperature of He at atmospheric pressure. The present study has demonstrated, at least qualitatively, the effect of surface roughness on the nucleate boiling heat transfer. Almost 55 % reduction in superheat at heat flux of 10 mW/cm^2 has been shown due to the large SI > 3. This effect of large SI seems to be more pronounced only in the low heat flux regime when there are few bubbles on the surface and convection heat transfer effects still play important role in energy transfer from the surface. However, this result is still inconclusive due to the calibration range limitation in the experimental setup above 4.5 K. More experiments need to verify this observation over the extended calibration ranges to span the whole nucleate pool boiling regime of liquid helium.

In order to understand the effect of thermal parameters on the defect free low frequency cavities operating at 4.2 K, simulations similar to those discussed above for high frequency cavities, is presented in figure 7.2. Since the thermal conductivity at these temperatures is well correlated with the RRR of the Nb, this value is held constant for one particular value of RRR. However, for heat transfer coefficient two empirical correlations are used to see the effect of improved heat transfer coefficient through surface roughness. Schmidt's conservative correlation is used for low heat transfer coefficient (q = $\Delta T_s^{2.5}$), whereas Kutateladze's correlation (q = 5.8 $\Delta T_s^{2.5}$) provides almost six times more heat flux for the same amount of superheat [17], same as for a rough surface.

300 MHz Cavity at 4.2 K
RRR=230 Rres=5nOhms

q= 5.8$(T_s-T_b)^{2.5}$ Kutateladze   T$_s$ (K)   q=$(T_s-T_b)^{2.5}$ Schmidt
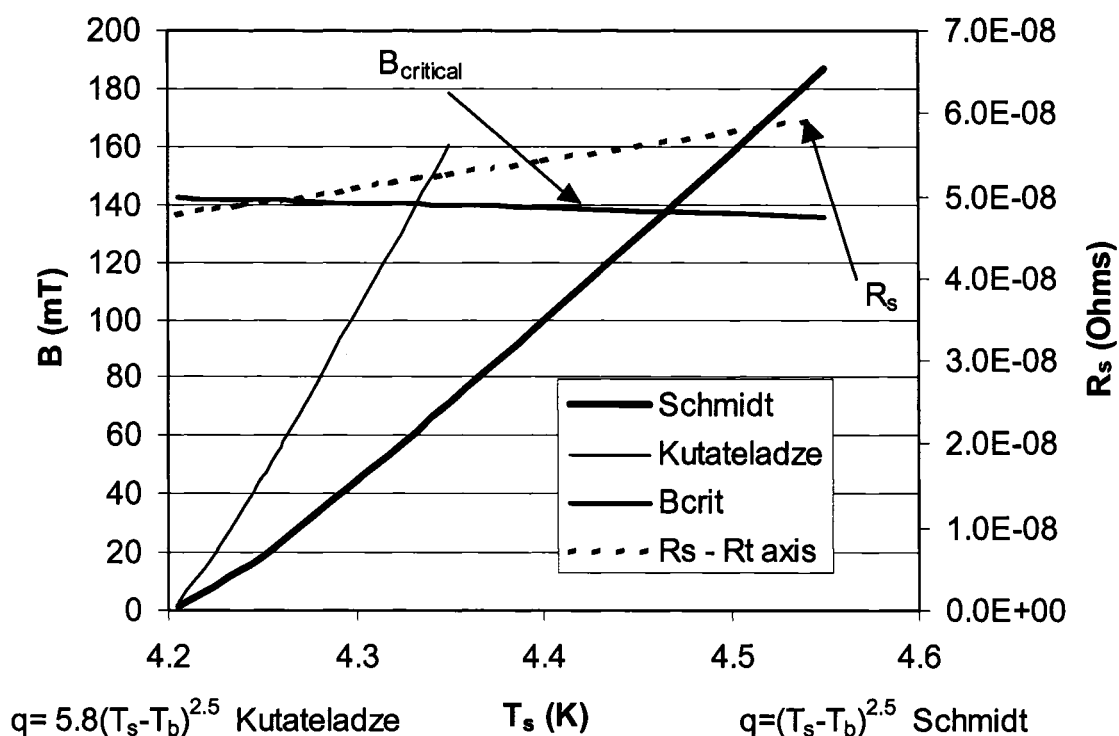
Figure 6.2: Thermal-Magnetic simulations for a defect free 300 MHz cavity at 4.2 K. Variation in surface resistance R_s is also plotted (Right axis) against the surface temperature T_s.

The simulations shown in figure 6.2 indicate that for a defect free 300 MHz cavity, even with a conservative heat transfer relation of Schmidt, which is for smoother surfaces, no fundamental limit on the thermal breakdown is found other than from the critical magnetic field at 138 mT. Although the RF surface temperature rise above ambient at this magnetic field is 0.28 K, the total change in R_s due to this temperature rise is ΔR_s ~8.3 nOhms. The improvement due to high heat transfer coefficient through surface roughness is shown through reduced T_s, which consequently results in lesser rise in R_s (ΔR_s ~4.1 nOhms) as compared with low heat transfer coefficient. Thus, this

112

improvement of high heat transfer coefficient through 100 % reduction in ΔR_s, may result in achieving proportionally higher Q_0 of the cavity at the break down fields. However this heat transfer coefficient has limited role in increasing the break down fields since the performance is shown limited by the critical magnetic fields.

In reality, low frequency cavities hardly reach closer to such a high magnetic field levels at 4.2 K. One possible explanation for the divergence of simulations from the real cavities comes from the caution that was placed in chapter 1 while using the relation for R_s in equation 1-2. Recall that the binding energy $\Delta(O)$ was assumed as constant with the condition that the $T_s < T_c/2$. However, operation of cavities at 4.2 K is so close to $T_c/2$ that the departure of the relation for R_s from the reality may be a significant effect. Also, since the physical size of the low frequency cavities is much larger than the high frequency cavities, there is more likelihood of having surface defects in the low fequency cavities causing thermal breakdown due to defects at much lower fields than the one predicted for the case of defect free cavity in the simulations. As discussed in chapter 1, for the case of cavities with defects, it's the thermal conductivity of the Nb that determines the quench field of the cavity and heat transfer coefficient has only a negligible effect.

6.4 Kapitza Conductance

The study has revealed a significant effect of annealing on the improvement of Kapitza conductance. At least 150 % increase in the Kapitza conductance has been demonstrated in this study at 2.1 K due to moderate temperature annealing. As discussed earlier, the effect of increased SI on Kapitza conductance doesn't seem to play a strong role as compared with the effect of annealing of the samples. Among other factors,

possibly removal of surface strains that might have been induced during the roughness process, has resulted in the increased Kapitza conductance after annealing. Also, since it is the nano-length scale roughness that is more important, crystal orientations on the surface could be one possible parameter that have changed due to annealing.

The effect of improved Kapitza conductance on the performance of SRF cavities have already been discussed in the above section while discussing the importance of phonon peak in the thermal conductivity of Nb. Also note that as the thermal conductivity of Nb is improved due to enhanced phonon peak, the importance of Kapitza conductance on the performance of SRF cavities becomes even more prominent. Even with such a substantial improvement of Kaptiza conductance after annealing has been demonstrated, yet the data found in this study for the Kapitza conductance is on the lower end of the wide spread of the data available in the literature for Nb. Hence room for further improvement in the Kapitza conductance still exists. Also, further study is required to point out the exact parameter that changed during the process of annealing and resulted in the improvement of Kapitza conductance.

7 Conclusions

7.1 Effect of Phonon Peak in Nb Thermal Conductivity

The performance of the defect free high frequency SRF cavities operating at temperatures below 2 K is greatly influenced by the thermal conductivity of Nb close to the operating temperatures. At these temperatures, phonons are the dominant energy carriers of energy and the microstructure of the bulk Nb becomes very important in determining the shape of thermal conductivity curve. This dissertation revealed that the strains induced through plastic deformations reduced the thermal conductivity of Nb by 80% at 2 K. This resulted in the loss of phonon peak. Low temperature annealing (at 750 °C for 2 hours) found to be insufficient to recover the lost phonon peak. However, titanification done at ~1300 °C restored the lost phonon peak near to its as received values.

The actual cavities are fabricated through a deep drawing process in which plastic deformations are induced to shape the cavity according to the design requirements. The absence of phonon peak in such cavities may cause their performance degradation. Simple numerical computations performed in this thesis reveal that the effect of recovery of the lost phonon peak along with improved Kaptiza conductance resulted in ~50 % improvement in the applied magnetic fields for the case of 1.3 GHz cavity operating at 2 K. Thus the need for titanification of cavities is found to be the single most necessary step in the preparation of high frequency cavities resulting in improved performance through enhanced phonon peak and significantly increased Kapitza conductance.

7.2 Effect of Surface Roughness on Nucleate Boiling Heat Transfer Coefficient

Surface roughness is found to increase the heat transfer by reducing the superheat of Nb surface in its pool boiling nucleate heat transfer regime. The effect of the large surface index is more pronounced in convection heat transfer regime of liquid helium than in its nucleate boiling regime. More experiments are needed to verify this observation over extended calibration ranges to span the whole nucleate pool-boiling regime of liquid helium.

The effect of the nucleate boiling heat transfer coefficient is found to decrease the ΔR_s of the cavity by 100 % thereby proportionally increasing the Q_o of the cavity at the break down magnetic fields. But it plays relatively small role in improving the break down magnetic fields since the fields are limited by the critical magnetic field. However, as discussed in the last section, the use of constant $\Delta(O)$ may be a poor approximation at 4.2 K in relation 1-2 for R_s. This may lead to a different analysis and thus needs more theoretical research.

7.3 Effect of Kapitza Conductance

The effect of the large surface index (increased surface area) on Kapitza conductance remained inconclusive possibly due to other effects influencing the heat transfer. These include, but are not limited to, the effect of surface strains, BCP etching, or the distribution of crystal orientation on the surface on the Kaptiza conductance. Although, both the low as well as the moderate temperature annealing has shown a consistent increase in Kapitza conductance, however, the exact cause of this increase is still undetermined. More research in this direction is needed to find the exact cause of increase in Kapitza conductance after annealing.

7.4 Looking Ahead: Large Phonon Peak and Large Kapitza Conductance

Back in 2001-2002, before the first step towards this research was taken, the role of the thermal parameters seemed to be exhaustively investigated and well known to the SRF community. Not much room for improvement in the performance of SRF cavity was talked about through improvement in thermal parameters, namely the thermal conductivity of Nb and its interface heat transfer coefficient with He. In this study, effort has been made to change this view by opening up new challenges for further work in this direction.

Enhancement of phonon peak in polycrystalline Nb could possibly be realizable either through high temperature (1800 to 1900 °C) annealing or for a longer duration at moderate temperatures. The use of unstrained single crystal / large grain Nb also seems to be a promising material to look for a considerably more enhanced phonon peak. Sometimes the lattice imperfections even in these single crystal / large grain material may not show the enhanced phonon peak. Moderate temperature annealing of such material may be necessary to bring the phonon peak to prominence.

Similarly, the domain of Kapitza conductance still pose many unanswered questions for which further research is needed. As discussed earlier, the effect of surface strains and / or crystal orientations on the surface need more attention to understand the effect of increased Kapitza conductance, as seen in this study through titanification process.

8 Appendices

8.1 Appendix A   Pool Boiling Heat Transfer

Boiling is a phase change process in which vapor bubbles are formed either on a heated surface or in a superheated liquid layer adjacent to the heated surface. It differs from evaporation at gas-liquid interfaces because it also involves creation of these interfaces at discrete sites on the heated surface. Nucleate boiling is a very efficient mode of heat transfer, and is used in various energy conversion and heat exchange systems. Pool boiling refers to boiling under natural convection conditions, whereas in flow boiling, liquid flow over the heater surface is imposed by external means.

Boiling is a complex process. Because the process is complex and there are so many heater and fluid variables that interact, complete theoretical models have not been developed to predict the boiling heat fluxes as a function of heater surface superheat. Figure A.1 shows, qualitatively, the boiling curve [44] (i.e. dependence of the wall heat flux, q, on the wall superheat on a surface submerged in a pool of saturated liquid). The wall superheat, ΔT, is defined as the difference between the wall temperature and the saturation temperature of the liquid at the system pressure. The plotted curve is for a flat plate or a horizontal wire to which the heat input rate is controlled. As the rate of heat input to the surface is increased, natural convection is the first mode of heat transfer to appear in a gravitational field.

At a certain value of the wall superheat (Point A), vapor bubbles appear on the heater surface. This is the onset of nucleate boiling. The bubbles form on cavities or scratches on the surface that contain preexisting gas/vapor nuclei. After inception, a dramatic increase in the slope of the boiling curve is observed. In partial nucleate boiling, corresponding to region II (curve AB) in Figure A.1, discrete bubbles are released from

119

randomly located active sites on the heater surface. The density of active sites and the frequency of bubble release increase with increasing wall superheat.

The transition from isolated bubbles to fully developed nucleate boiling (region III) occurs when bubbles at a given site begin to merge in the vertical direction. Vapor appears to leave the heater in the form of jets. The condition of jet formation also approximately coincides with the merger of vapor bubbles at the neighboring sites. A small change in the slope of the boiling curve can occur upon transition from partial to fully developed nucleate boiling. The heat flux on polished surfaces varies with wall superheat roughly as

$$q \sim \Delta T^m \tag{A-1}$$

where m has a value between 2 and 3 [17].
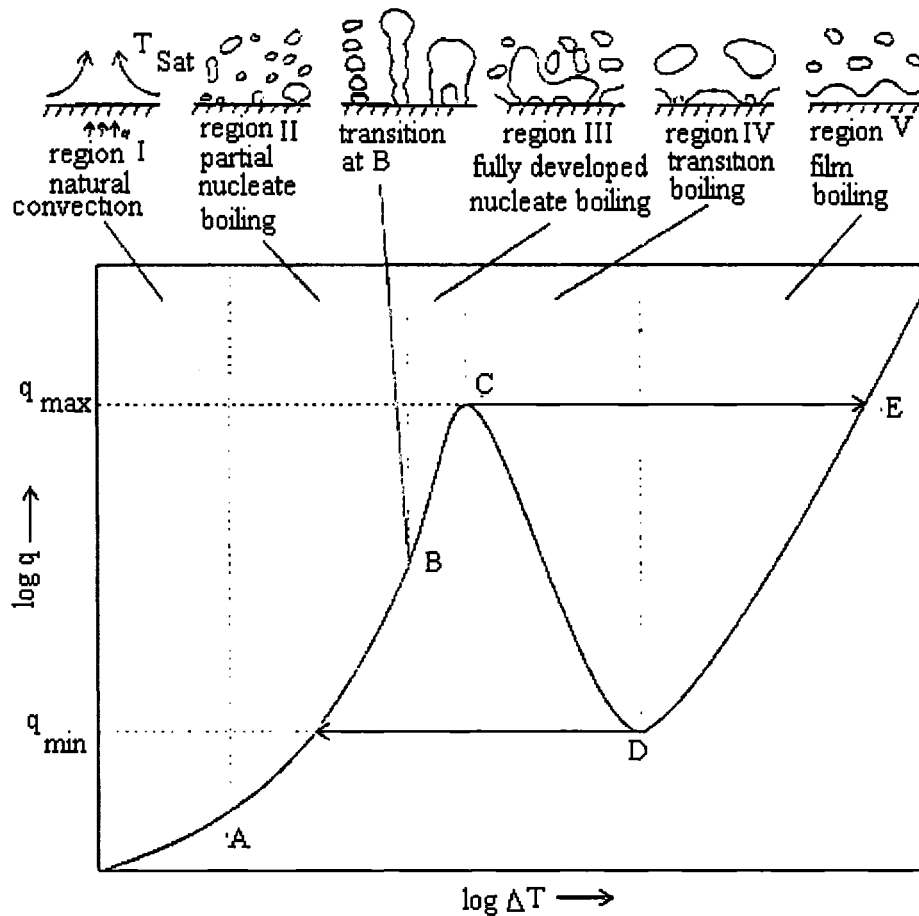
Figure A.1: Typical boiling curve, showing qualitatively the dependence of the wall heat flux, q, on the wall superheat, ΔT, defined as the difference between the wall temperature, T_w, and the saturation temperature, T_{sat}, of the liquid. Schematic drawings show the boiling processes in regions I–V. These regions and the transition points A–E are discussed in the text. (Adapted from Burmeister [44]).

The maximum or critical heat flux, q_{max} sets the upper limit of fully developed nucleate boiling for safe operation of equipment. After the maximum heat flux is reached, most of the surface is rapidly covered with vapor. The surface is nearly insulated, and the surface temperature rises very rapidly. When the rate of heat input is controlled, the heater surface passes quickly through regions IV and V (see Figure A.1) and stabilizes at point E. If the temperature at E exceeds the melting temperature of the heater material,

the heater will fail (burn out). The curve ED (region V) represents stable film boiling, and the system can be made to follow this curve by reducing the heat flux from q_{max}.

In stable film boiling, the surface is covered with vapor film, and liquid does not contact the solid. On a horizontal surface the vapor release pattern is governed by Taylor instability of the vapor-liquid interface. With a reduction of heat flux in film boiling, a condition is reached when a stable vapor film on the heater can no longer be sustained. Heat flux and wall superheat corresponding to the condition at which vapor film collapse occurs are referred to as the minimum heat flux q_{min}, and the minimum wall superheat ΔT_{min}, respectively. Upon collapse of the vapor film, the surface goes through regions IV, III, and II very rapidly and settles in nucleate boiling. Region IV, falling between nucleate and film boiling, is called transition boiling, which is a mixed mode of boiling that has features of both nucleate and film boiling. Transition boiling is unstable, since it is accompanied by a reduction in the heat flux with an increase in the wall superheat. As a result, it is difficult to obtain steady state data in transition boiling, except when the heater surface temperature is controlled.

8.2 Appendix B   Estimation of Measurement Errors

All measurements involve two types of errors or uncertainties. These are

- Uncertainties arising from a random effects

- Uncertainties arising from a systematic effects

Since the systematic effects have been dealt separately in appendix C and D, in this section quantitative estimates of the uncertainty due to random effects are analyzed.

8.2.1 Thermal Conductivity Measurement Uncertainty

Thermal conductivity is approximated from the measurement of the temperature difference between the two sensors when a known input electrical power is applied to the heater. Mathematically,

$$k = (Q/A)*(l/\Delta T) \qquad\qquad\qquad \text{B-1}$$

where, Q is the known electrical power input to the heater, l is the distance between the two sensors, A is the cross-sectional area through which heat is conducted in the material from the heater to the sensors and, ΔT is the difference of temperatures measured by the two sensors. Thus, the uncertainty in thermal conductivity, k, can be expressed as

$$\frac{\varepsilon_k}{k} = \sqrt{\left(\frac{\varepsilon_Q}{Q}\right)^2 + \left(\frac{\varepsilon_l}{l}\right)^2 + \left(\frac{\varepsilon_A}{A}\right)^2 + \left(\frac{\varepsilon_{\Delta T}}{\Delta T}\right)^2} \qquad \text{B-2}$$

Each uncertainty in equation B-1 arising from the individual parameters can be estimated separately.

The uncertainty in the electric power to the heater, Q, can be estimated from the measurements of both the applied voltage v and the corresponding current I as given in equation B-3.

$$\frac{\varepsilon_Q}{Q} = \sqrt{\left(\frac{\varepsilon_v}{v}\right)^2 + \left(\frac{\varepsilon_I}{I}\right)^2}$$
$$\text{B-3}$$

where ε_v and ε_I are provided by the manufacturer of the power supply unit.

Similarly, the uncertainties associated with measuring the length between the sensors and the cross sectional area through which heat is conducted, are related with the measuring device, usually through a digital read out of a vernier caliper.

The uncertainty associated with the ΔT is given as

$$\varepsilon_{\Delta T} = \sqrt{\left(\varepsilon_{T1}\right)^2 + \left(\varepsilon_{T2}\right)^2}$$
$$\text{B-4}$$

where ε_{T1} and ε_{T2} are the uncertainties related with the measurement of the temperature of any given pair of sensors, say sensor 1 and 2 respectively, through which the thermal conductivity is measured. The primary source of uncertainty in the temperature measurements of the carbon sensors is from interpolation polynomial used for the calibration fit. Detailed accounts of this uncertainty and other contributory factors have been documented earlier [39].

8.2.2   Interface Heat Transfer Measurement Uncertainty

The measurement of the heat flux across Nb-He interface is done using the following equation:

$$q = Q / A = h (T_s - T_b) \qquad \text{B-5}$$

where q is the heat flux through the interface, T_s is the Nb surface temperature, and T_b is the bath temperature of liquid helium. As discussed in chapter 3, usually the heat transfer in nucleate boiling regime of He-I is shown on a plot of heat flux applied against the surface temperature rise above the ambient. Errors associated with this temperature rise

124

are only related with the uncertainty of finding the temperature rise of exposed Nb surface above ambient i.e. ΔT_s. The interface surface temperature (T_s) of Nb is estimated from the linear extrapolation of temperature T_3 as measured by carbon sensor C3 and temperature T_2 as measured by carbon sensor C2. Refer figure 4.10 for the location of the two sensors where C3 is shown closer to the interface. The linear extrapolation assumes constant thermal conductivity between the sensors and its final form is given as.

$$T_s = (1+Lr)T_3 - (Lr)T_2 \qquad \text{B-6}$$

where Lr is the ratio of distance l_{3s} to that of distance l_{23}. In this nomenclature l_{3s} is the distance between the carbon sensor C3 and the interface, and l_{23} is the distance between carbon sensor C2 and C3.

Thus,

$$\Delta T_s = T_s - T_b = (1 + Lr)\, T_3 - (Lr)\, T_2 - T_b \qquad \text{B-7}$$

Now the uncertainty in ΔT_s is given as

$$\varepsilon_{\Delta T_s} = \sqrt{(1 + Lr)^2 (\varepsilon_{T3})^2 + (T_3 - T_2)^2 (\varepsilon_{Lr})^2 + (Lr)^2 (\varepsilon_{T2})^2 + (\varepsilon_{Tb})^2} \qquad \text{B-8}$$

where ε_{T2}, ε_{T3}, and ε_{Tb} are the uncertainties associated with the measurements of temperatures T_2, T_3, and T_b respectively and are discussed in section 7.2 above. Also, ε_{Lr} is the uncertainty associated with the measurement of Lr and is given as

$$\frac{\varepsilon_{Lr}}{Lr} = \sqrt{\left(\frac{\varepsilon_{l3s}}{l_{3s}}\right)^2 + \left(\frac{\varepsilon_{l23}}{l_{23}}\right)^2} \qquad \text{B-9}$$

where ε_{l3s}, and ε_{l23} are the uncertainties associated with measuring the distance l_{3s} and l_{23} respectively and are discussed in section 7.2 above.

8.3 Appendix C   Parallel Heat Flow Losses

Instead of all of the heat going through the Nb sample from the heater, some of it may leak into the base plate through the G-10 block. This is known as parallel heat flow and is shown in figure C.1 along with its thermal circuit diagram. This parallel heat loss can be estimated with the help of known thermal resistances of various components in each of the thermal path. In steady state, we know

$$Q_{in} = (T_h - T_b) / R_{tot} = \Delta T / R_{tot} \tag{C-1}$$

where T_h is the temperature of the heater.

The percentage of heat lost in the parallel path, Q_L, is then given by the ratio of the resistances in the actual path to that of the resistances in the parallel path. Mathematically, it is given by the equation

$$Q_L = Q_p / Q_{Nb+Cu} * 100 = (R_{Nb+Cu} / R_P) * 100$$

where, R_p is resistance of the parallel path and is given as

$$R_p = R_{G-10} + R_{BP} + R_{6\,Rods} + R_{Flange}$$

Table C1 shows that the heat loss from parallel path is less than 0.1% of the total heat supplied by the heater.
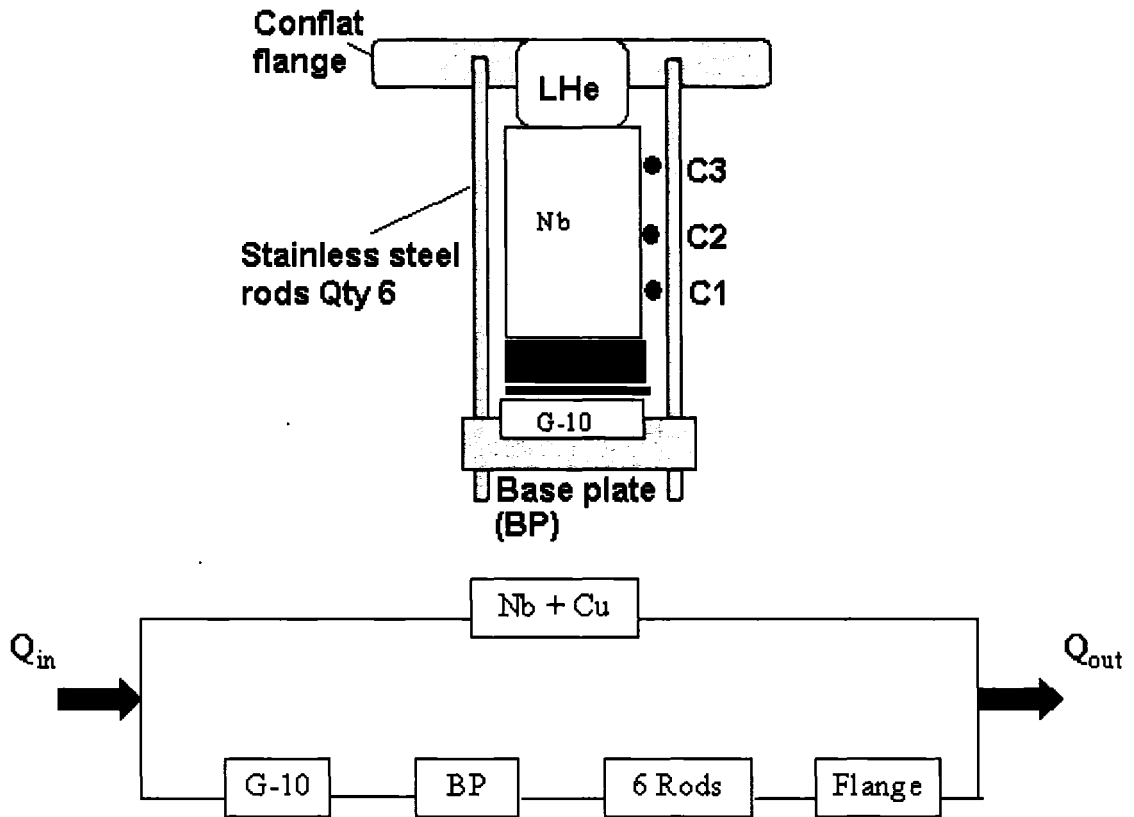
Figure C.1: Thermal circuit showing parallel heat leak.

Table C1: Percentage of heat loss calculation based on thermal circuit given in figure C.1

Title	Nb	Cu	G-10	BP	Rods	Flange
Resistance (K/W)	0.71	0.060	31.43	32.12	1410.3	23.92
Sub total (K/W)	0.77		1497.77			
Heat Loss (%)	0.05					

8.4 Appendix D Estimation of Heat Leak into Stainless Steel Tube

Estimation of heat leak from the Nb sample into the stainless steel tube containing liquid He at 2.0 K can be made through an assumption of infinite length, as shown in figure D.1. Given the excellent cooling properties of super-fluid He, most of the heat coming into the tube from the Nb sample would go be removed through convection into the liquid helium. Therefore the assumption of infinite length fin is reasonable.

Figure D.1: Estimation of heat leak into the stainless steel tube

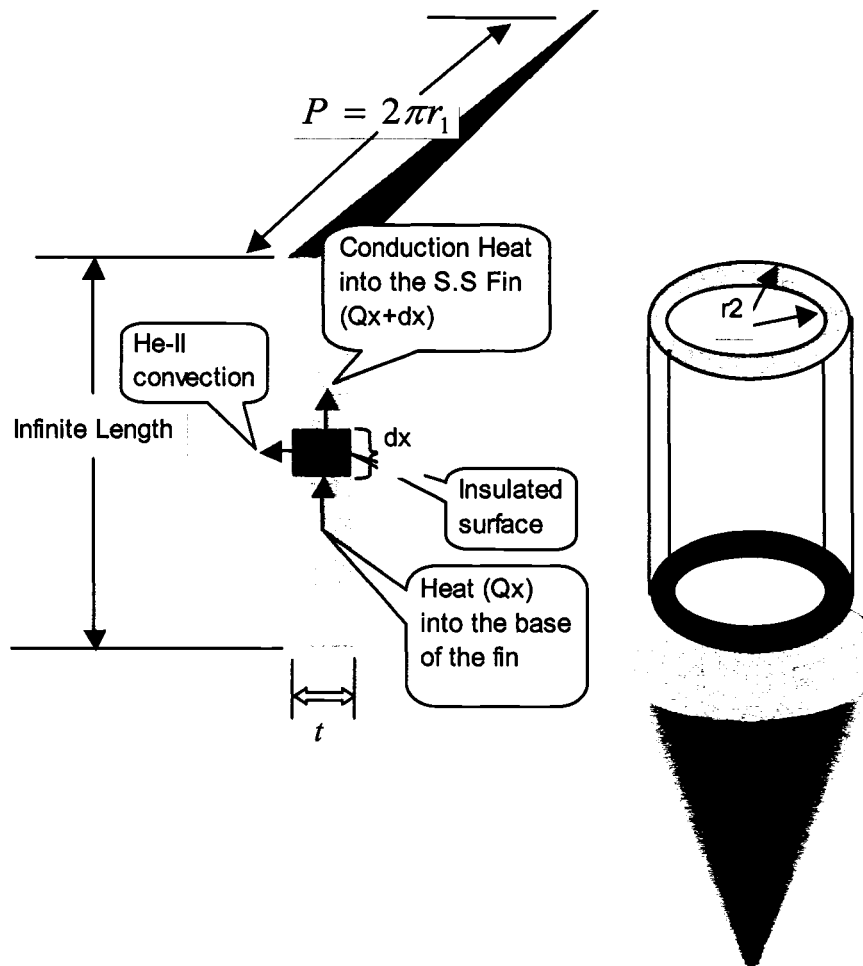Using the basic elemental approach to formulate the heat transfer equation by neglecting radiation losses, as shown in figure D.1, gives

$$Q_x - Q_{x+dx} - Q_{conv} = 0$$

$$Q_x - (Q_x + \frac{dQ}{dx} \Delta x) - h_{ss}(2\pi r_1)(T - T_\infty) = 0$$

Canceling out the terms results into the desired differential equation

$$\frac{d^2\Theta}{dx^2} - \frac{h_{ss}}{kt}(\Theta) = 0$$

where, $\Theta = (T_s - T_b)$ with boundary conditions as (a) $\Theta = 0$ $at\, x = \infty$; and (b) $\Theta = \Theta_s$ $at\, x = 0$. Here T_s is the base surface temperature of the fin and is approximately equal to the temperature of the Nb-He surface interface and T_b is the bath temperature. Solving the above differential equation by applying appropriate boundary conditions, we get

$$Q_{fin} = \sqrt{h_{ss}k_{ss}t}\, P(T_s - T_b)$$

where, h_{ss}, k_{ss} t and P are Kaptiza conductance, thermal conductivity thickness and the perimeter of stainless steel tube, respectively.

Thus, using the average values of thermal conductivity of stainless steel and its Kapitza conductance [37] at 2.0 K, the percentage of heat lost is estimated as :

$K_{ss} = 0.2$ W/m/K, $h_{ss} = 2*10^3$ W/m^2/K, thickness t = r_2-r_1 = 0.001 m

$$\frac{Q_{fin}}{Q_{total}} = 0.112\%$$

8.5 Appendix E   Sensors Sensitivity Comparison

Table E1 shows a comparison between a typical carbon sensor with that of standard germanium sensor [39].

Table E1: Comparison of sensitivity of carbon sensor with germanium sensor [39]

Sensor Type		Germanium	Carbon
Temperature Coefficient		Negative	Negative
Monitor Display Resolution		100 mΩ	100 mΩ
Sensor Sensitivity at	4 k	-117 Ω / K	-572 Ω / K
	2 K	-930 Ω / K	-10538 Ω / K
Monitor Display Resolution w.r.t. 100 mΩ	4 K	854.0 μK	174.0 μK
	2 K	107.5 μK	9.4 μK

However, due to high sensor resistance, self-heating could be a possible problem, especially at temperatures below 1.9 K. Usually a high valued resistor is placed at room temperature in parallel with the carbon sensor to overcome this problem, but it comes with a price of a small reduction ($\sim$ <10 % at 4.2 K) in the sensor sensitivity. This decrease in sensitivity is insignificant to pose any concern for the steady state measurements in the described experiment apparatus.

8.6 Appendix F   Specification Sheet for Nb Samples

MATERIAL TEST RESULTS 試驗成績表

No. 11641
TOKYO DENKAI CO., LTI
東京電解株式会社
Date 日付 Jan 18, 2002

Customer 御納入先	Messrs. NATIONAL SUPERCONDUCTING CYCLOTRON LABORATORY
Surveyor 御立会者	

Material 材質	Nb
Article 品名	RRR NIOBIUM ROD
Specification No. 仕様書番号	NSCL RFQ SB2541

Lot No.	Size 寸法 mm	Quantity 数量 pcs or gr
	Φ30 Diameter x 150 Long	2pcs

Mechanical properties 機械的特性

	T.S 引張強さ Kg/mm²	Y.S 耐力 Kg/mm²	Elong 伸び %	Hardness かたさ Hv	E.V. エリクソ-
Spec 規格 min / max					
Test Results 試験結果					
Longitudinal					
Transverse					

Chemical Composition (in Wt%) 化学成分

Element 成分	Ta	W	Ti	Fe	Si	Y.S	Mo	Ni	Zr	H
Spec 規格 min / max										
Test Results 試験結果	0.059	0.002	<0.001	<0.001	<0.001	<0.001	<0.001	<0.001	<0.001	<0.0

Chemical Composition (in Wt%) 化学成分

Element 成分	O	N	H	C
Spec 規格 min / max				
Test Results 試験結果	<0.001	<0.001	<0.0002	<0.001

Remarks 備考 Starting Ingot No. NB-524   RRR Value of Ingot 232

T.S.=Tensile Strength   Y.S.=Yield Strength   E.V.=Erichsen Value

Inspection Section
Manager 課長
Engineer 担任

Figure F.1: Specification sheet for cylindrical samples S1 and S2

131

8.7 Appendix G Surface Roughness Parameters

8.7.1 Introduction

For the discussions that follow, Z(x,y) is the function representing the height of the surface relative to the best fitting plane, cylinder, or sphere. Note that a used in the following integral expressions implies that the integration is performed over the area of measurement and then normalized by the cross-sectional area "A" of the measurement [48].

$$\iint_a Z(x,y)dxdy \equiv \frac{1}{A} \int_0^{Lx} \int_0^{Ly} Z(x,y)dxdy$$

8.7.2 Ra, The Roughness Average

It is the arithmetic average of the absolute values of the surface height deviations measured from the best fitting plane, cylinder or sphere. Ra is described by:

$$R_a = \iint_a |Z(x,y)|dxdy$$

Historically, Ra was one of the first parameters used to quantify surface texture. Most surface texture specifications include Ra either as a primary measurement or as a reference. Unfortunately, Ra may be misleading in that many surfaces with grossly different features (e.g., milled vs honed) may have the same Ra, but function quite differently [48].

132

Profile

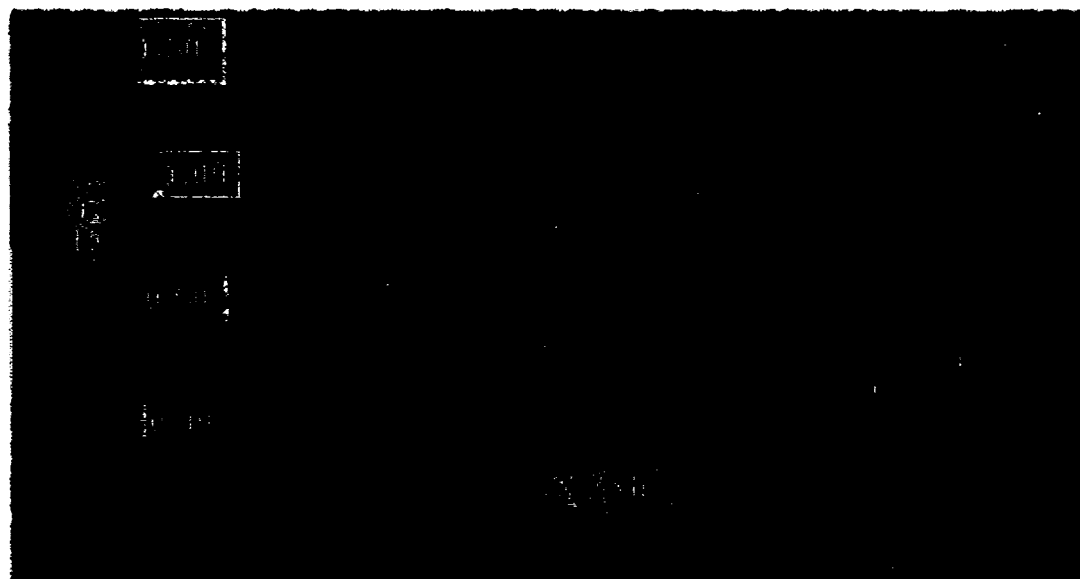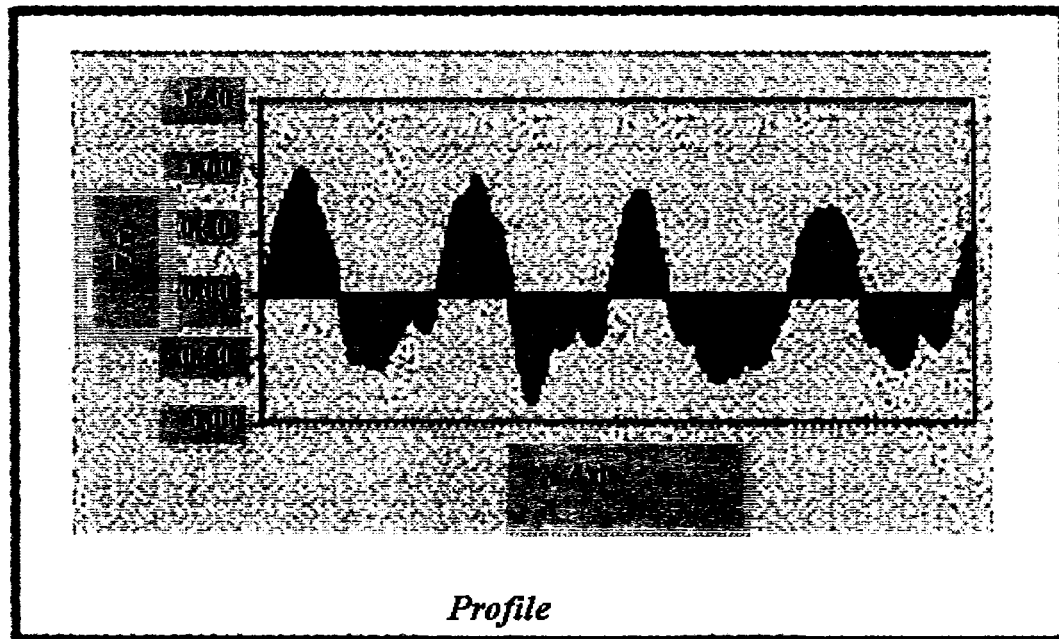*Absolute Value of Profile*

Figure G.1: Profiles are shown above for simplicity for the understanding of basic definition of Ra. When evaluating the 3D parameters the various surface functions are understood to apply to the complete 3D dataset. Adapted from Cohen [48]

133

Ra only quantifies the "absolute" magnitude of the surface heights and is insensitive to the spatial distribution of the surface heights. Ra is also insensitive to the "polarity" of the surface texture in that a deep valley or a high peak will result in the same Ra value. Despite its shortcomings, once a process for forming a surface has been established, Ra may be used as a good monitor as to whether something may have changed during subsequent production of the surface [48].

8.7.3   Rq, The Root Mean Square (rms) Roughness

It is the rms (standard deviation) or "first moment" of the height distribution, as described by:

$$Rq = \sqrt{\iint_a (Z(x,y))^2 \, dxdy}$$

Rq, or the rms of the surface distribution, is very similar to Ra and will usually correlate with Ra. Since the surface heights are "squared" prior to being integrated / averaged, peaks and valleys of equal height / depth are indistinguishable. As for Ra, a series of high peaks or a series of deep valleys of equal magnitude will produce the same Rq value. The Rq value is also insensitive to the spatial distribution of the surface heights, in that two very high peaks will contribute the same to Rq whether the peaks are close to each other or separated over the measurement field. The Rq parameter is typically used in the optics industry for specifying surface finish, since various optical theories relating the light scattering characteristics of a surface to Rq have been developed [48].
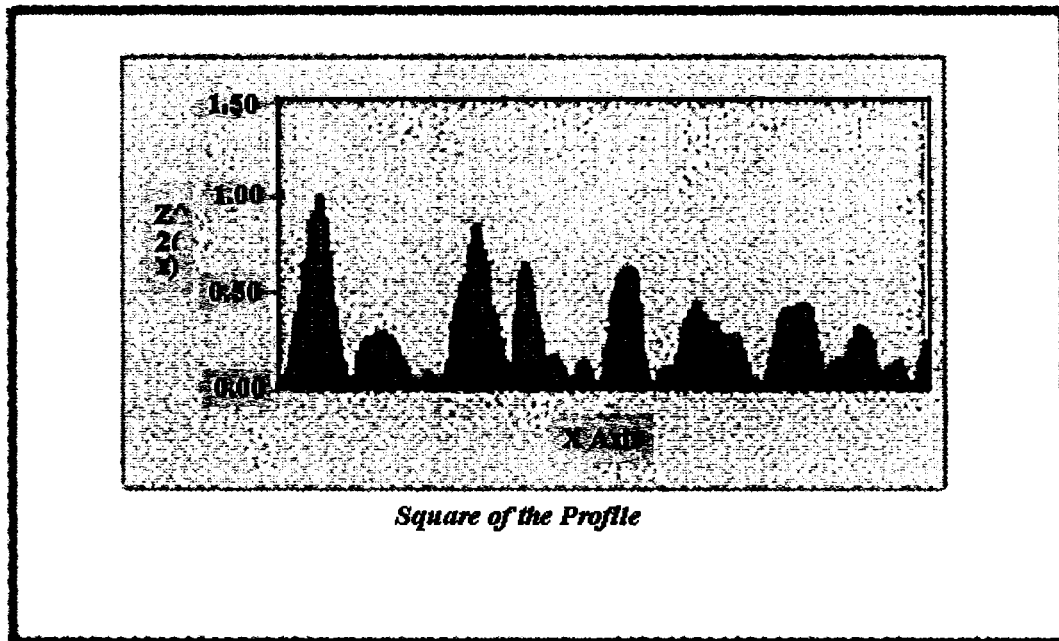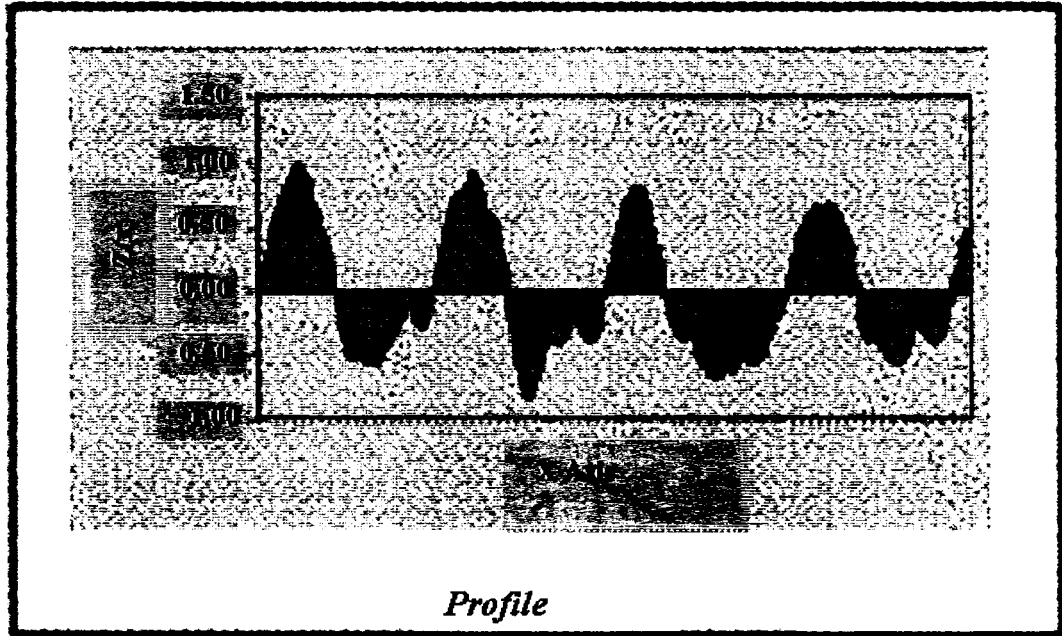
Profile

Square of the Profile

Figure G.2: Profiles for Rq are shown above for simplicity. When evaluating the 3D parameters the various surface functions are understood to apply to the complete 3D dataset. Adapted from Cohen [48]

8.7.4 Rp, Rv, Rt, Rpm, Rvm, Rz

Rp, Rv, and Rt are parameters evaluated from the absolute highest and lowest points found on the surface. Rp, the maximum peak height, is the height of the highest point. Rv, the maximum valley depth, is the depth of the lowest point. Rt, the maximum height of the surface, is found from Rp – Rv.

The Rpm, Rvm, and Rz parameters are evaluated from an average of the heights and depths of a number of extreme peaks and valleys. Rpm the average maximum peak height is found by averaging the heights of the ten (10) highest peaks found over the complete 3D image. Rvm, the average maximum valley depth is found by averaging the depths of the ten (10) lowest valleys found over the complete 3D image. Rz, the average maximum height of the surface is then found from Rpm-Rvm. Note that in determining the peaks and valleys, the analysis software eliminates a grid of 11 x 11 pixels around a given peak / valley before searching for the next peak / valley, thus assuring that localized, separated peaks / valleys are found [48].
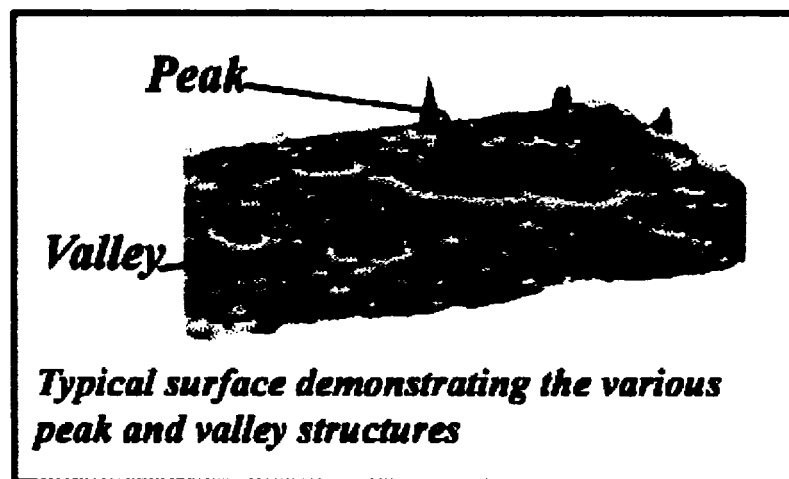

Figure G.3: Peak and valley structure of a typical surface is shown. Adapted from Cohen [48]

8.7.5 Application

Since Rp, Rv, and Rt are found from single points, they tend to be unrepeatable measurements. Thus when using these three parameters, one must be sure to make multiple measurements, consistent with the observed variations to obtain a statistically significant result. If the surface measurements are filtered prior to analysis (e.g. with a low pass filter), the results may be more repeatable. Rpm, Rvm and Rz may be used to characterize the extreme features of a surface, with Rz being a nominal measure of the "Peak-to-Valley" range of the surface. Typical applications for Rz may include sealing surfaces and coating applications. Rpm may find application when considering surfaces that will be used in a sliding contact application. Rvm may find application when valley depths relating to fluid retention may be of concern such as for lubrication and coating systems [48].

9 References

1. J.P. Turneaure; Ph.D. Thesis, Stanford University (1967).

2. J. Halbritter; Z. Phys., **238**, 466 (1970).

3. J. Halbritter; Proceedings of the 2nd Workshop on RF Superconductivity, CERN, Geneva, Switzerland; 427 (1984).

4. F. Palmer; Proceedings of the 3rd Workshop on RF Superconductivity, Argonne National Laboratory, Argonne, IL, USA; 309 (1988).

5. J.P. Turneasure, in Proceedings of the 1972 Applied Superconducting Conference, Annapolis, IEEE, p. 621 (1972). IEEE Pub. No. 72CH0682-5-TABSC.

6. D. Moffat; Proceedings of the 4th Workshop on RF Superconductivity, KEK, Tsukuba, Japan, KEK-Report 89-21 (1989); also CLNS 89-934 (1989).

7. J.R. Delayen, et al.; Proceedings of the 5th Workshop on RF Superconductivity, DESY, Hamburg, Germany, DESY M-92-01 (1992).

8. H. Piel; Proceedings of the CERN accelerator school 1988, S.Turner ed., DESY, Hamburg, West Germany, CERN 89-04, 149 (1988).

9. H. Padamsee, J. Knobloch, T. Hays; *RF Superconductivity for Accelerators*; John Wiley & Sons, INC. (1998).

10. J.H. Graber; Ph.D.Thesis, Cornell University, May (1993).

11. J. Amrit, C.Z. Antoine, M.X. Francois, and H. Safa; Adv. in Cryo. Eng.: Proc. of the Cryo. Eng. Conf., Vol 47. (2002).

12. H. Padamsee; IEEE Trans. Mag., Mag-21, 1007 (1985).

13. J. Knobloch, R.L. Geng, M. Liepe, and H. Padamsee; 9th Workshop on RF Superconductivity, Santa Fe USA, Vol. I, p77, SRF (1999)

14. K. D. Timmerhaus, and T. M. Flynn; *Cryogenic Process Engineering*, Plenum press New York (1989), Pg. 67 to Pg. 73.

15. J.G. Weisend II, Lecture notes provided during short course at Cryogenic Engineering Conf. Anchorage AK Sept. (2003).

16. V. K. Dhir, Annu; Rev. Fluid Mech., 30:365–401, (1998).

17. S.W. Van Sciver; *Helium Cryogenics*, Plenum Press (1986).

18. E.T. Swartz, R.O. Phol; Reviews of Modern Physics, Vol.61; No 3, July (1989).

19. I.M. Khalatnikov; *An Introduction To The Theory of Super fluidity*, Chapter 23; W.A. Benjamin, INC.; (1965).

20. L.J. Challis; Phys. Lett. A 26, 105, (1968).

21. L.J. Challis; J. Phys. C 7,481, (1983).

22. J.P. Harrison; J. Low Temp. Phys. 17, 43, (1974).

23. J. Halbritter; Phys. Lett. A 49,379, (1974).

24. J. Halbritter; Physica B 108, 917, (1981).

25. K.R. Farmer, C.T. Rogers, and R.A. Buhrman; Phys. Rev. Lett. 58, 2255, (1987).

26. I.M. Gel'fgat and E.S. Syrkin; Fiz. Nizk. Temp. 4, 141, 1978; [Sov. J. Low Temp. Phys. 4, 69 (1978)].

27. J.C.A. Van der Sluijs and A.E. Alnaimi; *Phonon Scattering in Solids*, edited by L.J. Challis, V.W. Rampton, and A.F.G. Wyatt; (Plenum, New York), p.34, (1976).

28. J.C.A. Van der Sluijs; Cryogenics 16, 161, (1976).

29. J. Weber, W. Sandmanm, W. Dietsche, and H. Kinder; Phys Rev. Lett. 40, 1469, (1978).

30. J. Amrit and, M.X. Francois; J. Low Temp. Phys., 119, p 27, (2000).

31. J.Amrit, C.Z. Antonine, M.X. Francois and, H. Safa; Adv. Cryo. Eng.: Proc. Of the Cryo. Eng. Conf., 47, p 499, (2002).

32. T. Klitsner; Ph.D. Thesis Cornell University, (1987).

33. T. Klitsner and R.O. Pohl; Phys. Rev. B, 34, 6045, (1986).

34. T. Klitsner; Phys. Rev. B; 36, 6551, (1987).

35. K. Mittag; Cryogenics, p 94, February (1973).

36. N.S. Snyder; Cryogenics, 10, 89, (1970).

37. A. Kashani and S.W. Van Sciver; Cryogenics, p 238, Vol. 25, May (1985).

38. S. Bousson, M. Fouaidy, T. Junquera, N. Hammoudi, J.C. Le Scornet, and J. Lesrel; 9th workshop on RF Superconductivity, Santa Fe, (1999).

39. A. Aizaz, M.Sc. Thesis, Michigan State University, (2002).

40. A. Aizaz and T.L. Grimm, Advances in Cryogenic Engineering: Transactions of the Cryogenic Engineering Conference-CEC05, Vol. 51B, (2006).

41. B. Gebhart., Y. Jaluria, R. Mahajan, and B. Sammakia; *Buoyancy Inducd Flows and Transport*, Hemisphere Press, (1988).

42. E. Hahne, U. Grigull; *Heat Transfer in Boiling*, Hemisphere Press, (1977).

43. P. Kapitza; The Study of Heat Transfer on He II, J. Phys. (USSR) 4, 181 (1941).

44. L. Burmeister; *Convective Heat Transfer*, John Wiley & Sons, INC. (1993).

45. A. Boucheffa, M. X. Francois, and F. Koechlin; Proceedings of the 15th International Cryogenic Engineering Conference, (1994).

46. H. Padamsee; IEEE Transactions on Magnetics, Vol. MAG-23, No 2, pg 1607, March (1987).

47. R. L. Geng; E-mail communication, October (2006).

48. D.K. Cohen; http://www.michmet.com, Email communication, October (2006)